

UNCLASSIFIED

AD NUMBER	
AD357980	
CLASSIFICATION CHANGES	
TO:	UNCLASSIFIED
FROM:	CONFIDENTIAL
LIMITATION CHANGES	
TO: Approved for public release; distribution is unlimited.	
FROM: Distribution authorized to U.S. Gov't. agencies only; Administrative/Operational Use; 31 JAN 1958. Other requests shall be referred to Defense Atomic Support Agency, Washington, DC. Formerly Restricted Data.	
AUTHORITY	
DNA ltr dtd 27 Oct 1980 DNA ltr dtd 27 Oct 1980	

THIS PAGE IS UNCLASSIFIED

AD- 357980

SECURITY REMARKING REQUIREMENTS

DOD 5200.1-R, DEC 78

REVIEW ON 31 JAN 78

THIS REPORT HAS BEEN DELIMITED
AND CLEARED FOR PUBLIC RELEASE
UNDER DOD DIRECTIVE 5200.20 AND
NO RESTRICTIONS ARE IMPOSED UPON
ITS USE AND DISCLOSURE.

DISTRIBUTION STATEMENT A

APPROVED FOR PUBLIC RELEASE,
DISTRIBUTION UNLIMITED.

UNCLASSIFIED

AD 357980

CLASSIFICATION CHANGED

TO: UNCLASSIFIED

FROM: CONFIDENTIAL

AUTHORITY: DNA etc,
27 Oct 80



UNCLASSIFIED

WT-1132

This document consists of 95 pages

No. 1 of 245 copies, Series A

Operation TEAPOT

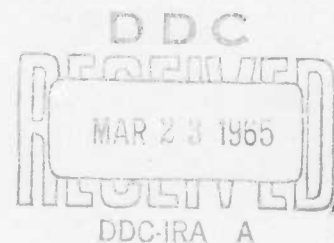
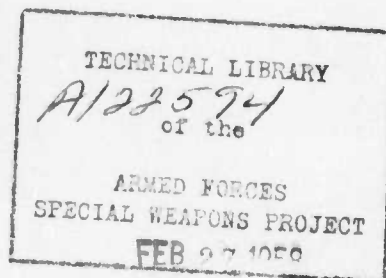
NEVADA TEST SITE

February - May 1955

Project 5.1

DESTRUCTIVE LOADS ON AIRCRAFT
IN FLIGHT

Issuance Date: January 31, 1958



Act of 1954.

This material contains information affecting the national defense of the United States within the meaning of the espionage laws, Title 18, U.S.C., Secs. 793 and 794, the transmission or revelation of which in any manner to an unauthorized person is prohibited by law.

HEADQUARTERS FIELD COMMAND, ARMED FORCES SPECIAL WEAPONS PROJECT
SANDIA BASE, ALBUQUERQUE, NEW MEXICO

EXCLUDED FROM AUTOMATIC
DECLASSIFICATION: E.O. 12812, 5200.10
DOES NOT APPLY

Classification (Cancelled) (Changed to)

By Authority of *Memorandum*


37 *Taylor* Date *2/2/58*

Inquiries relative to this report may be made to
Chief, Armed Forces Special Weapons Project
Washington, D. C.

When no longer required, this document may be
destroyed in accordance with applicable security
regulations. When destroyed, notification should
be made to

AEC Technical Information Service Extension
P. O. Box 401
Oak Ridge, Tenn.

DO NOT RETURN THIS DOCUMENT

 L
⑤ Aeronautical Systems Div., Air Force
Systems Command, Wright-Patterson AFB,
FOREIGN ANNOUNCEMENT AND DISSEMINATION OF THIS REPORT BY DDC Ohio.
IS NOT AUTHORIZED.

⑬ ACC
⑭ WT-1132
⑮ Report on
OPERATION TEAPOT, PROJECT 5.1 [4].

Report to the Test Director


⑥ DESTRUCTIVE LOADS ON AIRCRAFT
IN FLIGHT [4], ⑤

⑩ by Glen F. Purkey and
W.R. Lounsbury, Capt, USAF
and
Staff of Radiation, Inc.
Orlando, Florida

Wright Air Development Center
Wright-Patterson Air Force Base, Ohio

U. S. GOVERNMENT AGENCIES MAY OBTAIN COPIES OF THIS REPORT DIRECTLY
FROM DDC. OTHER QUALIFIED DDC USERS SHALL REQUEST THROUGH

Director
Defense Atomic Support Agency
Washington, D. C. 20301


high and
s. Atomic Energy
Act of 1946

This material contains information affect-
ing the national defense of the United States
within the meaning of the espionage laws,
Title 18, U.S.C., Secs. 793 and 794, the
transmission or revelation of which in any
manner to an unauthorized person is pro-
hibited by law.

SUMMARY OF SHOT DATA, OPERATION TEAPOT

Shot	Code Name	Date	Time*	Area	Type	Latitude and Longitude of Zero Point
1	Wasp	18 February	1200	T-7-4†	762-ft Air	37° 05' 11.6856'' 116° 01' 18.7386''
2	Moth	22 February	0545	T-3	300-ft Tower	37° 02' 52.2654'' 116° 01' 15.6967''
3	Tesla	1 March	0530	T-9b	300-ft Tower	37° 07' 31.5737'' 116° 02' 51.0077''
4	Turk	7 March	0520	T-2	500-ft Tower	37° 06' 18.4944'' 116° 07' 03.1879''
5	Hornet	12 March	0520	T-3a	300-ft Tower	37° 02' 25.4043'' 116° 01' 31.3674''
6	Bee	22 March	0505	T-7-1a	500-ft Tower	37° 05' 41.3880'' 116° 01' 25.5474''
7	ESS	23 March	1230	T-10a	67-ft Underground	37° 10' 06.1263'' 116° 02' 37.7010''
8	Apple	29 March	0455	T-4	500-ft Tower	37° 05' 43.8200'' 116° 06' 09.9040''
9	Wasp'	29 March	1000	T-7-4‡	740-ft Air	37° 05' 11.6656'' 116° 01' 16.7386''
10	HA	6 April	1000	T-5§	36,620-ft MSL Air	37° 01' 43.3642'' 116° 03' 28.2624''
11	Post	9 April	0430	T-9c	300-ft Tower	37° 07' 19.8965'' 116° 02' 03.6860''
12	MET	15 April	1115	FF	400-ft Tower	36° 47' 52.8687'' 115° 55' 44.1066''
13	Apple 2	5 May	0510	T-1	500-ft Tower	36° 03' 11.1095'' 116° 08' 09.4937''
14	Zucchini	15 May	0500	T-7-1a	500-ft Tower	37° 05' 41.3880'' 116° 01' 25.5474''

* Approximate local time, PST prior to 24 April, PDT after 24 April.

† Actual zero point 36 feet north, 426 feet west of T-7-4.

‡ Actual zero point 94 feet north, 62 feet west of T-7-4.

§ Actual zero point 36 feet south, 397 feet west of T-5.



ABSTRACT

The primary purpose of Project 5.1 of Operation TEAPOT was to determine the structural responses and progression of failure in the post-buckling range of aircraft structures when subjected to destructive gust loads produced by a nuclear explosion. Three QF-80 drones, chosen as the test vehicles, participated in full-scale field tests conducted at the Nevada Test Site during Shot 12.

From theoretical calculations and structural test data, it was estimated that the overpressure necessary to produce lethal damage due to gust loading was approximately 3.8 psi. Based on this, three aircraft were to be positioned to receive 2.8, 3.8, and 4.8 psi in an attempt to bracket the lethal volume contour.

The drones were instrumented in anticipation of a bending moment failure of the horizontal stabilizer. Additional instrumentation covered aircraft flight characteristics, structural temperatures, elevator positions, nuclear and thermal radiation, and wing, fuselage, and vertical stabilizer bending moments. The instrumentation systems were backed up by extensive photographic coverage, which was also used to measure wing, fuselage, and horizontal stabilizer deflections. The drone aircraft were positioned at preassigned altitudes by airborne radio and ground radar control and were timed to arrive directly above ground zero at shock arrival.

The complete results of the test are presented in this report. An accumulation of many factors, all tending to reduce the overpressure at the aircraft, produced inputs which were somewhat lower than desired. Although the input to the lowest drone was within the range expected to produce a kill, the lowest drone continued flight after shock arrival and could not be classed as an immediate kill. The basic prediction, that the aircraft was gust critical on the horizontal stabilizer, was confirmed. Valuable data were obtained on the aircraft structural response in the post-buckling range.

FOREWORD

This report presents the final results of one of the 56 projects comprising the Military Effects Program of Operation Teapot, which included 14 test detonations at the Nevada Test Site in 1955.

For overall Teapot military-effects information, the reader is referred to "Summary Report of the Technical Director, Military Effects Program," WT-1153, which includes the following: (1) a description of each detonation including yield, zero-point environment, type of device, ambient atmospheric conditions, etc.; (2) a discussion of project results; (3) a summary of the objectives and results of each project; and (4) a listing of project reports for the Military Effects Program.

PREFACE

Acknowledgment must be given to the following for their cooperation and assistance in the completion of this task:

The Massachusetts Institute of Technology (MIT) Department of Aeronautical Engineering, under Contract to Wright Air Development Center, conducted a theoretical study simultaneously with the experimental preparations for Project 5.1. This study was carried out by E. A. Witmer, N. P. Hobbs, E. S. Criscione, and H. Lin of the MIT Aero-Elastic and Structures Research Laboratory.

The 3215th Drone Squadron, 3205th Drone Group, Air Proving Ground Command, commanded by Lt. Col. A. J. Bregar and Col. E. F. Hocver, respectively, was responsible for maintaining and operating the drone and director test aircraft. Capt. Robert E. Goepfert and Lt. H. W. Lucas were responsible for the operation of the MSQ-1 radar under command of the drone group.

Valuable technical advice and assistance were supplied by personnel of the Air Research and Development Command, Special Weapons Center, Kirtland Air Force Base.

CONTENTS

ABSTRACT	5
FOREWORD	6
PREFACE	6
CHAPTER 1 INTRODUCTION	11
1.1 Objective	11
1.2 Background	11
1.3 Nature and Scope of Investigation	13
1.4 Selection of Aircraft and Input Levels	13
CHAPTER 2 INSTRUMENTATION	17
2.1 Structural Response	17
2.2 Flight Data	20
2.3 Positioning	20
2.4 Timing	20
2.5 Input Measurements	20
2.5.1 Overpressure	20
2.5.2 Thermal Radiation	21
2.6 Response Measurements	21
2.6.1 Response Sign Convention	21
2.6.2 Structural Response	21
2.6.3 Temperature Rise	24
2.6.4 Acceleration	27
2.6.5 Pitch Rate.	27
2.6.6 Elevator Position	27
2.6.7 Photographic Coverage	27
2.6.8 Recording Equipment	27
CHAPTER 3 CALIBRATION	33
3.1 Calibration Method	33
3.2 Strain-Gage Calibration	33
3.2.1 Pure Bending Bridges	33
3.2.2 Tension-Area-Bending Bridges	36
3.2.3 Structural Strain	37
3.3 Pressure Gages	37
3.4 Accelerometers	37
3.5 Rate Gyros	40
3.6 Radiometers and Calorimeters	40
3.7 Airborne Cameras	40
CHAPTER 4 OPERATIONS.	41
4.1 Modification and Instrumentation.	41
4.2 Eglin AFB Operations.	41

4.3	Nevada Test Site Operations	42
4.3.1	Operational Plan	42
4.3.2	Shot 6.	45
4.3.3	Shot 12	45
CHAPTER 5	RESULTS	46
5.1	General	46
5.2	Drone Performance and Visual Damage	46
5.2.1	Drone 1	46
5.2.2	Drone 2	59
5.2.3	Drone 3	59
5.3	Data Acquisition	61
5.3.1	Local Recording	61
5.3.2	Telemetry	63
5.3.3	Airborne Cameras	64
5.3.4	Temp-Tapes.	64
5.3.5	Position Data	64
CHAPTER 6	DISCUSSION.	66
6.1	General	66
6.1.1	Position	66
6.1.2	Damage.	66
6.1.3	Post-Operation Tests	67
6.2	Blast Effects	68
6.2.1	Shock Wave.	68
6.2.2	Normal Acceleration	71
6.2.3	Deflections	71
6.2.4	Bending Moments	81
6.2.5	Elevator Deflection	84
6.3	Thermal Effects	84
6.3.1	Thermal Inputs.	84
6.3.2	Protective Paint	84
6.3.3	Thermal Stress.	85
CHAPTER 7	CONCLUSIONS	90
CHAPTER 8	RECOMMENDATIONS	91
FIGURES		
1.1	Assigned drone positions at time zero with respect to ground zero	14
1.2	Assigned drone positions at shock arrival with respect to ground zero and predicted lethal contour	14
1.3	Calculated overpressure versus height above tower for a 28 kt shot	15
2.1	Aircraft sensing instrument location.	18
2.2	Airborne camera locations and fields of view.	19
2.3	Aircraft stations diagram	22
2.4	Typical strain gage bridge installation for horizontal stabilizer structural strains (single-active-arm).	23
2.5	Typical wing root bending moment bridge installation (four-active-arm).	25

2.6	Typical fuselage bending moment bridge installation (four-active-arm).	25
2.7	Typical horizontal stabilizer strain gage installation	26
2.8	Typical horizontal stabilizer bending moment bridge installation (two-active-arm multiple-gage)	26
2.9	Airborne camera coverage as photographed during dry-run flight	28
2.10	Left side cockpit camera installation	29
2.11	Right side cockpit camera installation	29
2.12	Telemeter pod installation	30
2.13	Recorder pod installation	31
3.1	Sample calibration curve.	34
3.2	Wing calibration.	35
3.3	Fuselage calibration.	35
3.4	Vertical stabilizer calibration	36
3.5	Whiffletree loading fixture for horizontal stabilizer static calibration	38
3.6	Horizontal stabilizer calibration	39
3.7	Deflection calibration points	39
4.1	Basic flight pattern for drone aircraft	43
4.2	Nevada Test Site area showing drone flight plan	44
5.1	Actual versus planned altitude, relative ground position, and velocity at shock arrival, Drone 1	50
5.2	Actual versus planned altitude, relative ground position, and velocity at shock arrival, Drone 2	50
5.3	Actual versus planned altitude, relative ground position, and velocity at shock arrival, Drone 3	51
5.4	Horizontal stabilizer deflection, Station 94 Left, Drone 1	51
5.5	Horizontal stabilizer deflection, Station 94 Right, Drone 1	52
5.6	Wing deflection, Station 213 Left, Drone 1	52
5.7	Wing deflection, Station 213 Right, Drone 1	53
5.8	Horizontal stabilizer deflection, Station 94 Left, Drone 2	53
5.9	Horizontal stabilizer deflection, Station 94 Right, Drone 2	54
5.10	Wing deflection, Station 213 Left, Drone 2	54
5.11	Wing deflection, Station 213 Right, Drone 2	55
5.12	Horizontal stabilizer deflection, Station 94 Left, Drone 3	55
5.13	Horizontal stabilizer deflection, Station 94 Right, Drone 3	56
5.14	Wing deflection, Station 213 Left, Drone 3	56
5.15	Wing deflection, Station 213 Right, Drone 3	57
5.16	Visual damage, Drone 1	58
5.17	Visual damage, Drone 2	60
5.18	Visual damage, Drone 3	62
6.1	Shock wave time of arrival versus slant range	69
6.2	Peak overpressure versus slant range.	70
6.3	Horizontal stabilizer deflection at shock arrival, Drone 1	72

6.4	Horizontal stabilizer deflection at shock arrival, Drone 2	75
6.5	Horizontal stabilizer deflection at shock arrival, Drone 3	78
6.6	Fuselage deflection versus time after T_0 , Station 373, Drone 2	82
6.7	Horizontal stabilizer apparent bending moment, Station 43 Left, Drone 1.	82
6.8	Comparison between peak bending moments and limit loads, Drone 1	83
6.9	Elevator deflection, Station Zero, Drone 1	83
6.10	Thermal curves, Drone 1.	85
6.11	Thermal curves, Drone 2.	86
6.12	Thermal curves, Drone 3.	87

TABLES

4.1	Aircraft Identification	42
5.1	Summary Shot Data	47
5.2	Test Conditions	47
5.3	General Test Results.	48
5.4	Temp Tape Measurements	48
5.5	Peak Deflections.	49
5.6	Maximum Stabilizer Apparent Bending Moment During Thermal Input Period	49
5.7	Data Recording Systems	49
6.1	Post-Operation Static Tests of Drone Horizontal Stabilizers	68

CONFIDENTIAL

Chapter I INTRODUCTION

1.1 OBJECTIVE

Project 5.1 was planned to investigate the response of aircraft structures in flight to the blast effects from a nuclear explosion. In particular, it was desired to experimentally verify the inputs necessary to produce lethal damage to the aircraft and the responses of the aircraft to their destructive loads. Measurements were planned to secure structural behavior data in the post-buckling range to determine the phenomena and progression of structural failure. This would provide a check for theoretically calculating lethal volumes for aircraft.

1.2 BACKGROUND

This project was carried out in support of a theoretical lethal volume study by WADC conducted at the Department of Aeronautical Engineering of the Massachusetts Institute of Technology. The purpose of this theoretical study was to determine an analytical procedure for estimating the destruction of aircraft in flight by a nuclear explosion. It was intended that these procedures could then be used to formulate a general theory of destruction which would lead to the definition of a lethal volume contour. Questions of what would constitute a satisfactory kill were highly debatable. Therefore, in this project, damage to primary aircraft structural components sufficient to prevent continued flight of the aircraft was considered a kill. This necessarily excluded radiation effects on the pilot, since he might well sustain a lethal dose of radiation and still live long enough to complete his mission.

Previous investigations of the blast effects on aircraft in flight were limited to "safe delivery" tests. In those tests the objective was to determine the level of thermal and blast inputs from a nuclear explosion which could be sustained by an aircraft delivering the weapon without inflicting permanent damage to the aircraft. In that type of operation it was necessary to position the test aircraft at a considerable distance from air zero and in an attitude to sustain the least-possible damage. Naturally, the resulting blast loads were relatively low and were limited to the linear range below the elastic limit of the structural elements. Consequently, data from these tests were insufficient to determine structural failure phenomena.

In order to check the validity of the theory of destruction when applied to a particular structure, it was necessary to choose a typical

aircraft that could be subjected to the test. The F-80 was selected as a test aircraft for Project 5.1, since it was the only available proven jet drone. An analysis was then made of the F-80 aircraft that indicated that the horizontal stabilizer was the critical structural component.

An investigation was undertaken to determine by static test and existing structural response data, the approximate loads required to produce bending moment failure of the horizontal stabilizer. A laboratory static-test program was carried out to obtain additional structural information under controlled conditions and to assist in the selection of the proper location for strain-gage instrumentation. Two stabilizers were loaded to destruction at Wright Air Development Center and three more at Massachusetts Institute of Technology. Data from these break tests were reduced and analyzed. A complete report on the static test program is presented in the following document: D'Amato, Richard, "Destruction Tests of Aircraft Structural Components," WADC Technical Report 54-385, Part I, Massachusetts Institute of Technology, 1 June 1955.

The drone test positions were planned with the purpose of bracketing the lethal volume contour. It was intended that the aircraft structure would be exposed to the same order of inputs required for destruction and near destruction as predicted by use of the MIT analysis. By observations of the test results, it was expected that the theory would be proven or modified as indicated necessary by the experimental results. If the theory could be validated in this manner, it could be used to predict theoretically the in-flight response characteristics for any aircraft type whose structural details were available. Then, for any given input conditions or weapon yield, lethal gust volumes could be devised for any aircraft under a specific set of flight conditions.

It was intended that the results of this program would ultimately be extrapolated to shots of very low yield. However, successful completion of the test required a much larger shot (approximately 25 KT) to insure that the expected drone position errors would not appreciably alter the inputs to the drones. A single-peak, ideal-type, shock wave was desired in which all reflections or other spurious signals would be eliminated. This was necessary in order to eliminate the complex effects on loading and resonance that would occur with arrival of a reflected shock wave and to stimulate the free-air characteristics of an antiaircraft detonation at altitude. However, problems involving timing and coordination of delivery eliminated the possibility of using an air burst for this test, and a surface burst of adequate yield could not be used at the Nevada Test Site because of off-site fallout limitations. There remained the possibility of a low tower shot, which would be satisfactory only if the reflected wave merged with the incident wave to form a single-peak shock wave.

The operational plan called for each drone to be directly above air zero at the time of shock arrival. Therefore, the shock wave was of particular interest only in a narrow cone directly over the burst point. Results from previous nuclear tests had indicated that the reflected shock wave might be greatly accelerated as it passed back through the air which had previously been heated by the fireball. If this were true, the reflected wave would catch up and merge with the incident

wave directly above the burst point. If such a merger took place before the shock wave reached the lowest drone, the shock wave characteristics would be suitable for Project 5.1.

1.3 NATURE AND SCOPE OF INVESTIGATION

The primary data for Project 5.1 were obtained during full-scale participation in Shot 12 of Operation Teapot. Since previous experience had shown that some difficulty might be expected from recording and telemetering equipment in this type of test, it was desired to check out this equipment early in the operation. It was also desired to test the complete instrumentation and data-recording systems under conditions similar to those expected during the actual test. This was accomplished by manned participation of one drone in Shot 6. (For a description of the general characteristics of all shots of interest in this report, see Table 5.1.)

In view of the stringent requirements for shock wave characteristics for Project 5.1, it was necessary to verify prior to actual test participation that the incident and reflected shock waves for a similar shot would merge at a sufficiently low altitude. This was accomplished by Project 1.2 during Shot 4 which was also a low tower shot and was quite similar to Shot 12.

Three QF-80 drones were scheduled for full-scale participation in Shot 12. Each drone was timed to arrive directly above ground zero at shock arrival. In Figure 1.1 are shown the assigned drone positions at time zero with respect to ground zero. The aircraft were positioned to bracket the calculated lethal volume contour, as shown in Figure 1.2. It was intended that Drone 3 be so severely damaged that it would not support normal flight load, that Drone 2 would sustain severe damage with possible failure, and that Drone 1 would be lightly damaged and capable of continued flight. Aircraft altitudes above the burst point, i. e. slant range, were assigned as follows:

Drone 3	3,800 feet
Drone 2	4,300 feet
Drone 1	5,100 feet

The tower base was 3,077 feet above mean sea level.

The tower height was 400 feet.

1.4 SELECTION OF AIRCRAFT AND INPUT LEVELS

The QF-80 was the logical choice as a test vehicle for this project. It was the only proven drone available in sufficient quantity, and there was a large volume of analytical and test data available on the structural characteristics. The QF-80 was selected only as a typical test specimen, however, and the use of this particular aircraft does not in any way imply a limitation of the theory. There were many possible variations in test conditions, including yield, calculated inputs, calculation of aircraft response, and aircraft position. It was decided that three aircraft positioned at different altitudes would be

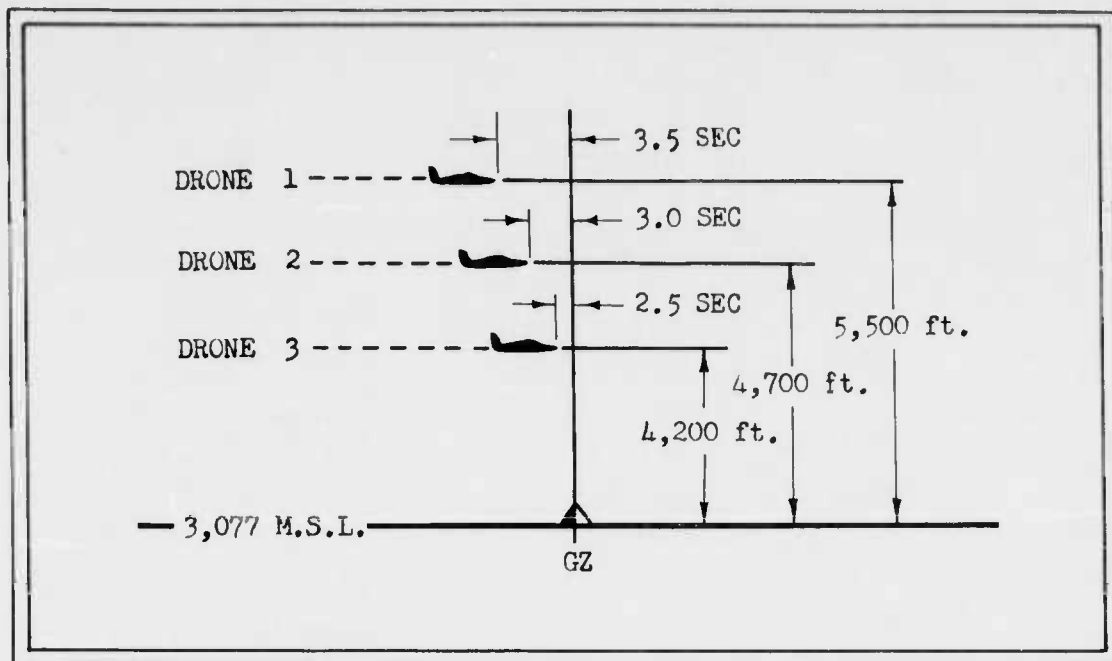


Figure 1.1 Assigned Drone Positions at Time Zero with Respect to Ground Zero

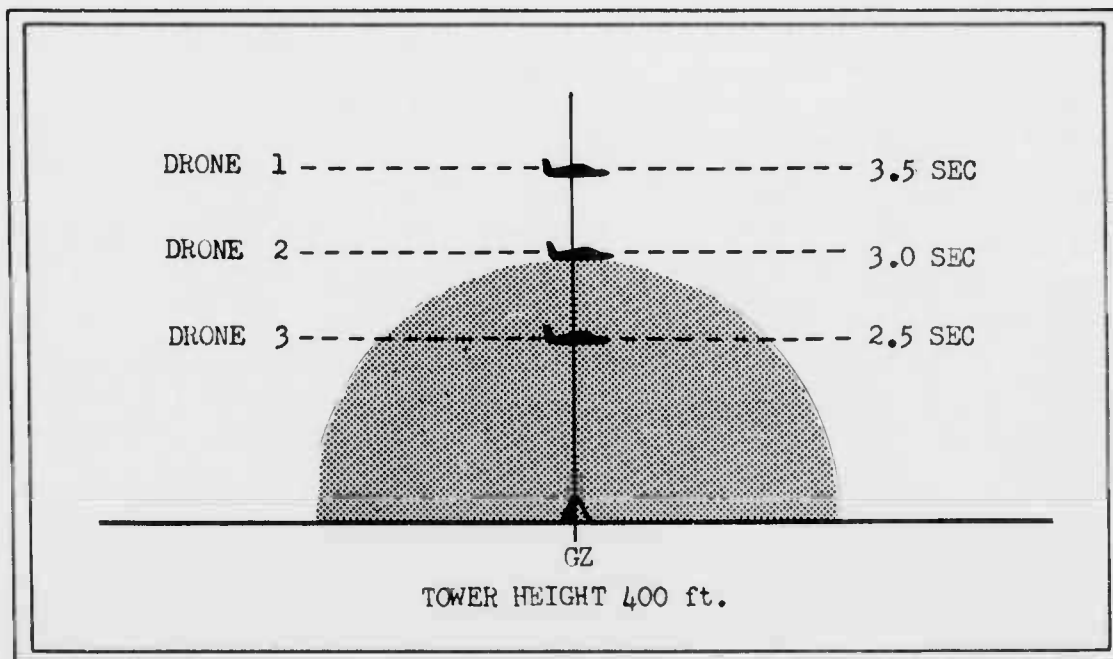


Figure 1.2 Assigned Drone Positions at Shock Arrival with Respect to Ground Zero and Predicted Lethal Contour

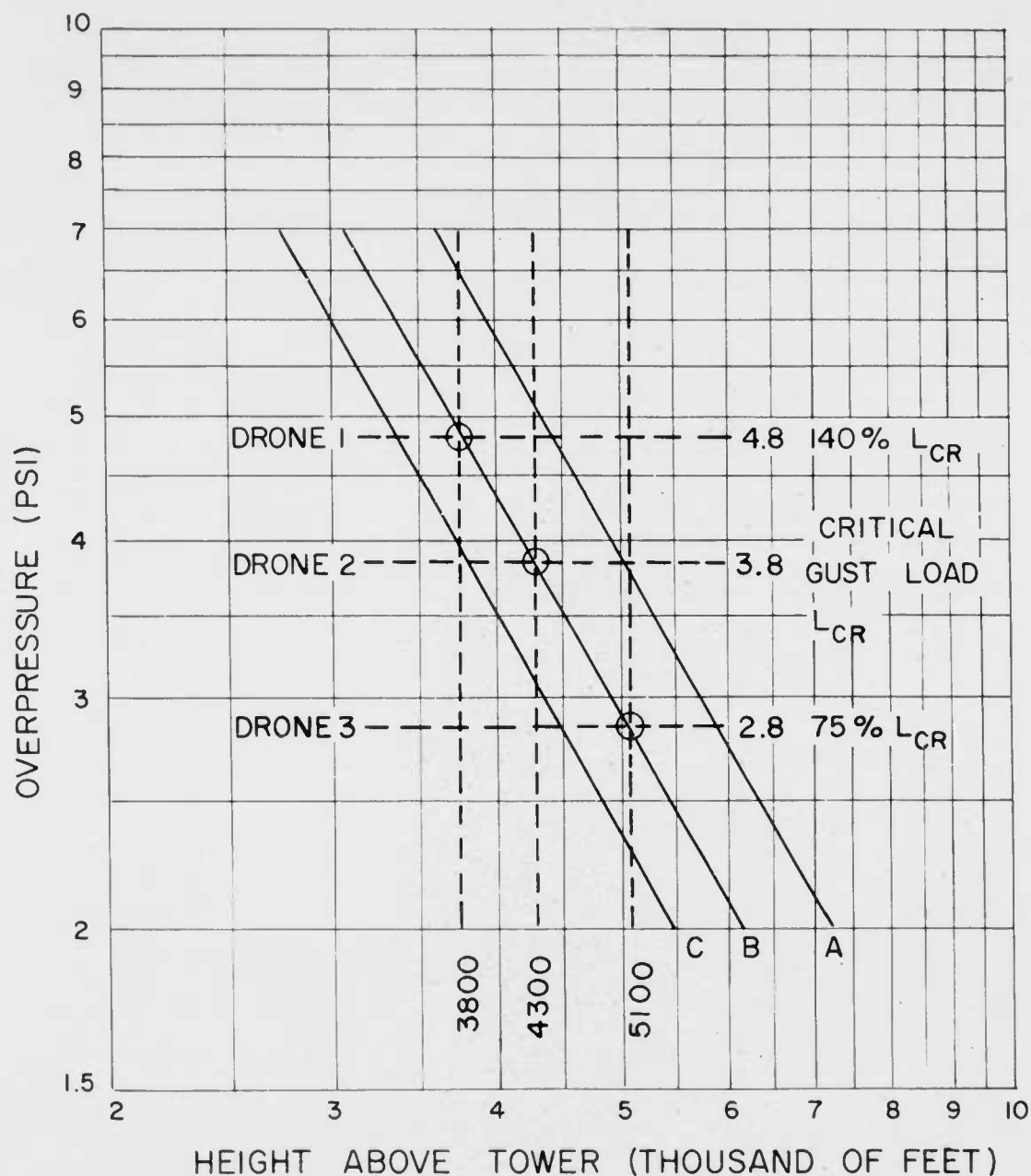


Figure 1.3 Calculated overpressure versus height above tower for a 28 KT shot. A, Maximum expected value, based on 2 times yield plus 10 percent yield plus 5 percent pressure; B, Best calculated value, overpressure based on 1.2 times yield as indicated by data from Shot 4; C, Minimum expected value, based on 1 times yield minus 10 percent yield minus 5 percent pressure.

required to attain a high probability of bracketing the input level required to just produce destruction.

In connection with the safe-delivery problem, analytical methods have been developed for calculating inputs at specified distances from a nuclear explosion and the responses of aircraft to these inputs in the elastic-deformation range. In the planning for this lethal volume test, an attempt was made to extend these methods to determine the gust velocity required to produce failure of the QF-80 horizontal stabilizer. This critical gust velocity was then related to peak overpressure, which in turn established the position for the specified yield. The value of overpressure thus calculated to be critical was approximately 3.8 psi. The other two aircraft positions were based on 75 percent and 140 percent of the critical gust loading, which corresponds to 2.8 and 4.8 psi, respectively. A graph of calculated overpressure versus height above the tower for a 28 KT shot is presented in Fig. 1.3. This graph was prepared by the Test Director and his advisors, based upon the data obtained from Shot 4, and the expected limits of inputs are indicated. The necessary aircraft positions at shock arrival are taken from this curve. The drones were positioned by use of the standard close Support Control Set AN/MSQ-1, which was designed to track an aircraft or missile in flight. This system consists of a ground radar station for each aircraft, which tracks the aircraft in flight and provides a continuous plot of its ground track; a record of its height, ground speed, and azimuth and range as measured from the system location; and indication of the aircraft distance and bearing from a fixed target point. Also provided are facilities to enable communications between the system controller and the pilot for guidance purposes. The MSQ-1 system was used in conjunction with the APW-11 command set so that the operator at the MSQ-1 ground station could control the airplane during the test run. The position limits for the drones were based on the expected best obtainable accuracy of the MSQ-1. These limits were ± 150 yards lateral error, ± 150 feet in altitude, and $\pm 1,250$, $\pm 1,450$, and $\pm 1,660$ feet of horizontal range for Aircraft 3, 2, and 1, respectively. These tolerances are considered acceptable for the test.

Chapter 2

INSTRUMENTATION

Because of the severe nature of conditions to be encountered in the instrumented aircraft, it was decided to use two systems for obtaining input and aircraft-response data. These instrumentation systems used identical sensing devices but differed in the manner in which the sensed data were recorded. One system employed recording oscillographs carried in the aircraft. The other channeled the data over a radio-telemetry link to ground recorders. These systems were, in turn, backed up by extensive photographic coverage. Remote control of the recorders and cameras was necessary, since the aircraft were not manned. All aircraft were instrumented identically, since complete interchangeability was essential. Figure 2.1 shows the location of all instruments installed directly in the aircraft. A more-detailed description of the instruments and installation used in this project is given in Volumes I and II of "Equipment Report" (February 1955), prepared by Radiation, Inc., for WADC on Contract AF 33(600)-19270.

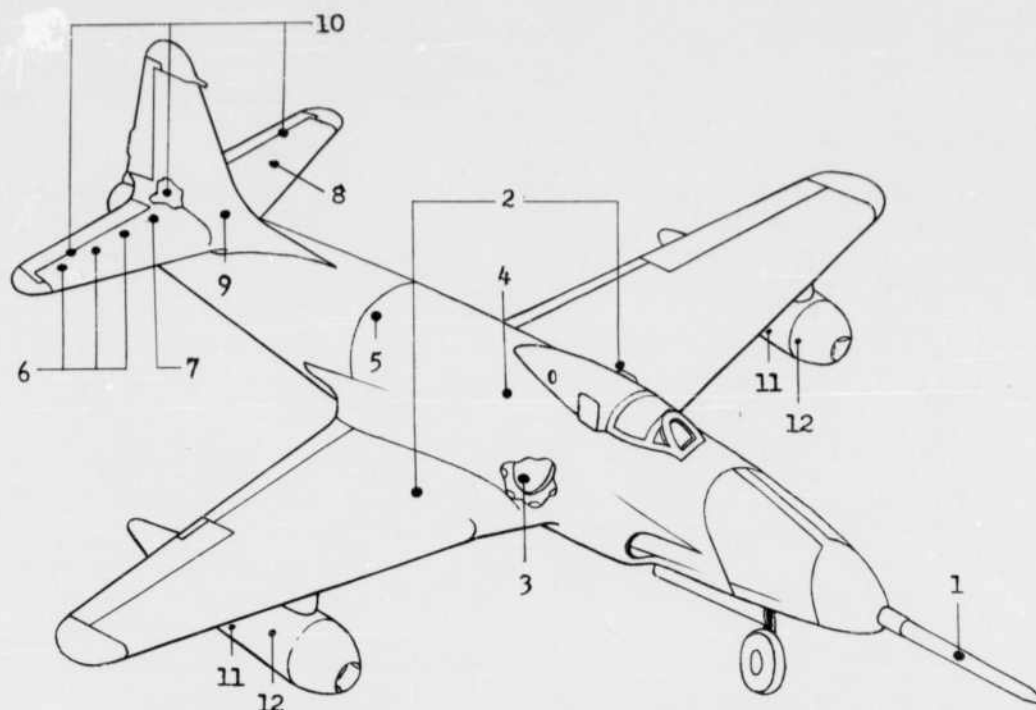
Transducers, recording equipment, and cameras were selected on the basis of: (1) ability to provide necessary data; (2) reliability and relative insensitivity to adverse environmental conditions; (3) size and weight; and (4) availability.

The aircraft were instrumented primarily to measure structural responses. Additional measurements were made of aircraft flight characteristics together with records of blast-imposed inputs. Photographic coverage of flight data and aircraft response, as shown in Figure 2.2, completed the instrumentation.

Since all of the test drones were not expected to return safely to base, it was necessary to provide a system through which the recorded data could be recovered, even though the aircraft were lost. This was done by means of a jettisoning system. All recording equipment was housed in two jettisonable pods under the wings and in the jettisonable cockpit canopy. The jettisoning system could be operated by remote control from the director aircraft and was arranged to effect automatic jettison in the event of either remote-control carrier failure or a primary power failure.

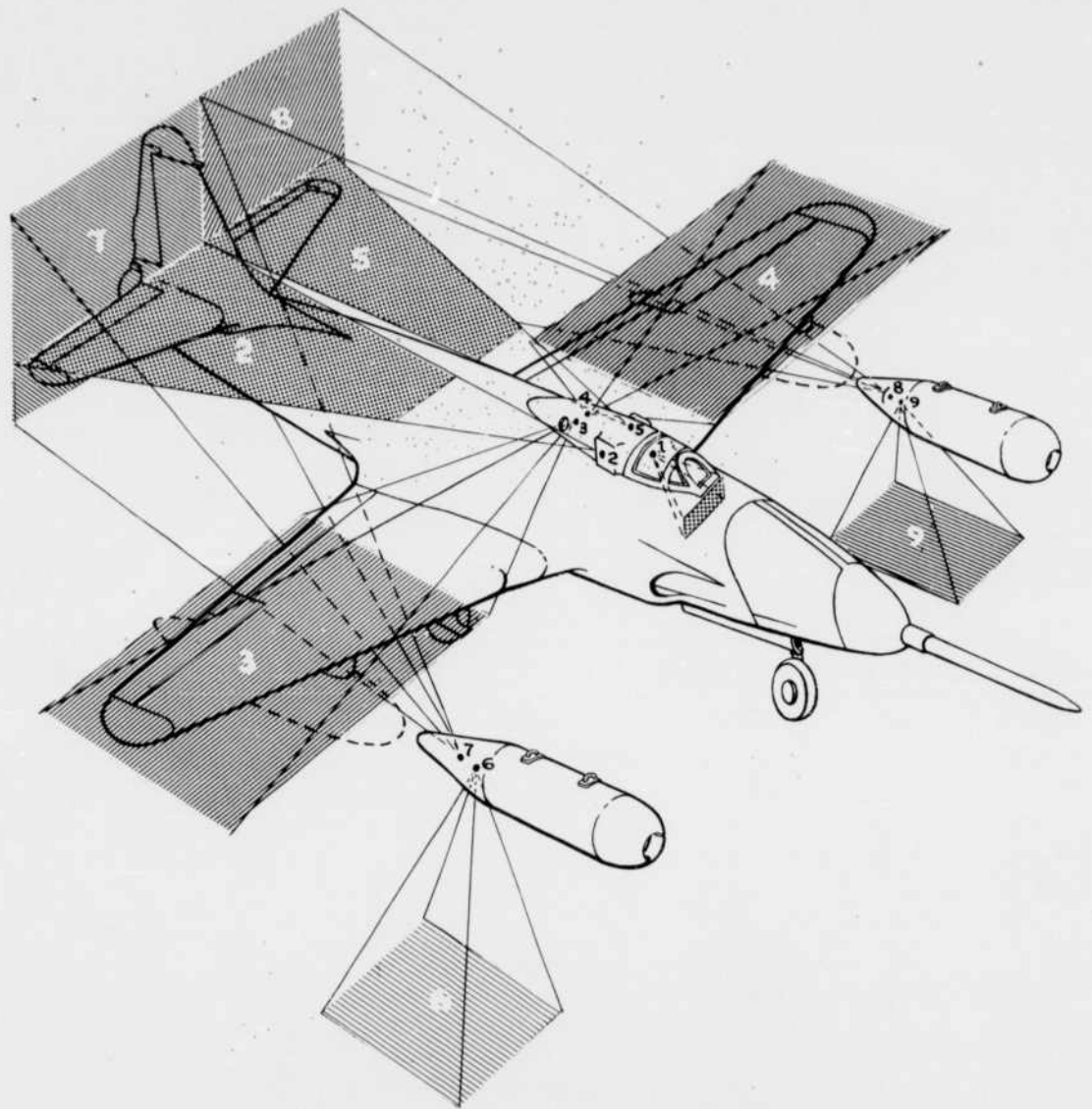
2.1 STRUCTURAL RESPONSE

The major portion of the aircraft instrumentation was devoted to the measurement of the structural behavior of the horizontal stabilizer. This particular component of the aircraft was considered to be critical to upward gust loading. Strain gages were extensively used to measure the strains in the individual structural elements, as well as to measure the stabilizer bending moment at stations selected on the basis of laborato-



No	INSTRUMENT USED	QUANTITY MEASURED	COMPONENT LOCATION
1	Pressure Transducer	Free-Air Over Pressure	Nose Boom Fus. Sta. -30
2	Strain Gages	Wing Root B.M.	Wing Sta. 40
3	Linear Accelerometers	Vertical Acceleration	Fus. Sta. 209 Left Wheel Well
4	Rate Gyros	Rate-of-Pitch	Fus. Sta. 225
5	Strain Gages	Fus. B.M.	Fus. Sta. 270
6	Strain Gages	Horiz.Stab. B.M.	H. Stab. Stas. 33, 43 & 52 L & R
7	Strain Gages	Horiz. Stab. Struct.Strain	H. Stab. Sta. 10 to 20 L & R
8	Resistance Thermometer	Horiz.Stab.Temp.	Left Side Horiz. Stab. Sta. 30
9	Strain Gages	Vert.Stab. B.M.	Vert. Stab. Sta. 125
10	Precision Potentiometer	Elevator Position	Horiz. Stab. Stas. 0 and 60
11	NRDL Calorimeters	Thermal Input	Tel. & Rec. Pods
12	NRDL Radiometer	Thermal Energy	Tel. & Rec. Pods

Figure 2.1 Aircraft Sensing Instrument Location



P. No.	LOCATION	COVERAGE
1	Cockpit Canopy	Inst.-Panel, Airspeed Indicator, & Altimeter
2	Cockpit Canopy	Right Side Horizontal Stabilizer & Fuselage
3	Cockpit Canopy	Right Wing Wing Deflection & Skin Buckling
4	Cockpit Canopy	Left Wing Wing Deflection & Skin Buckling
5	Cockpit Canopy	Left Side Horizontal Stabilizer & Fuselage
6	Recorder Pod	Ground
7	Recorder Pod	Right Side Horizontal Stabilizer & Fuselage
8	Telemeter Pod	Left Side Horizontal Stabilizer & Fuselage
9	Telemeter Pod	Ground

Figure 2.2 Airborne Camera Locations and Fields of View

ry static destruction tests. Other structural response instrumentation included wing root, fuselage, and vertical stabilizer bending moment bridges.

Early static destruction tests showed a tendency for the stabilizer to break inboard of Stations 10 Left and 10 Right. Since this greatly reduced the possibility of obtaining good break data, a structural reinforcement similar to that of the T-33 stabilizer was installed. This resulted in all further breaks falling outside of Station 10. Also, in the first two breaks, the front attachment fitting on the stabilizer broke due to its being under extreme bending stress. The structural reinforcement eliminated any further breakage of the fitting.

2.2 FLIGHT DATA

A camera was located in the cockpit area attached to the jettisonable canopy to record airspeed and pressure altitude. The instruments standard for the aircraft, Type F-2 airspeed indicators and Type AN5760-2 aneroid altimeters.

2.3 POSITIONING

Location of the aircraft in space was by triangulation using ground-based phototheodolites. These data were backed up by the data supplied by the MSQ-1 positioning radar and the time history plots made at the ground control stations. Additional backup was provided by the WLAMC data recorders that photographically recorded the position data supplied by the MSQ-1 radar. The accuracy of the two backup data systems is essentially that of the MSQ-1 itself.

2.4 TIMING

Data were correlated by coded time marks generated by a Berkeley Model 501 Time Reference Generator synchronized with range time at T-15 seconds. It was planned to record time marks directly on the ground-based recorders along with the telemetered data. Keyed audio tones were transmitted to the aircraft via a VHF link where they were decoded and applied to the airborne recorders. Special neon lamps installed in the camera film magazines provided time reference marks for the photographic data.

2.5 INPUT MEASUREMENTS

2.5.1 Overpressure. Statham Laboratories, Inc. Model P81 K pressure transducers were installed to measure overpressure. These unbonded strain-gage instruments were selected for their high degree of damping. They were 0 to $\frac{1}{2}$ 8-psi instruments with approximately critical damping.

It was necessary to employ temperature compensation to hold zero shift to $\frac{1}{2}$ 1 percent of full scale per 100°F. The gages were located in a nose boom in order to measure free-air overpressure independent of turbulence and reflection effects from the airframe.

Three gages were installed in the boom with their reference ports fed to a common reference chamber. This chamber had a needle valve in-

take which was adjusted for a 3-minute time constant. Thus the gage installations were designed to read overpressure referred to ambient pressure just before shock arrival.

2.5.2 Thermal Radiation. Radiometers and calorimeters developed by the U. S. Naval Radiological Defense Laboratory (NRDL) were installed to measure both time history of intensity and total thermal radiation input data. The radiometers, designed MK 6-F, operated in the energy range of 0 to 250 calories/cm²/sec and delivered 10 millivolts output at their design maximum. Each unit was linear to \pm 5 percent, and was considered accurate to \pm 10 percent. The calorimeters employed to measure the total thermal radiation at the test aircraft were selected to cover the range of 100 calories/cm². Linearity and accuracy were comparable to that of the radiometers. The thermal-radiation-input instrumentation was designed for both telemetering and local recording. Cameras were mounted parallel to the axis of the calorimeters and radiometers to provide a correction factor due to incidence angle and to record any unusual atmospheric circumstances, such as small clouds between aircraft and ground.

One radiometer and one calorimeter were mounted in the recorder pod. Two calorimeters and one radiometer were mounted in the telemeter pod.

2.6 RESPONSE MEASUREMENTS

2.6.1 Response Sign Convention. To eliminate misunderstanding and provide a reference for quickly ascertaining direction of response, an arbitrary sign convention has been employed in presenting data in this report. The following effects are considered positive: (1) Acceleration, normal, an increase in the upward velocity or decrease in the downward velocity of the aircraft or any component thereof; (2) Bending (aft fuselage), tail deflection upward, upper surface compression; (3) bending (wings and stabilizers), tip deflection upward, upper surface compressions; (4) elevator position, elevator deflected upward; (5) overpressure, differential pressure above ambient; (6) pitch rate, tail deflection downward, nose deflection upward; and (7) structural strain, tension load or elongation.

2.6.2 Structural Response. The purpose of the strain-gage installation in this operation was to measure bending moment and structural strains. Shear and torsion were of no interest, except as they affected the bending moment readings.

Strain gages bonded to the aircraft structural members were used in all measurements involving structural response. Due to the anticipated thermal rise, Baldwin EBDF-7D temperature-compensated gages were used in all applications, except those where the strain was expected to exceed the proportional limit. In those cases Baldwin PA-3 post-yield gages were used.

Generally all of the EBDF-7D gages were applied with phenolresin cement under pressure with a heat-curing cycle. The only exception were the gages in the wheel well where heat could not be applied, in which case Armstrong A-6 cement was used. The PA-3 gages were applied

with a special cement supplied by Baldwin. Protection from weather and liquids was provided by a semi-soft plastic compound, Products Research PR-1201, normally used as a fuel tank sealer. This protective coating was also applied to short lengths of wire leading from strain-gage ter-

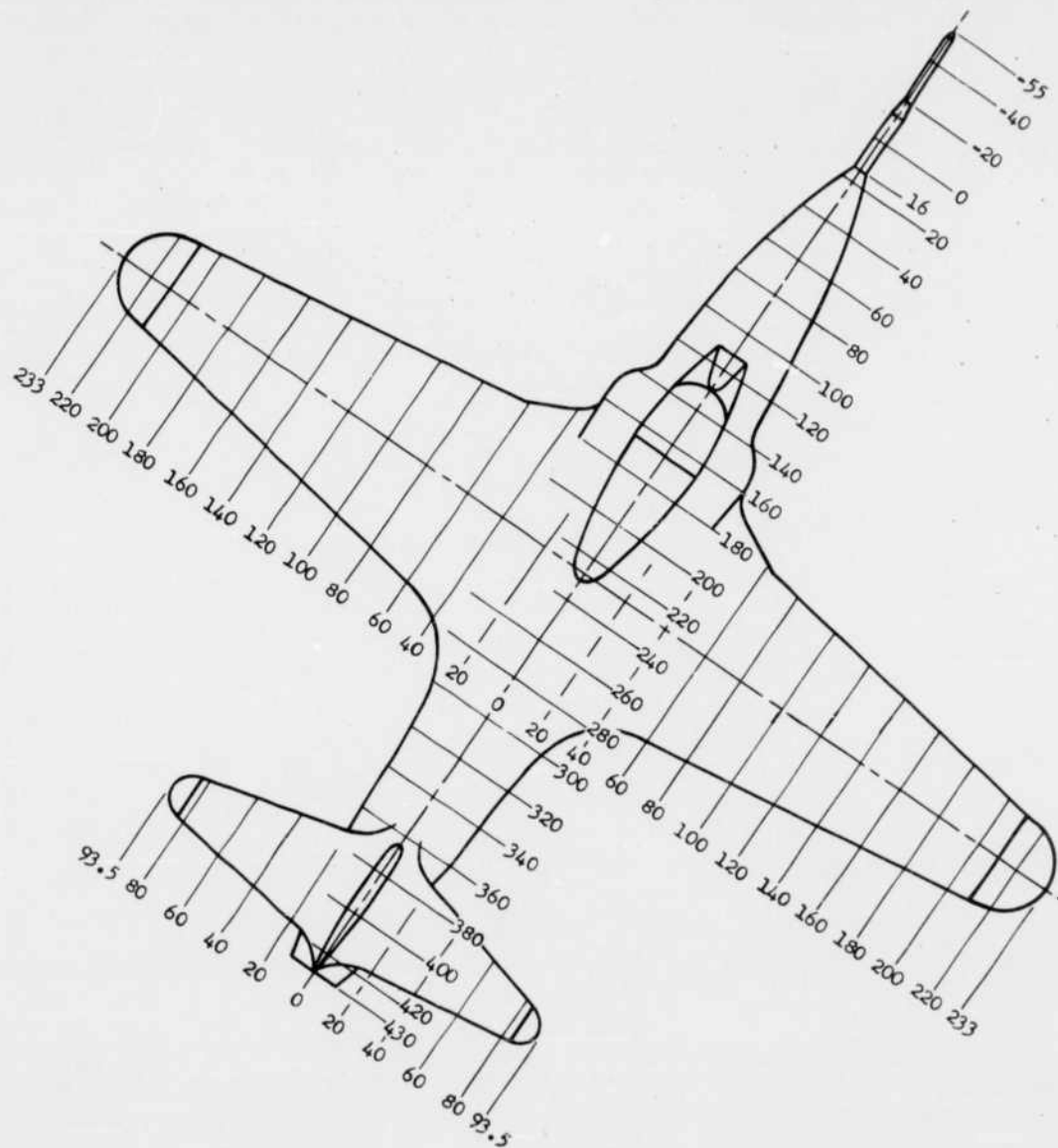


Figure 2.3 Aircraft Stations Diagram

minal boards to seal as well as restrain the wires from excessive motion.

As an aid in determining location of strain gages and other instruments used in this program, an aircraft stations diagram is shown in Figure 2.3.

Structural Strain Measurements. The main object in measuring structural strains was to provide a time history of progression of fail-

ure of horizontal stabilizers exposed to excessive uploading. Secondly, a quantitative measure of post-buckling strains in the area of failure was desired. Stress analysis and static test data on the QF-80 stabilizers had shown that the critical bending stations were Stations 10 and 20 and Stations 40 to 50. The destruction tests conducted at WADC and MIT confirmed this data and showed that the most-probable-break stations were in the region of Stations 10 to 20. Due to the limited number of recording channels, it was not possible to completely instrument both critical areas. Therefore, post-yield strain gages were in-

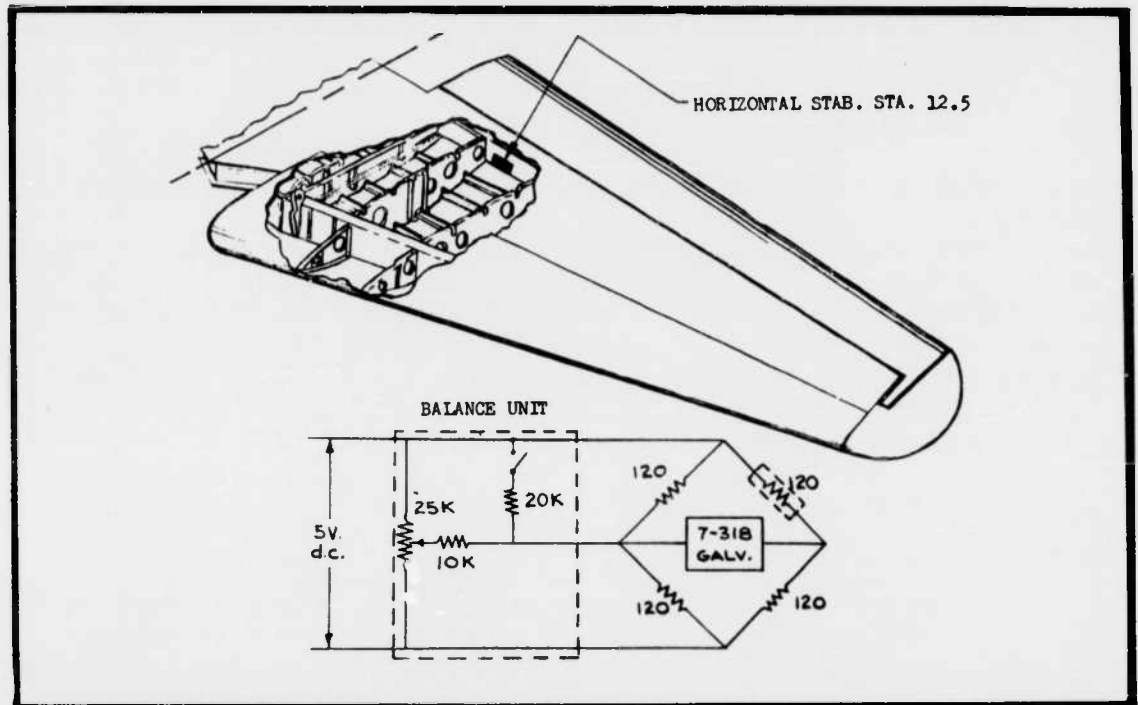


Figure 2.4 Typical Strain Gage Bridge Installation for Horizontal Stabilizer Structural Strains (Single-Active-Arm)

stalled on the front and rear spars and on the upper skin stringers only in the region of Stations 10 to 20.

These gages were Baldwin Type PA-3 gages capable of measuring up to 10 percent strain before gage failure. There was a total of 15 structural strain gages on each semispan of each stabilizer. Nine of these gages were connected into single-active-arm Wheatstone Bridges as shown in Figure 2.4. Due to the limited number of recording channels allotted to the structural strain measurements the remainder of the gages were connected to form three two-active-arm bridges to provide adequate coverage of the expected break station.

Bending-Moment Measurements. Bending-moment-measuring stations were at wing Station 40, fuselage Station 270, vertical-stabilizer Station 126 and horizontal-stabilizer Stations 33, 43, and 52. All gages used for bending moment measurements were Baldwin Type EBDF-7D. For the wing, fuselage, and vertical stabilizer, the gages were connected in a conventional four-active-arm bending bridge with gages installed

top and bottom of the main structural members only. In these installations each gage location and all bridge circuits were so selected that the bridges were essentially insensitive to shear, torsion, and end-loading. Gages were placed on the front and rear main spars of wings and vertical stabilizers as shown in Figure 2.5. Fuselage bending moment gages were installed on three main longerons as shown in Figure 2.6.

For the horizontal stabilizer bending moments, it was necessary to depart from the installation as used on the other components. In this operation the strain gages mounted on the upper surface compression areas were expected to give erroneous readings under critical loading conditions, due to the extensive buckling of these surfaces. During the static test phase of the program at MIT, the following procedure was used to develop a method of instrumentation to accurately measure these bending moments.

The horizontal stabilizer bending moment stations were extensively instrumented with gages on both compression and tensile members, as shown in Figure 2.7.

The individual outputs of these gages were then recorded for known loading conditions. Several combinations of strain gages were selected, and the load-carrying area represented by each gage was calculated for each combination. The bending moment at the station was then obtained as follows:

$$M = K \sum s_1 A_1 d_1 + s_2 A_2 d_2 + \dots + s_n A_n d_n \text{ (Eq. 2.1)}$$

Where: K = calibration constant

s = measured stress in individual element
(tension is positive, compression is negative)

A = Calculated effective area for individual element

d = distance from gage to arbitrarily chosen reference axis

Different gage combinations were tried until the one combination was found which most accurately represented the known bending moment at the measuring station while using the smallest number of gages. The combination finally selected was arrived at by letting the reference axis pass through the upper-surface compressive areas, thus cancelling out the erroneous reading in these elements. Several of the remaining gages were then selected and connected electrically into two-active-arm multiple-gage Wheatstone bridge circuits, which gave a resulting output proportional to the actual bending moment. The horizontal-stabilizer bending-moment bridge installation is shown in Figure 2.8.

This testing program confirmed the theory that the bending moment beyond the elastic limit of the structure can be accurately measured by instrumenting only the tensile elements. For a detailed explanation of the reasoning and calculation involved in developing this method of instrumentation, see WADC Technical Report 54-385, Part II, Massachusetts Institute of Technology.

2.6.3 Temperature Rise. It was anticipated that thermal stress due to the thermal radiation input would not be sufficient to cause a large error in gust-effect measurements. However, temperature gages were placed at several significant points on the skin, spars, and stringers about

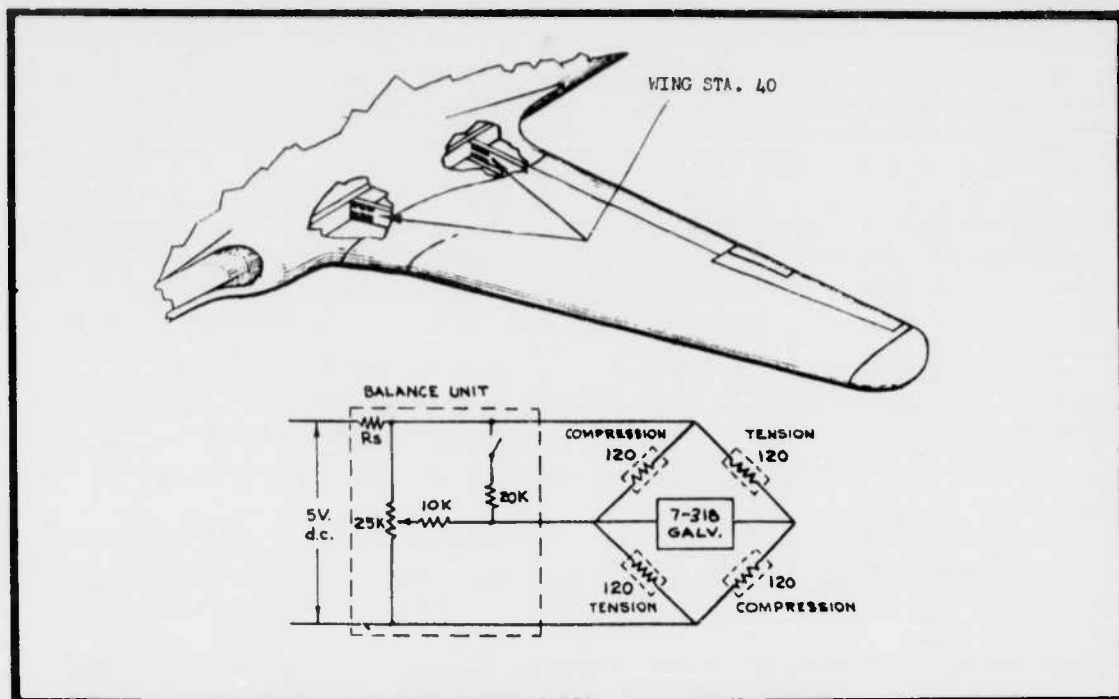


Figure 2.5 Typical Wing Root Bending Moment Bridge Installation (Four-Active-Arm)

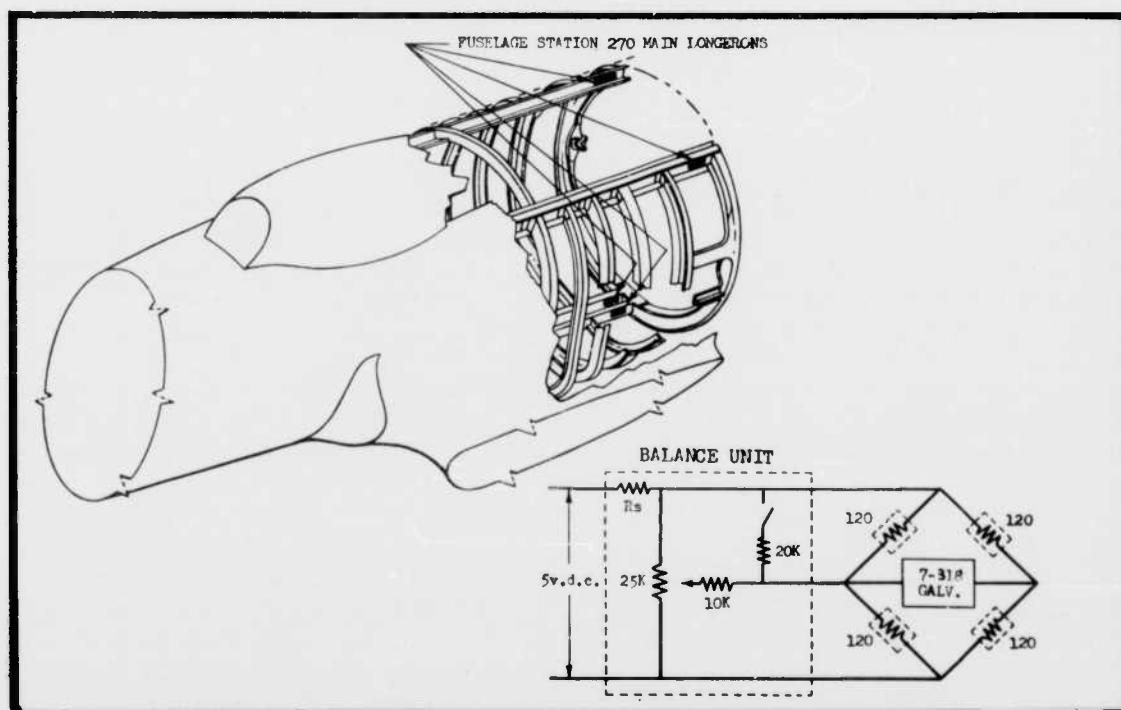


Figure 2.6 Typical Fuselage Bending Moment Bridge Installation (Four-Active-Arm)

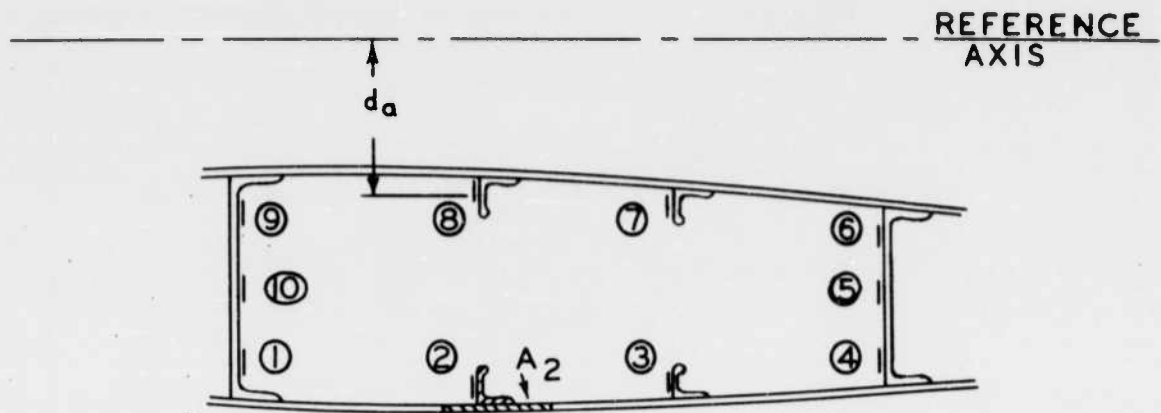


Figure 2.7 Typical Horizontal Stabilizer Strain Gage Installation

the structure so that the temperature effects could be determined. Baldwin TB-14 gages were selected on the basis of satisfactory response and convenience of application. Tests were run in which several types of thermocouples and the TB-14 gages were subjected to high rates of temperature rise. Only a thermocouple composed of 0.010-inch-diameter wire gave a shorter rise time than the TB-14 gage. However, since the rise time of the thermocouple was not appreciably shorter and due to the necessity of using a chopper for telemetering any DC functions, the

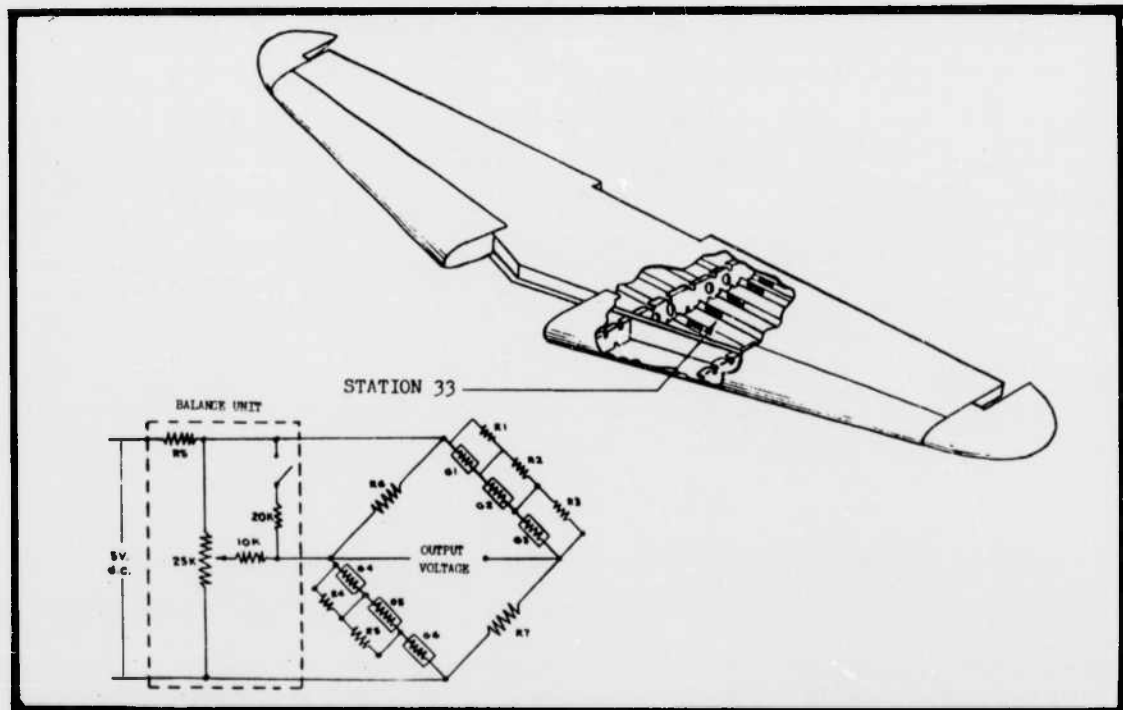


Figure 2.8 Typical Horizontal Stabilizer Bending Moment Bridge Installation (Two-Active-Arm Multiple-Gage)

TB-14 gages were chosen. The high temperature rises expected were great enough to completely mask any errors due to mechanical strain of the temperature gages.

As a back-up measurement, "Temp-Tapes," both of the type developed by University of Dayton and the type developed by University of California at Los Angeles, and "Tempilaq," a commercial product manufactured by Tempil Corporation, were used.

2.6.4 Acceleration. Vertical acceleration of the center of gravity of the aircraft was determined from acceleration measurements taken at the left wheel well, fuselage Station 209. The accelerometer could not be located exactly at the CG because it fell inside the fuselage fuel tank. The gages used were Statham C-25-120 linear accelerometers. This instrument had a range of $\pm 25G$ but was set up with the recorders and telemeter for $\pm 15G$ maximum input. Environmental tests proved these instruments to be accurate to within ± 1 percent, but since they were not temperature compensated, they had a slight zero drift. However, the accuracy of the measurement was not compromised, since the ambient temperature was essentially constant during the time the important acceleration data were being taken and instrument sensitivity was independent of temperature. Therefore, the 1-g acceleration indication in the approach could be used as a reference from which the gust acceleration could be measured.

2.6.5 Pitch Rate. Since violent pitching adds considerably to the loading of the horizontal stabilizer, rate gyros were installed near the center of gravity in the plenum chamber to measure this effect. Giannini Model 3611F rate gyros having a range of 0 to ± 300 degrees per second were employed. For the purpose of determining pitch attitude, the rate-of-pitch records were to be integrated.

2.6.6 Elevator Position. Three-position potentiometer installations were made on the elevator, one each at horizontal-stabilizer Station 60, right and left, and one in the middle, at Station 0. These were all three-gang potentiometers, which provided telemeter, recorder, and spare outputs for each of the three positions. By comparing the three-position measurements, any large torsional effects on the elevator could be determined.

2.6.7 Photographic Coverage. Nine airborne cameras were installed in each aircraft to record deflections and other general information not readily obtainable in quantitative measurements. The planned coverage (Figure 2.2) of all airborne cameras is illustrated photographically in Figure 2.9. The canopy installation is shown in Figure 2.10 and 2.11.

All cameras were run at the rate of 64 frames per second, except the unit photographing the cockpit instrument panel. Due to marginal lighting, this camera was operated at a speed of 32 frames per second.

Other information to be obtained by photographic means was the general nature of all buckling of compression skins and gross structural failure.

2.6.8 Recording Equipment. Collection of quantitative data was by means of both airborne and ground-based recorders, which received



CAMERA POSITION No. 1



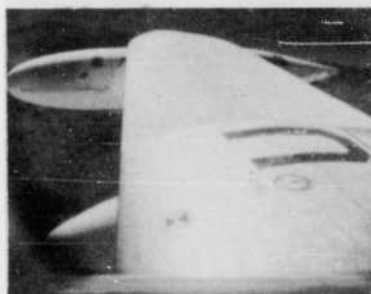
CAMERA POSITION No. 5



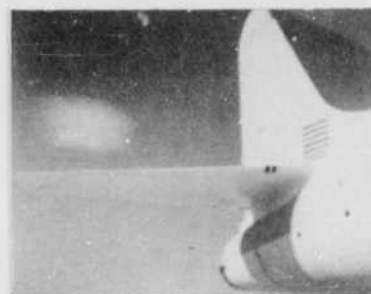
CAMERA POSITION No. 2



CAMERA POSITION No. 6 &



CAMERA POSITION No. 3



CAMERA POSITION No. 7



CAMERA POSITION No. 4



CAMERA POSITION No. 8

Figure 2.9 Airborne Camera Coverage as Photographed During Dry-Run Flight

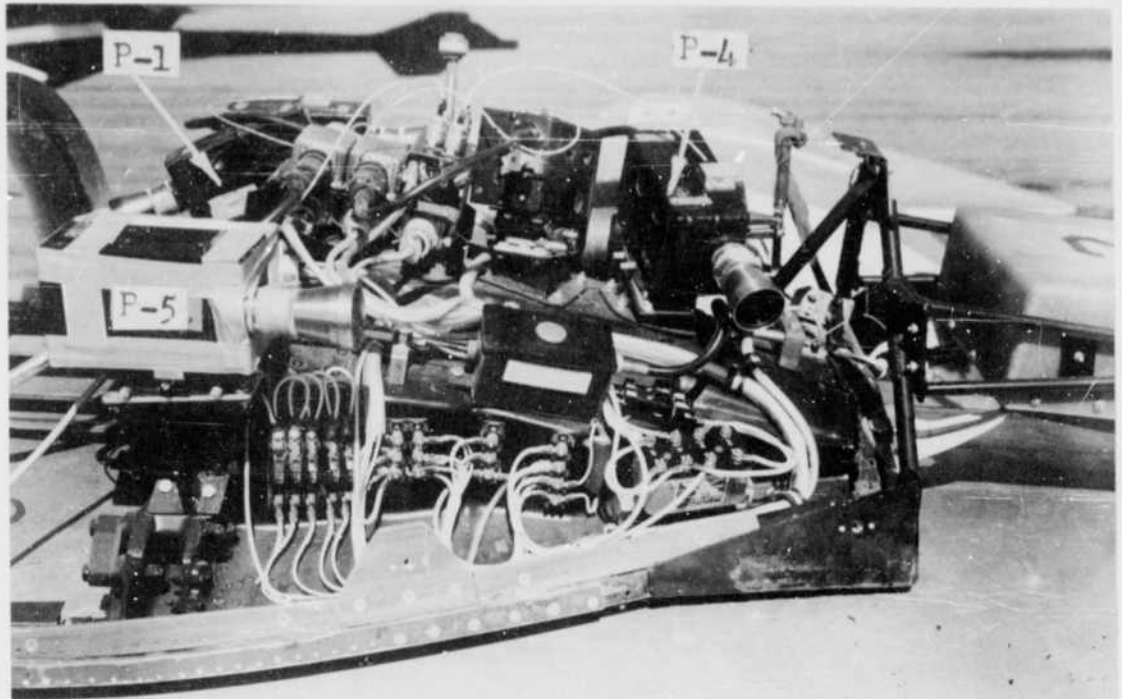


Figure 2.10 Left Side Cockpit Camera Installation

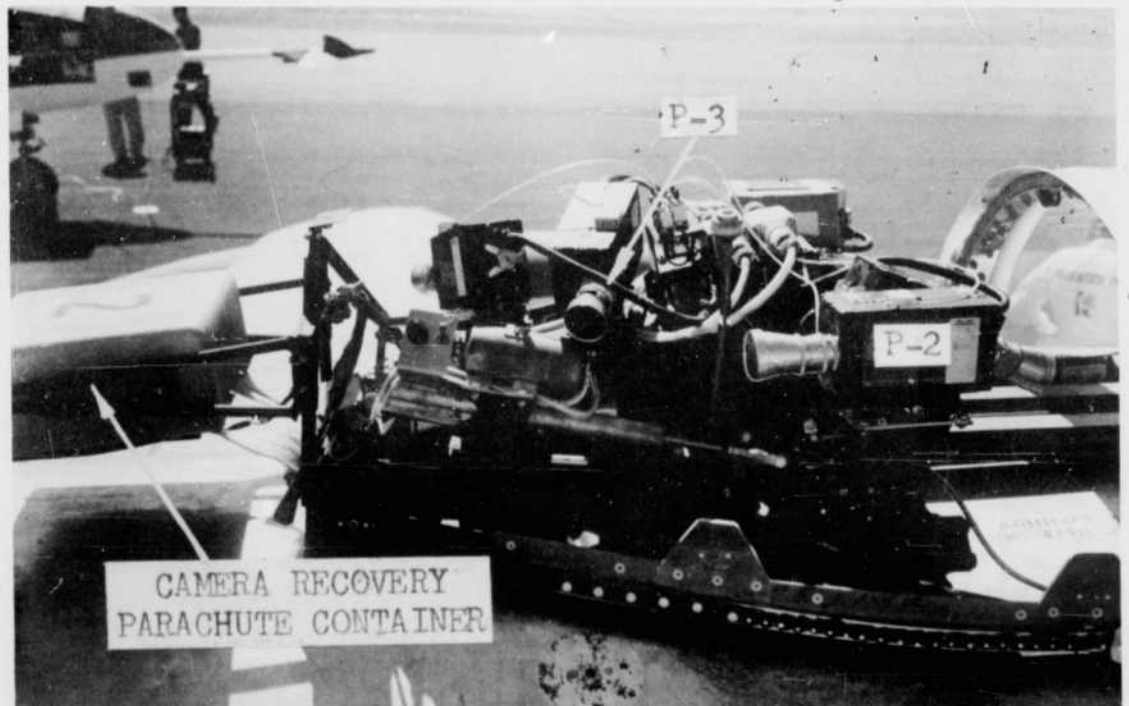
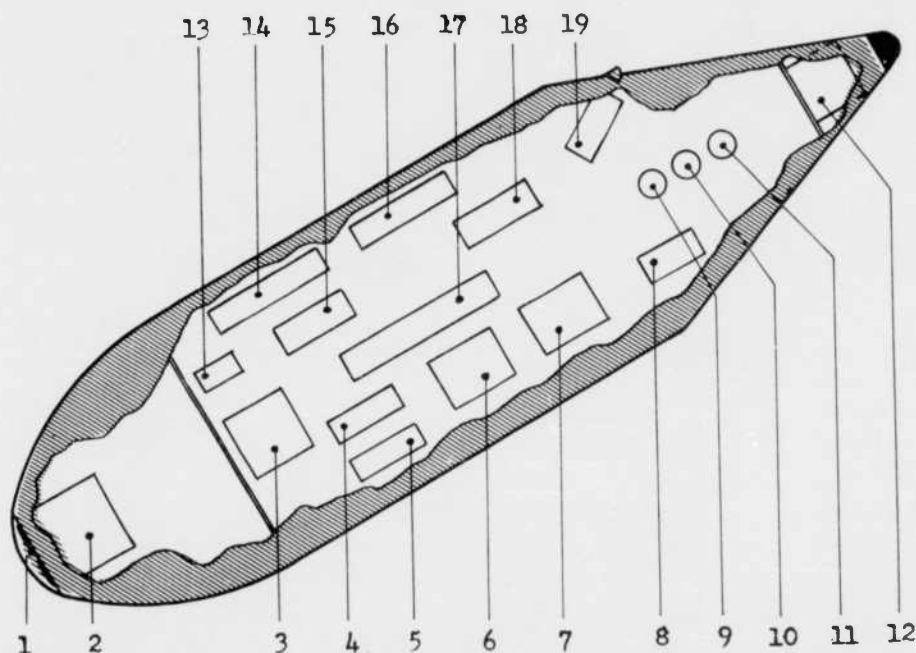
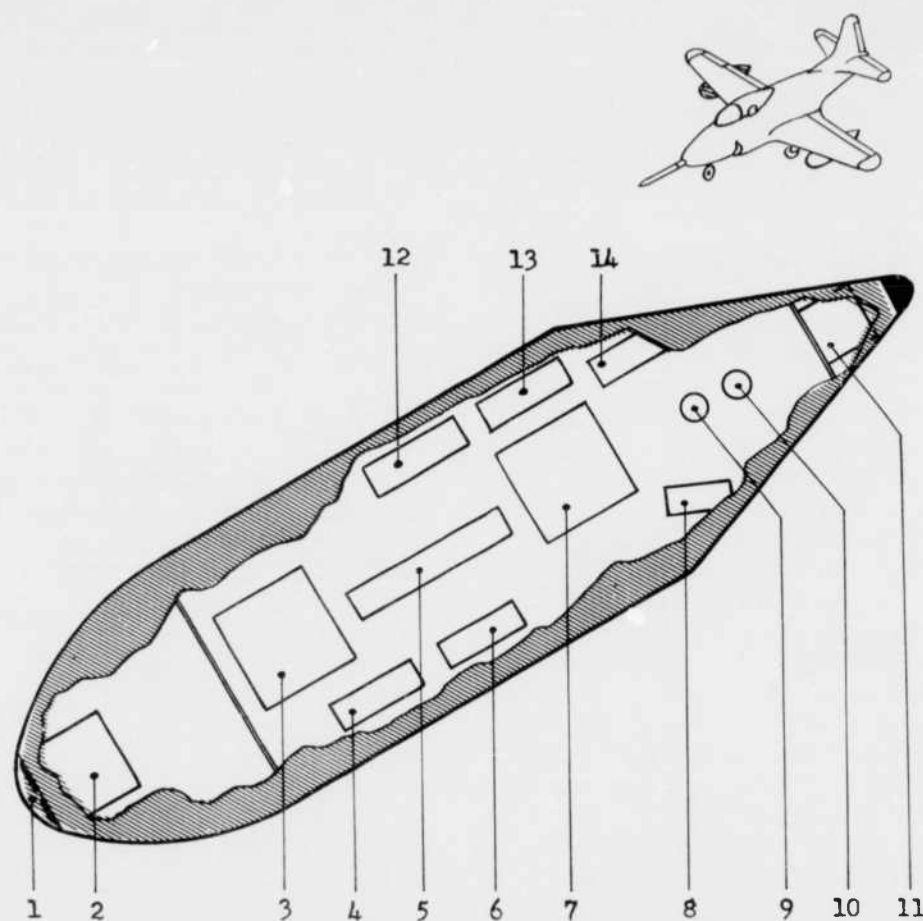


Figure 2.11 Right Side Cockpit Camera Installation



No.	Description	No.	Description
1	Telemeter Pod	10	Calorimeter #1
2	Blower	11	Calorimeter #2
3	Multiplexer	12	Recovery System, Chute, etc.
4	Chopper #1	13	Commutator Balance Box
5	Chopper #2	14	Sampling Switch
6	Transmitter #1	15	Calibration Box
7	Transmitter #2	16	300 V DC Power Supply
8	Incidence Camera	17	Pod Quick-Disconnect
9	Radiometer	18	Junction Box
		19	Tail-Viewing Camera

Figure 2.12 Telemeter Pod Installation



No	Description	No	Description
1	Recorder Pod	8	Incidence Camera
2	Blower	9	Radiometer
3	Attenuator Box #2	10	Calorimeter
4	Bridge Balance Unit #1	11	Recovery System, Chute, etc.
5	Pod Quick-Disconnect	12	Bridge Balance Unit # 2
6	Attenuator Box #1	13	Recorder #1
7	Recorder #2	14	Tail-Viewing Camera

Figure 2.13 Recorder Pod Installation

essentially identical information. Pertinent information concerning both systems is given below.

Telemetry System. The telemetry system employed was the AKT-6/UKR-1 telemeter having 28 channels of 0 to 300 cycles-per-second response. This system employs pulse time modulation of an amplitude modulated carrier and achieves an accuracy better than 1 percent with in-flight calibration. One of the channels was sub-commutated to carry four low-rate inputs. The recorders used with the ground receivers were Consolidated Type 5-119 with 7-319 galvanometers.

In order to give complete radiation pattern coverage with the 2300-megacycle RF link, two transmitters operating on two different frequencies were used to feed antennas located on the top and bottom of the fuselage. Two receivers were diplexed from the antenna which tracked each aircraft. Antenna tracking was accomplished by slaving to the MSQ-1 radar which positioned the aircraft.

All the equipment directly associated with the telemeter was carried in the pod on the left bomb pylon. This pod is shown in Figure 2.12.

Airborne Recorders. Two Consolidated 5-114 recording oscillographs were carried in the right-hand pod. This pod is shown in Figure 2.13. These recorders were equipped with 7-312, 7-315, and 7-318 galvanometers as required for the various transducers.

Laboratory tests were performed to determine the effect of shock on the operation of these recorders and galvanometers. It was found that accelerations of the order of 5 g produced an apparent galvanometer deflection of a few percent of full scale, which was within the manufacturer's specification on the equipment. Recording errors due to acceleration were expected to be as high as 10 percent.

Bridge drive was 5 volts DC obtained from magnetically regulated power supplies. One supply was employed for each recorder and a third was installed as a spare.

Individual bridges were coupled to bridge balance units developed by American Helicopter Company. In addition to providing adjustment of the bridges for zero output under normal conditions, the units were designed to provide calibration signals to the recorders. Preflight calibration was accomplished by switching a known resistance in parallel with one arm of each bridge. The resulting galvanometer deflections were recorded just prior to test.

Chapter 3

CALIBRATION

3.1 CALIBRATION METHOD

In order to permit interchangeability of instruments, galvanometers, etc., all calibration was done in terms of a reference calibrate signal. This calibrate signal was produced by applying an unbalancing resistance to each bridge circuit which corresponded to approximately full-scale gage output. The bridge output thus produced was recorded and all subsequent calibrations were made in terms of this reference.

Final preflight calibration for all recorder channels was made by successively switching calibrate resistors into each channel. The telemeter was equipped with a set of relays which could be made to insert the calibrate signal manually when on the ground or by radio command when airborne. The final telemeter calibration was made at approximately 15 seconds before time zero.

3.2 STRAIN-GAGE CALIBRATION

The general procedure was to introduce into the aircraft structure a bending moment of known magnitude and direction, so that the strain-gage output at the station being calibrated could be positively related to pure bending moment.

From the data obtained in these calibrations, the bending moment was computed and plotted against the total measured strain at the strain-gage station, given as percent of the master calibration signal. From these plotted points the slope of the calibration curve was obtained. For the final calibration curve, it was assumed that the curve was linear and passed through the origin. A sample calibration curve is shown in Figure 3.1.

There were three basic types of installations used, two to measure bending moment and a third to measure structural strains.

3.2.1 Pure Bending Bridges. This type of installation was used to measure wing bending at wing Station 40, fuselage bending at fuselage Station 270, and vertical-stabilizer bending at vertical-stabilizer Station 126. In general these bridges were all calibrated in the same manner. The procedure was to apply a single concentrated load, by means of an aircraft-type hydraulic jack, to the airplane member being calibrated. The wing load was applied at wing Station 228, the fuselage load at fuselage Station 383, and the vertical stabilizer load at Station 170. These loads were measured with a Baldwin-Lima-Hamilton Type U-1 load cell. For the wing and fuselage calibrations, all loads were applied upward, while the vertical stabilizer was calibrated with both right and left side loads.

For the wing calibration, the fuselage was jacked up and placed on cradles so that the main landing gear was clear of the floor and carry-

ing no load (see Figure 3.2). The calibrate load was applied to the wing tip in increments of 500 lb, up to a maximum of about 5,000 lb, and was removed in like increments. Data were recorded after each load increment with equal loads applied simultaneously to each wing. The maximum bending moment attained was approximately a million inch-pounds, or about 29 percent of limit load.

For the fuselage calibrations, the airplane was supported normally on the main landing gear, and the calibrate load was applied to the

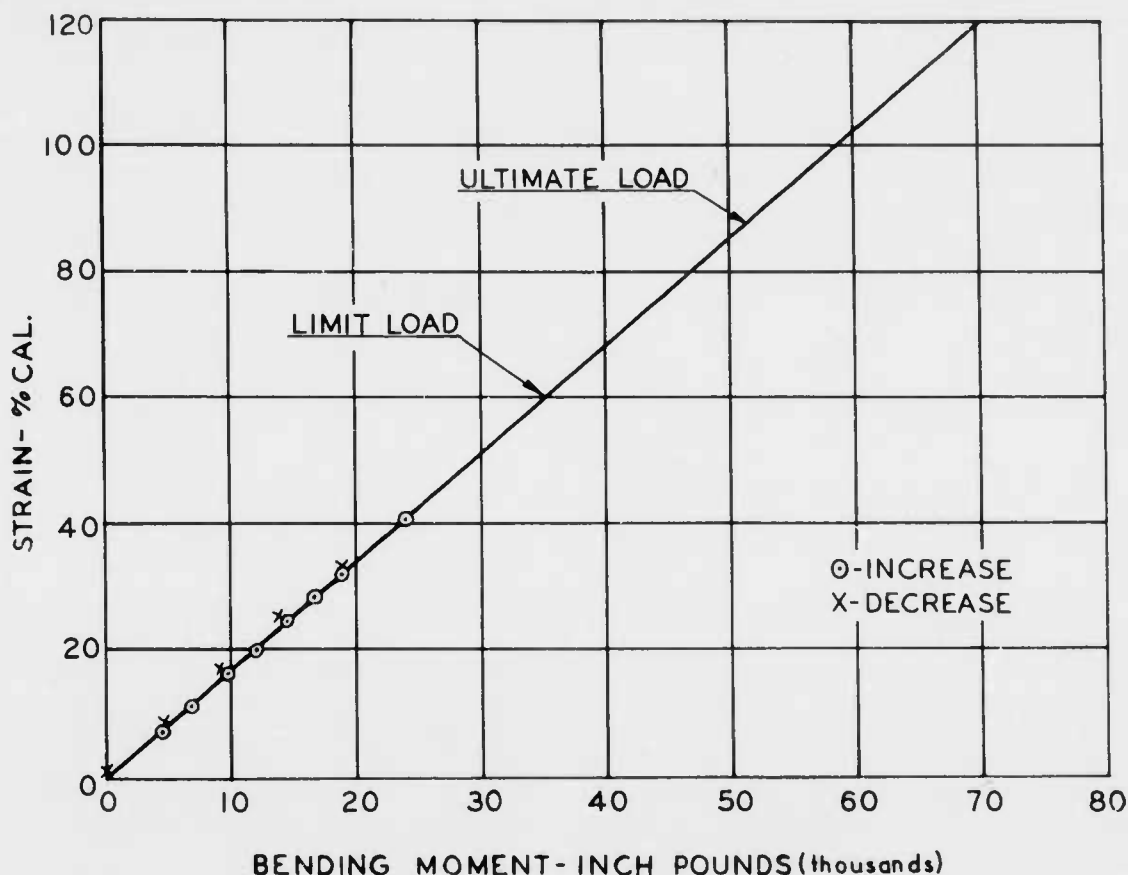


Figure 3.1 Sample Calibration Curve

horizontal stabilizer (see Figure 3.3). A special fixture was required to prevent nose-strut-oleo collapse due to the applied load at the tail. The calibrating load was applied at Station 20 on both sides of the horizontal stabilizers simultaneously. This load was applied in total load increments of 500 lb, up to a maximum of about 4500 lb. This resulted in a maximum applied moment of approximately 550,000 in-lb, or about 40 percent of limit load.

Because of the difficulty involved in applying large side loads to the vertical stabilizer on the airplane, this calibration was performed with the stabilizer installed in a special fixture rigidly attached to the ground (see Figure 3.4). The load was applied in increments of 200 lb,

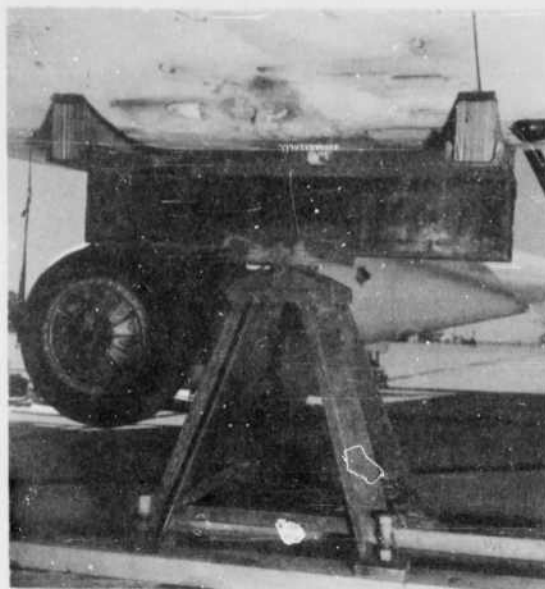


Figure 3.2 Wing Calibration. Left, Fuselage Resting on Cradle Landing Gear Clear of Floor; Right, Applying Load to Wing Tip.

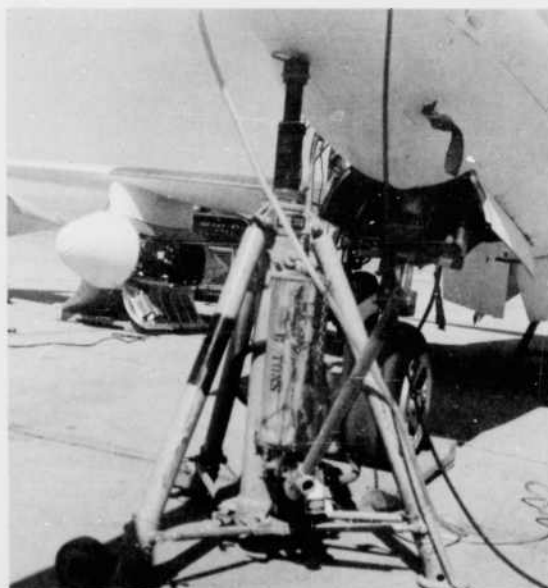


Figure 3.3 Fuselage Calibration. Left, Nose Jacked Up to Prevent Nose Strut Oleo Collapse; Right, Applying Load to Horizontal Stabilizer.

up to a maximum of 1,000 lb, resulting in a maximum bending moment of 44,000 in-lb, or 55 percent of limit load. After the stabilizer had been reinstalled on the airplane, another check calibration was made, using smaller total loads, to make sure that the load-transmission characteristics were the same with the stabilizer mounted rigidly to the ground as with it mounted on the airplane.

3.2.2 Tension-Area-Bending Bridges. This type of strain-gage installation was used on the horizontal stabilizer, and all gages were attached to the lower-surface spars and stringers, which were in the

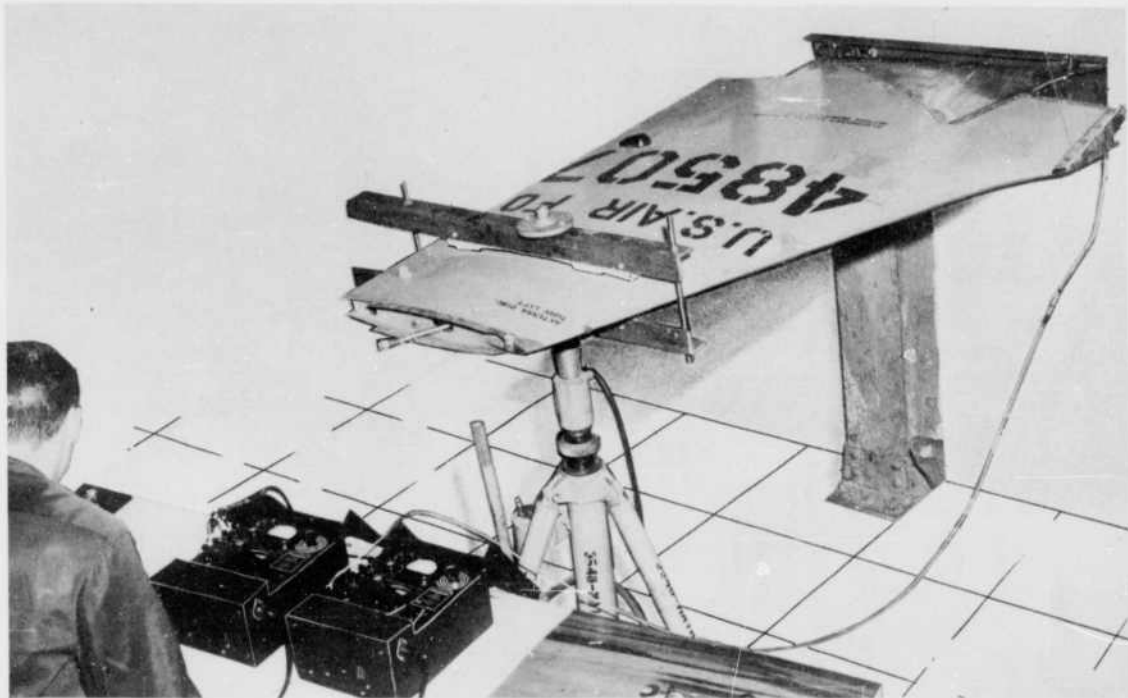


Figure 3.4 Vertical Stabilizer Calibration

tension area. With this type of installation, however, it is not possible to completely eliminate torsion and shear effects from the calibration. Therefore, it was necessary to distribute the applied calibrate load in a manner more closely approximating the distribution of bending moment, shear and torsion expected during the final operation. This was done by means of a whiffletree arrangement, as shown in Figure 3.5, which was the same as that used in the laboratory static tests.

For calibrating with the large loads required on the horizontal stabilizer, it was necessary to remove the stabilizer from the airplane and install it in a special calibration fixture rigidly attached to the ground. The stabilizer is shown mounted for calibration in Figure 3.6. The load was applied in increments of 500 lb, one-half to each semi-span, up to a maximum of 6,000 lb. This resulted in a bending moment about 45 percent of limit. Calibration of one stabilizer was extended to a total load of 10,000 lb, or about 75 percent of limit load, with no

unusual calibration response effects noted. Additional check calibrations were made by applying single-point loads to the stabilizer after it had been installed on the airplane. These checks were intended to verify the validity of a rigidly mounted calibration fixture.

In addition to the calibrations performed at the contractor's plant, information was obtained from a series of destruction tests previously conducted at MIT and WADC. In these tests the stabilizers were identical to those used on the test aircraft and were instrumented in a similar manner. Also, the load-application and load-distribution systems were similar to that used in the calibration performed at the contractor's plant. It was believed that the stresses obtained in the post-buckling range up to and including failure were typical of those expected under similar loads in the final test operation. Therefore, the results of these destruction tests provided a reliable extension of the normal calibration curve through the post-buckling deformation range.

3.2.3 Structural Strain. The structural-strain gages were calibrated at the same time that the bending-moment gages were calibrated. Readings were taken and compiled into tables showing actual element strain in μ in. /in. corresponding to 100 percent calibrate signal.

Calibration procedures and curves for all instrumentation were compiled in Radiation, Inc.'s internal Report #1023-2, entitled "Calibration Report".

3.3 PRESSURE GAGES

Calibration of the Statham P81 pressure gages was checked against the manufacturer's data in the laboratory and was found to be linear and accurate to ± 1 percent, as stated by the manufacturer. Shock-tube tests were conducted to determine the dynamic properties of these gages. It was found that the rise time of the gage was at least as short as that which could be generated at the required pressure level in the shock tube. This was in the order of 250 microseconds rise time. Faster response could not readily be recorded by conventional techniques. No ringing was observed in the gages when shocked.

After installation in the nose boom, all transducers were calibrated by applying a known vacuum to the common reference tube and recording the result.

3.4 ACCELEROMETERS

The accelerometers were calibrated in the laboratory of the manufacturer and were rechecked at several points by Radiation, Inc. Since all points checked satisfactorily in the laboratory, it was felt that periodically rechecking the reading for normal 1-g load was sufficient to verify the calibration.

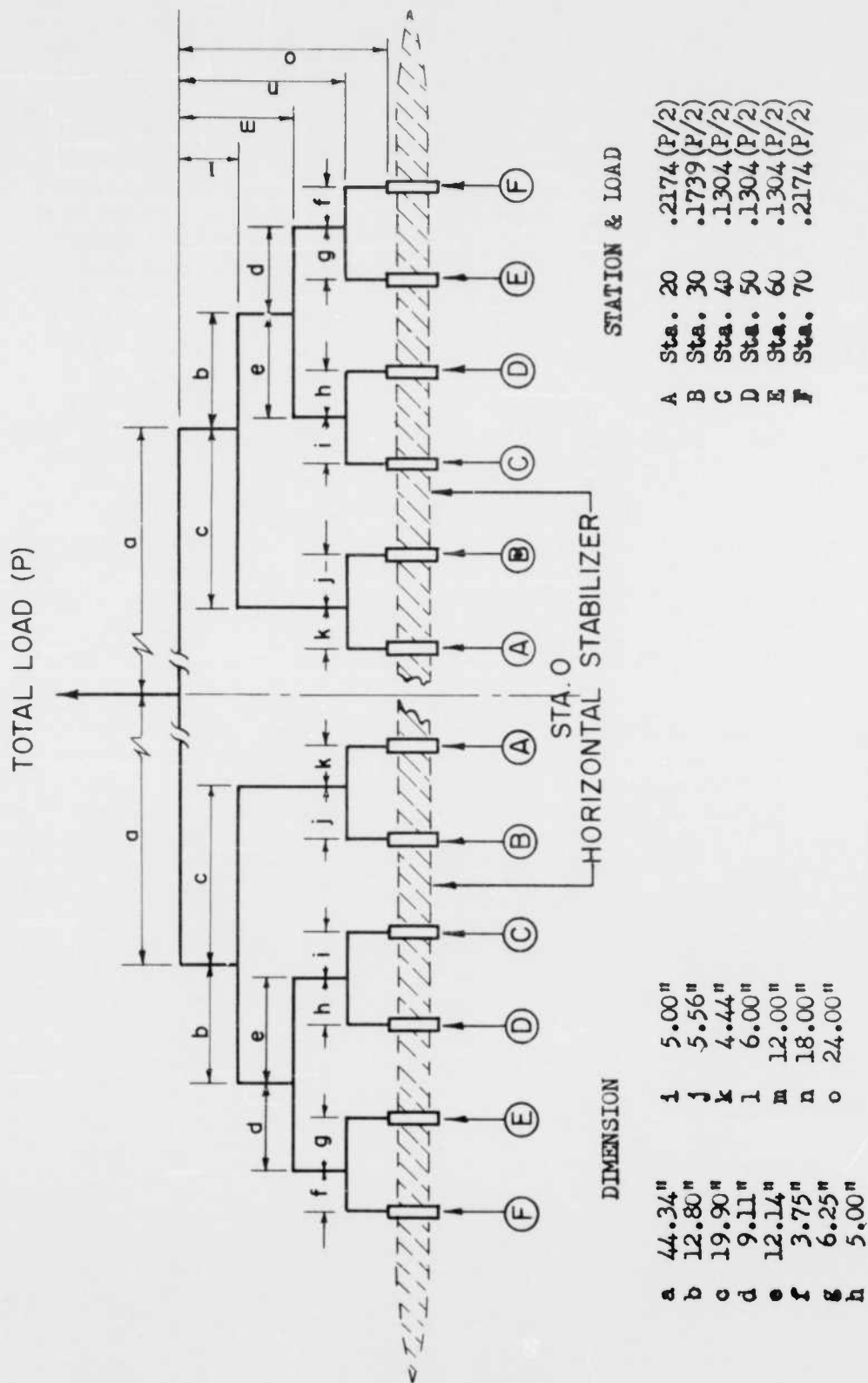


Figure 3.5 Whiffletree Loading Fixture for Horizontal Stabilizer Static Calibration

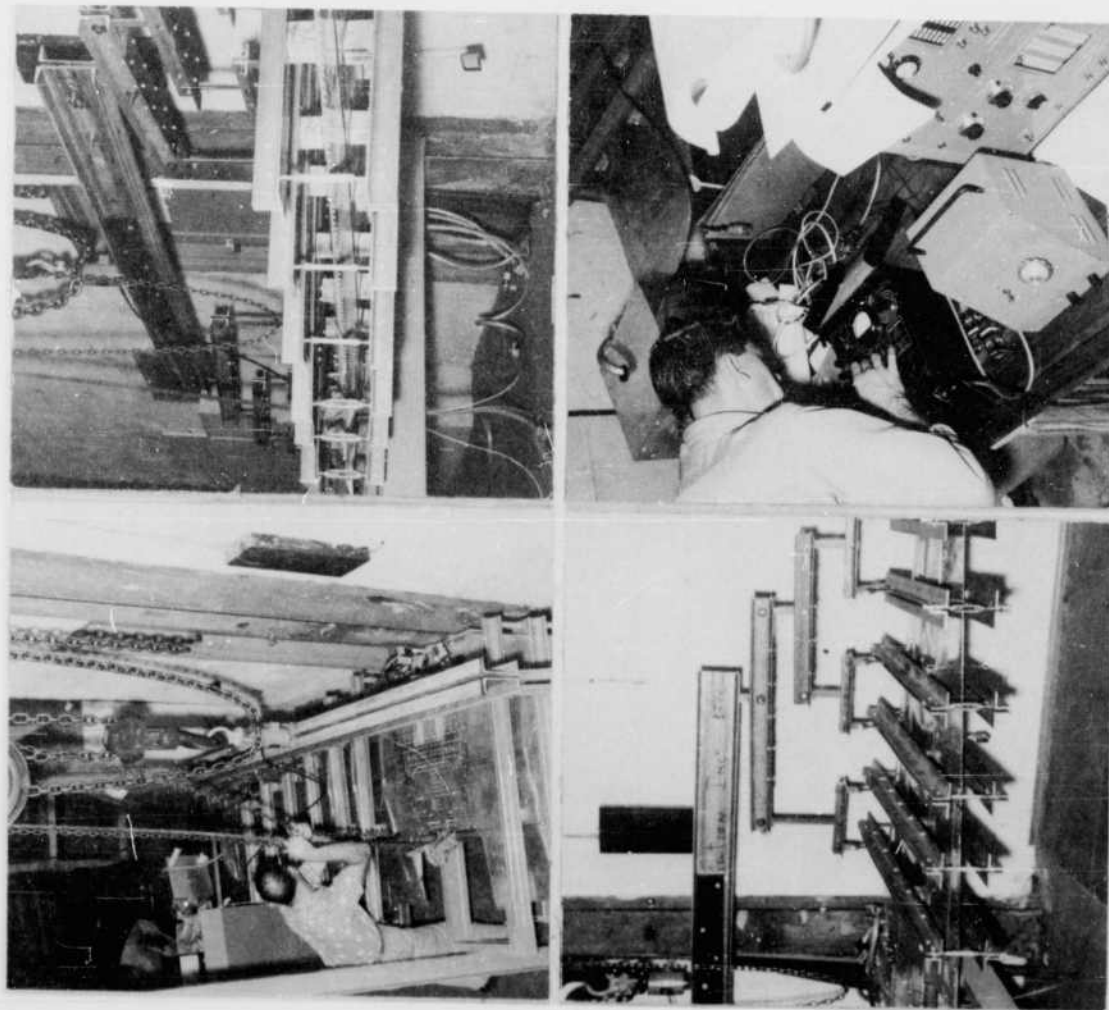


Figure 3.6 Horizontal Stabilizer Calibration. Upper Left, Applying Load; Upper Right, Deflection; Lower Left, Skin Wrinkles; Lower Right, Reading Strain Indicator.

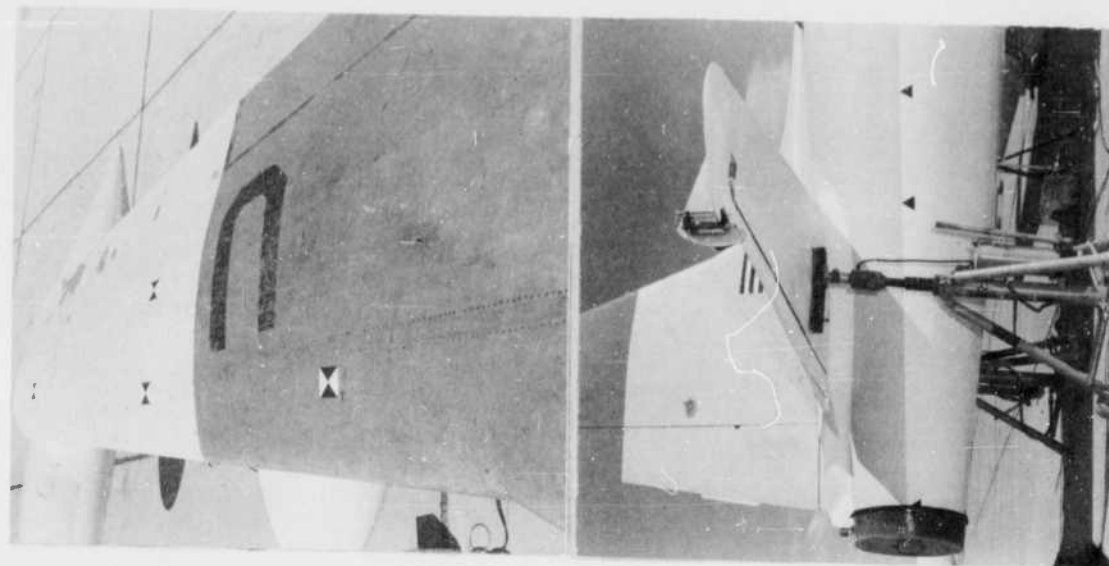


Figure 3.7 Deflection Calibration Points. Top, Wing Calibration Points; Bottom, Fuselage Calibration Points.

3.5 RATE GYROS

Calibration data supplied by the manufacturer were rechecked at WADC. The zero position of the instrument was periodically checked to confirm the calibration.

3.6 RADIOMETERS AND CALORIMETERS

These instruments were calibrated by NRDL. The complete channel of instrumentation for each unit was calibrated by inserting a known voltage into the channel and recording the output.

3.7 AIRBORNE CAMERAS

Calibration of the airborne cameras consisted of determining, previous to the test, the scaling factors at all points where deflection data were necessary. This was accomplished by photographing, from the camera position to be used, an object of known dimensions installed at the deflection calibration points, as shown in Figure 3.7. The scaling factors thus obtained on the motion analyzer were available for use during reduction of the test data on the same motion analyzer. By comparing photographs taken during and previous to the test, the amount of wing, fuselage, and horizontal-stabilizer deflections were determined.

Chapter 4

OPERATIONS

The operational problems encountered by the various personnel participating in this project were considerable, and tremendous effort was required by all concerned in order to successfully complete the mission. This phase of the operation is touched on lightly in this report, however, and only those factors believed to be of significance to the test results are included.

4.1 MODIFICATION AND INSTRUMENTATION

Four QF-80 drone "shells" were delivered to the contractor's plant at Orlando, Florida, in March and May of 1954. These four aircraft are identified according to serial number and position number in Table 4.1.

These aircraft were modified and instrumented for participation in Project 5.1 of Operation TEAPOT. The instrumentation of the first drone was completed at Orlando on 19 October 1954 and the modified canopy and bomb pylon fairings were installed. It was immediately flight tested in Orlando to determine the effects of the modifications. The drone was then ferried to Eglin AFB and delivered to the 3215th Drone Squadron of the 3205th Drone Group who had been given charge of aircraft operation for the test program. On 20 and 21 October 1954 the 3215th Drone Squadron made further flights to determine the flight characteristics of the drones after the dummy pods were added. Considerable aileron buffet was experienced at high speeds with the dummy pods and fairings installed. By redistributing the weights in the pod to more closely duplicate the actual equipment weight distribution and by redesigning the pylon fairing, the buffeting was reduced to a negligible level. There were no adverse effects other than increased cockpit noise level from the modified cockpit canopies. The three remaining drones were delivered to the 3205th Drone Group by 2 December 1954.

4.2 EGLIN AFB OPERATIONS

Shakedown of the drone control equipment and staging and rehearsal of the test mission were accomplished during December 1954 and January 1955. During this time all instrumentation and data source systems were thoroughly checked out. Full dress rehearsals were run on 15 and 22 December 1954 and 7 January 1955. Simulated inputs and check loads were applied to all instruments to verify the previously determined calibration characteristics.

In order to protect the drones from the high-intensity thermal radiation expected at time zero, all lower surfaces were cleaned and painted white. A highly reflective heat-resistant paint (High Altitude White, PV-100) especially developed by the Vita-Var Corp. was used. The paint was ap-

plied at Eglin AFB under the supervision of the WADC Materials Laboratory. Special care was taken to insure that the proper thickness of paint was applied on all surfaces.

4.3 NEVADA TEST SITE OPERATIONS

Upon completion of the staging operations all test aircraft, associated ground equipment, and participating personnel were moved to the Nevada Test Site during the week of 6 through 12 February 1955. The drones were based at Indian Springs AFB, and the maintenance and instrumentation headquarters were established there. The MSQ-1 radar sites, the telemetering trailers, and the radar data recorder trailer were set up at the pre-assigned positions near the Frenchman's Flats Area. At this time

TABLE 4.1 Aircraft Identification

A/C Serial No.	Assigned Drone Position	Also Referred to as:
*QF-80A - 44-85096	1	No. 096
QF-80A - 44-85077	2	No. 077
QF-80A - 45-8301	3	No. 301
*QF-80A - 44-85311	1	No. 311

*Aircraft No. 44-85311 was the spare drone during checkout and dress rehearsals but replaced Drone 1 for test participation.

a communications network was set up linking the above-mentioned areas with each other and with the range control point.

After all equipment was set up and operating satisfactorily, test and checkout operations were continued. Several dress rehearsals and continuous flight testing of drone and instrumentation equipment were accomplished during the remainder of February and all of March 1955. Check loads and simulated inputs were applied to all test aircraft several times during this interval, and results were in close agreement with the original calibration data.

4.3.1 Operational Plan. Accurate positioning of the three drone aircraft was one of the major operational problems. Each drone was assigned two DT-33 director aircraft for drone control during the test participation flight. One director maintained actual control while the second served as a spare. Each drone was flown independently against range time with a basic flight pattern, as shown in Figures 4.1 and 4.2. At the time Point D was reached in Figure 4.1, control of the test drones was transferred to the MSQ-1 ground radar sites, and the two directors took the courses shown to right and left of the drone course. Ground control was maintained until the drones were picked up again by one of the director aircraft after the blast. During the entire flight the director aircraft were in constant communication with the range control point through the Project 5.1 control center. Since the conditions of Shot 12 were tailored to the requirements of Project 5.1, the authority to recommend delay or postponement of the shot was given to the Project Officer. Therefore, the possibility of bringing all three aircraft into the proper time-position relationship was greatly improved.

In addition to the directors previously discussed, each drone was assigned two chase aircraft. These aircraft were used to shoot down

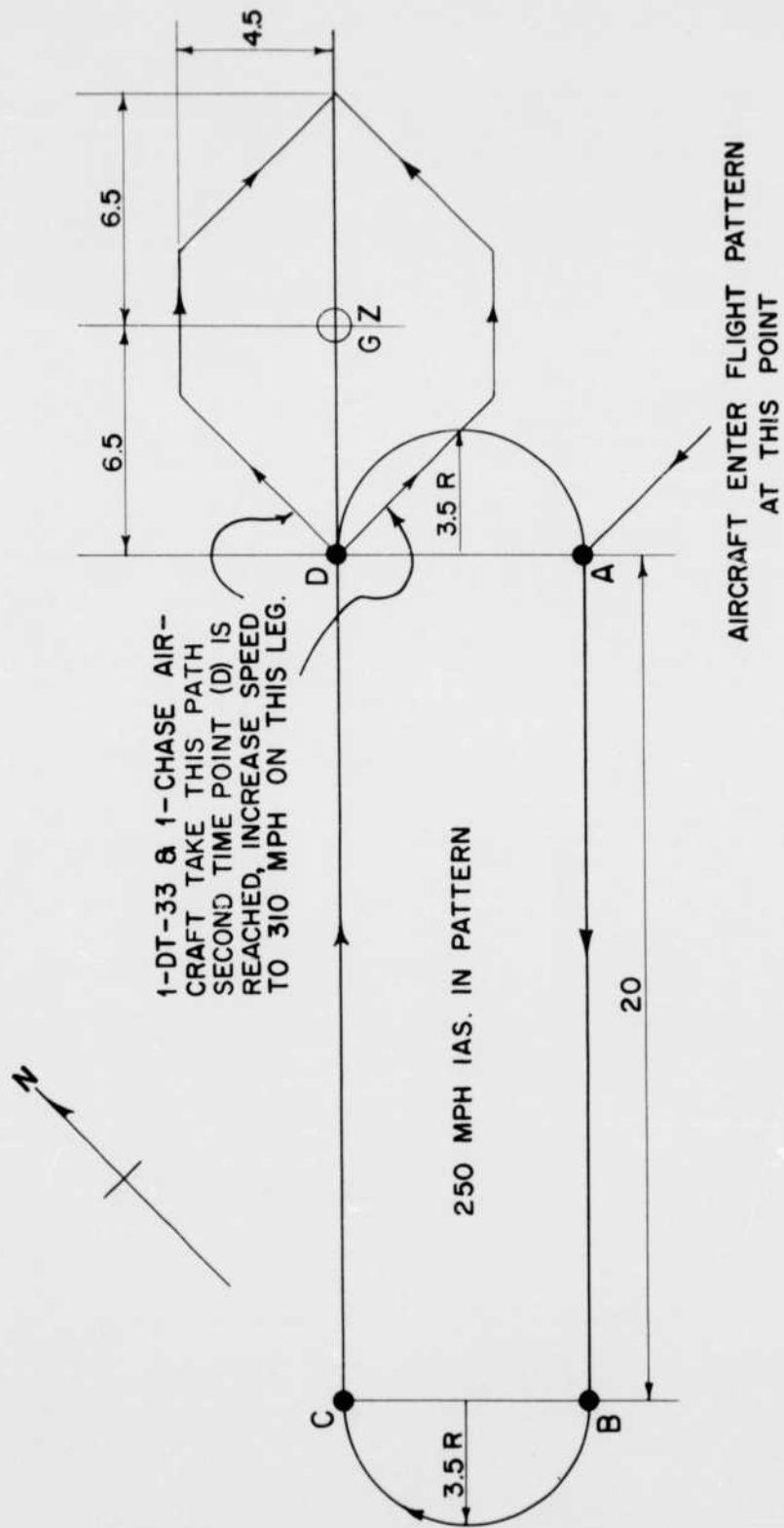


Figure 4.1 Basic Flight Pattern for Drone Aircraft

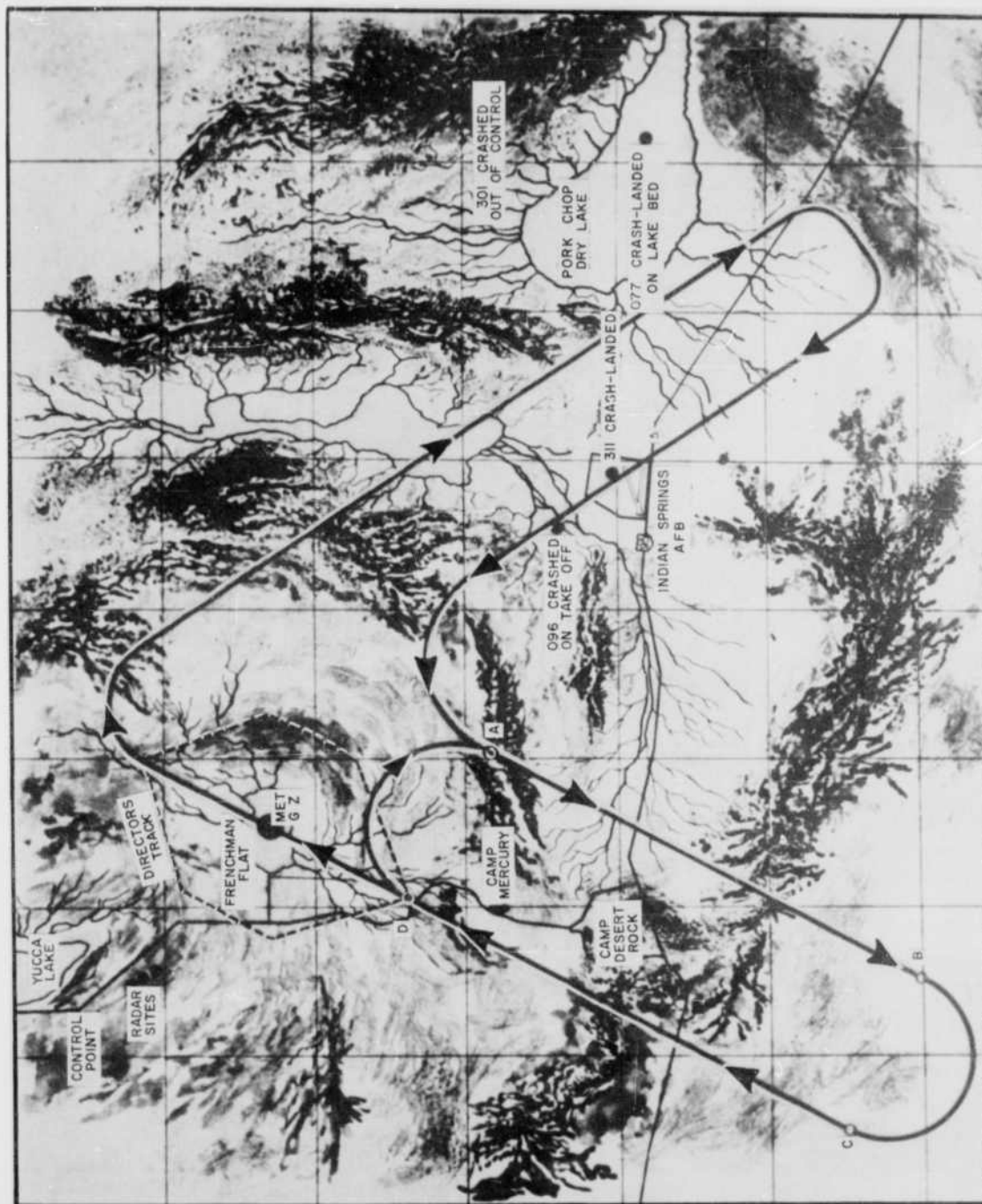


Figure 4.2 Nevada Test Site Area Showing Drone Flight Plan

the drones, if this became necessary, and to provide photographic coverage of the drones in the air after the test. They followed the same flight path at time zero as that of the director aircraft (Figure 4.2).

4.3.2 Shot 6. On 22 March 1955 one manned drone, QF-80A Drone 301, which was assigned the No. 3 position for the event, participated in Shot 6, to determine the effects of a nuclear explosion on propagation of telemetered signals and to serve as a general check on the instrumentation system. The results of the test were satisfactory. All data were received and recorded satisfactorily and agreed closely with predicted results.

4.3.3 Shot 12. The primary test was scheduled for Shot 12, and preparations were made accordingly. In order to assure participation of the required three drones in the test mission, all four drones were completely prepared on D-1 day. At this time a complete inspection and functional checkout of the instrumentation and drone remote-control equipment was made. Cameras and recorder magazines were loaded as a final step of this checkout. Approximately 2 hours before take-off time on D-day, another complete instrument check was begun. Airborne recorders were balanced for 1-g flight loads on the basis of records from previous flights. Just before takeoff, the cockpit canopy and instrumentation pod jettisoning systems were armed.

Since the telemetry ground station was located beyond a mountain range from the takeoff point, no reception of the signals could be made until a few minutes after takeoff. At this time receiver channels were rechecked for balances.

Drone 1 made a successful takeoff but went out of control shortly thereafter and crashed. Drone 2 took off on Schedule 2 minutes after Drone 1 and was followed by Drone 3, also on schedule. By this time the spare drone replacing No. 1 was readied and started the takeoff run. Just before flying speed was attained the director flamed out on the runway. Drone control was transferred to the director for the original Drone 1, which was making a normal pickup approach behind the drone at an altitude of about 50 feet. The drone became airborne successfully, but not before it had veered off the runway, jumped a ditch, and traveled about 300 feet across the desert. The pods probably received severe bumps from protruding brush, rocks, or dirt during the run, since they were necessarily mounted low and the ground clearance was small. After takeoff, all drones were under complete control and entered the flight pattern satisfactorily.

Chapter 5

RESULTS

5.1 GENERAL

Shot 12 of Operation TEAPOT was held on 15 April 1955 at 1115, PST at the Frenchman's Flat area of the Nevada Test Site. The final yield has been established as 22.0 KT which was approximately 20 percent less than scheduled. All results and discussion contained in this report are based on the measured radiochemical yield of 22.0 KT as reported in the letter from Hq., FC, AFSWP, FCWET dated 13 December 1955. A summary of the pertinent data from all shots of interest in this report is given in Table 5.1. Further information about this and other shots in the operation is contained in ITR-1153, Summary Report of the Technical Director, Military Effects Program.

As scheduled, the three drones of Project 5.1 participated in the test and were positioned according to the operational plan. Actual drone positions and velocities at shock arrival are compared with ground zero and with the assigned positions and velocities in Figures 5.1, 5.2, and 5.3 for Drones 1, 2, and 3, respectively. (See also Table 5.2.)

In Table 5.3 are presented the general test results, showing peak values of inputs and responses measured and, where applicable, the degree of accuracy attributed to each. In Table 5.5 are shown the peak values of deflection reached at all measured stations on each drone. In Table 5.6 are presented the maximum values of apparent bending moment induced by thermal effects of the blast. In Figures 5.4 through 5.15 are presented actual time histories of deflections for one right and one left side station on the wing and horizontal stabilizer for each drone. Temperature measurements are present in Table 5.4.

Additional illustrations showing typical time-history curves are presented in the next chapter to facilitate the discussion of results. Complete time histories of all available data are given in WADC Technical Note 55-545, "Data Results for Destructive Loads on Aircraft in Flight."

5.2 DRONE PERFORMANCE AND VISUAL DAMAGE

5.2.1 Drone 1

Performance. Drone 1 remained under complete control throughout the blast and at shock arrival and was maintaining course and altitude when picked up by the director aircraft. The telemeter pod was lost soon after shock arrival, however, and the recorder pod and canopy were jettisoned and later recovered satisfactorily. The vertical fin was slightly damaged when struck by the jettisoned canopy, and the horizontal-stabilizer upper surface was buckled slightly due to blast loads, but no other damage was evident.

All control functions were operating and a normal landing approach was completed satisfactorily. Drone control was then transferred to ground,

TABLE 5.1 Summary Shot Data

Shot	Code Name	Date	Time	Area	Tower Type	Yield (KT)
4	Turk	7 March	0520	T-2	500 ft.	43 \pm 2
6	Bee	22 March	0505	T-7-1a	500 ft.	7.76 \pm .2
12	MET	15 April	1115	FF	400 ft.	22.0 \pm 1.0

TABLE 5.2 TEST CONDITIONS

	Burst Altitude (3477 ft)	Drone 1	Drone 2	Drone 3
Atmospheric Conditions				
Wind (deg/kts)	200/15	220/14	210/16	210/14
Pressure (mb)	879	735	759	778
Temperature (°C)	18.4	3.2	5.6	7.7
Relative Humidity (%)	21	38	35	32
Dew Point (°C)	-4.1	-9.7	-8.5	-7.6
Drone Flight Parameter (Shock Arrival)				
Gross Weight (lbs.)		12,379	13,169	13,038
C. G. % MAC		25.1	27.5	27.8
* Angle of Attack (estimated degrees)		2	2	2
Drone Velocity (ft/sec)				
True Airspeed at Time Zero		436	421	416
True Airspeed at Shock Arrival		436	420	424
Ground Speed at Time Zero		456	447	440
Ground Speed at Shock Arrival		456	445	447
Position (\pm 1%)				
Altitude (MSL) ft.		8859	8015	7331
Slant Range (From Air Zero)		5389	4596	3885

* Not measured

TABLE 5.3 GENERAL TEST RESULTS

Shock	Drone 1	Drone 2	Drone 3
Time of Arrival (sec)	3.26±.01	2.62±.01	2.05±.01
Peak Overpressure (psi)	2.18	3.07	4.19
Normal Acceleration (g at C.G.)	9.3	12.0	15.1
Thermal			
Peak Irradiance (cal/cm ² /sec)	96.5±15%	106.0±15%	172.0±15%
Time to Peak Irradiance (sec)	0.22±0.1	0.21±.01	0.22±.01
* Total Thermal Energy (cal/cm ²)	44.4±15%	51.0±15%	99.0±15%
Peak Horizontal Stabilizer			
# Skin Temperature Rise (°F)	109.0±10%	159.0±10%	362.0±10%
Bending Moment (in. - lb)			
* Horizontal Stabilizer			
Station 52 Left	27,500	—	—
Station 43 Right	30,500	—	—
Station 33 Right	100,400	—	—
Wing Root			
Station 40 Left	196,000	—	—
Station 40 Right	184,000	—	—
Fuselage			
Vertical Stabilizer	Not Recorded	—	—
	Not Recorded	—	—

* This is not maximum value for Drones 2 and 3, since thermal energy was still increasing when the record was lost at shock arrival. See Figures 6.11 and 6.12.

Skin temperatures were measured with resistance thermometers. Skin was 0.040 aluminum having reflectivity of approximately 86%.

* These are the only stations for which measurements were obtained.

TABLE 5.4 TEMP TAPE MEASUREMENTS

Drone	Location	Temp Tape Data	
		Type	Number Temperature
1	Right cover of nose wheel well	UCLA	508 250
1	Outer cover of left wheel in wing	UCLA	510 250
1	Right nose landing gear door	UD	20 200
1	Left dive flap	UD	21 135
1	Right dive flap	UD	22 135
1	Left main ldn. door center	UD	23 155
1	Right main ldn. door center	UD	24 200
1	Left door assembly armament hood	UD	25 200
1	Right pod, left door midway	UD	31 120
1	Right, pod, right door midway	UD	32 120
1	Right pod, bottom aft-tail assembly	UD	35 155
2	Right cover of nose wheel well	UCLA	516 260
2	Instrument pod bottom, left wing	UCLA	518 195
2	Instrument pod bottom, right wing	UCLA	519 200
2	Right inspection door nose assembly	UD	62 120
2	Left pod, left door midway	UD	63 120
2	Left pod, right door midway	UD	64 120
2	Left pod, bottom center	UD	65 185
2	Right pod, left door midway	UD	67 120
2	Right pod, right door midway	UD	68 120
2	Right pod, bottom center	UD	69 185
2	Right pod, bottom aft-tail assembly	UD	71 155
3	Instrument pod bottom, left wing	UCLA	513 250-275
3	Instrument pod bottom, right wing	UCLA	515 250
3	Left pod, left door midway	UD	10 120
3	Left pod, bottom center	UD	1 340
3	Left pod, bottom front	UD	9 250
3	Right pod, left door midway	UD	6 120
3	Right pod, right door midway	UD	4 125
3	Right pod, bottom center	UD	3 255
3	Right pod, bottom, aft-tail assembly	UD	7 250

NOTE: All skins instrumented with temp tapes were 0.064 aluminum and were painted with Vita-Var PV-100 white paint having a reflectivity of approximately 86%.

TABLE 5.5 Peak Deflections
All Deflections in Inches

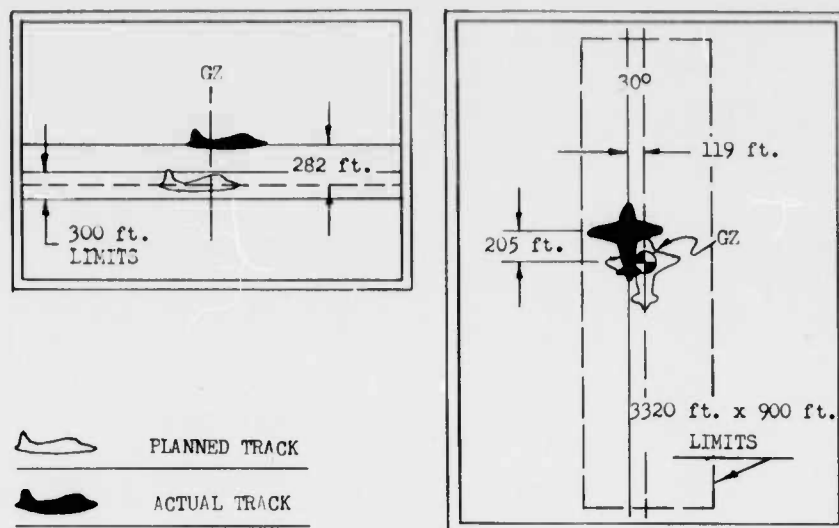
Station Number	Drone 1		Drone 2		Drone 3	
	L.	R.	L.	R.	L.	R.
<u>Horiz. Stabilizer</u>						
Station 94	5.65	7.15	8.20	11.90	15.65	16.90
Station 82	4.55	5.04	6.90	8.90	11.70	11.70
<u>Wing</u>						
Station 213	5.00	5.50	8.30	7.35	9.25	9.80
Station 145 (20%)	2.38	2.55	3.85	2.95	4.55	4.80
Station 145 (50%)	2.25	2.35	4.00	3.10	5.10	4.55
Station 89	1.23	1.22	2.05	1.70	2.70	2.26
<u>Fuselage</u>						
Station 373	2.45		4.40		7.65	

TABLE 5.6 Maximum Stabilizer Apparent Bending
Moment During Thermal Input Period
(Bending Moment, In.-Lb/1000)

Station No.	Drone 1		Drone 2		Drone 3	
	L.	R.	L.	R.	L.	R.
52	44.5	45.5	69.0	76.5	102.0	93.0
43	63.0	64.0	80.0	87.0	112.0	112.0
33	93.0	88.0	104.0	132.0	140.0	138.0

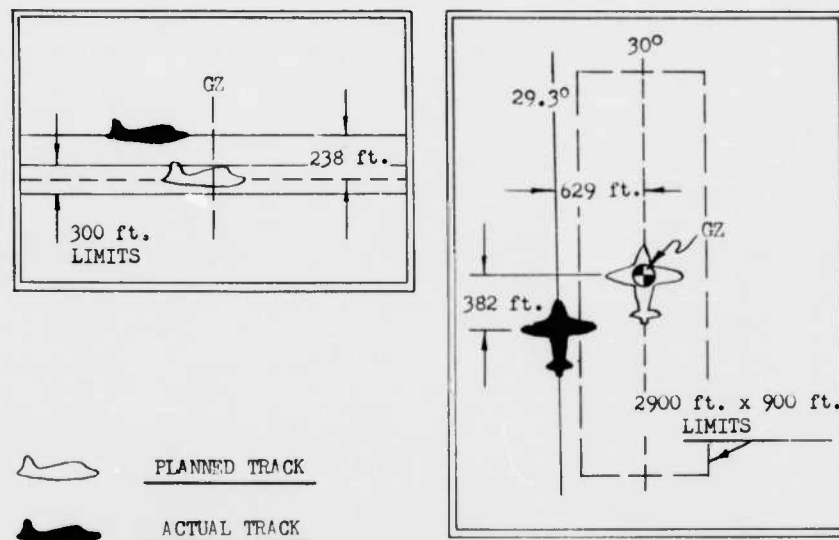
TABLE 5.7 Data Recording Systems

Data Recording System	Applicable Drones	Reduceable Data Range	Remarks
Telemetering	All	T-15 to shock arrival	Some shock peaks readable
Local Recorder No. 1	1	T-15 to T \neq 30	Erratic read-ability at shock arrival
Local Recorder No. 2	1	T-15 to after shock arrival	Some shock peaks readable
Local Recorder No. 1	2	T-15 to shock arrival	
Local Recorder No. 2	2	T-15 to T-10	
Both Local Recorders	3	None	
Camera Position 1	All	Scattered	Sufficient for purpose intended
Camera Positions 2, 3, 4, 5, 7	1, 2	T-5 to T \neq 25	
Camera Positions 2, 3, 4, 5	3	T \neq 0.5 to T \neq 30	Triggered by blue box
Camera Position 6	1, 2	T-5 to T \neq 25	
Camera Positions 6, 9	3	None	Ran at wrong time
Camera Position 7	3	T \neq 0.5 to T \neq 2.3	
Camera Position 8	1	None	
Camera Position 8	2	T-5 to T \neq 2.8	
Camera Position 8	3	T-5 to T \neq 25	
Camera Position 9	1, 2	T-15 to shock arrival	



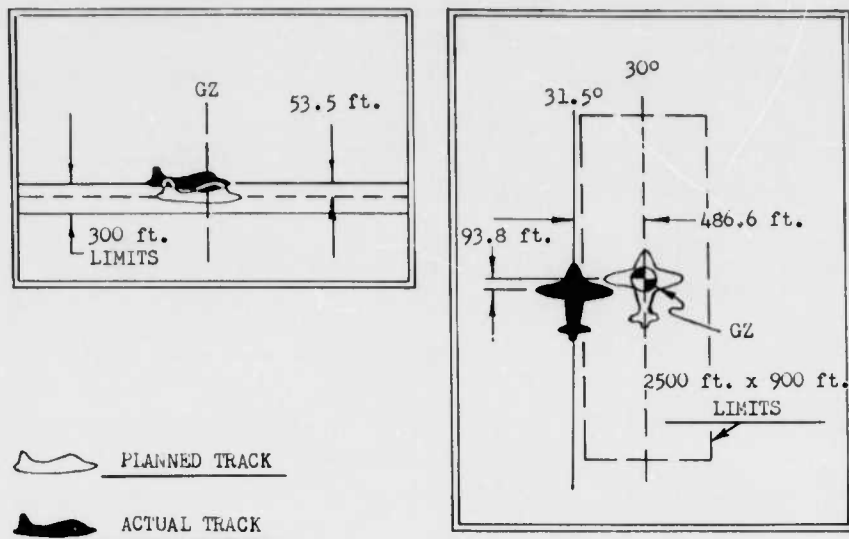
	Planned	Actual
Indicated Airspeed, mph	250	257
True Airspeed, mph	NA	294
Ground Speed, mph	NA	310
Altitude (MSL) ft.	8577	8859
Slant Range (From Air Zero) ft.	5100	5386

Figure 5.1 Actual versus Planned Altitude, Relative Ground Position, and Velocity at Shock Arrival, Drone 1



	Planned	Actual
Indicated Airspeed, mph	250	254
True Airspeed, mph	NA	286
Ground Speed, mph	NA	305
Altitude (MSL) ft.	7777	8015
Slant Range (From Air Zero) ft.	4300	4596

Figure 5.2 Actual versus Planned Altitude, Relative Ground Position, and Velocity at Shock Arrival, Drone 2



	Planned	Actual
Indicated Airspeed, mph	250	258
True Airspeed, mph	NA	289
Ground Speed, mph	NA	300
Altitude (MSL) ft.	7277	7331
Slant Range (From Air Zero) ft.	3800	3885

Figure 5.3 Actual versus Planned Altitude, Relative Ground Position, and Velocity at Shock Arrival, Drone 3

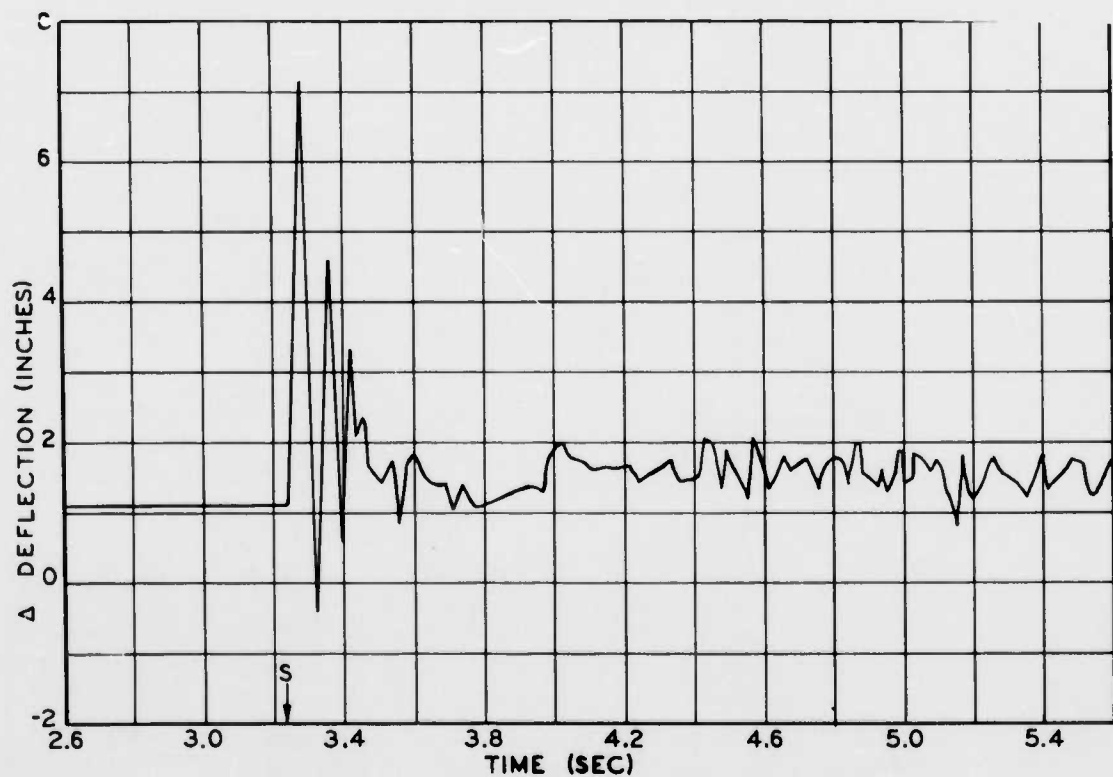


Figure 5.4 Horizontal Stabilizer Deflection, Station 94 Left, Drone 1

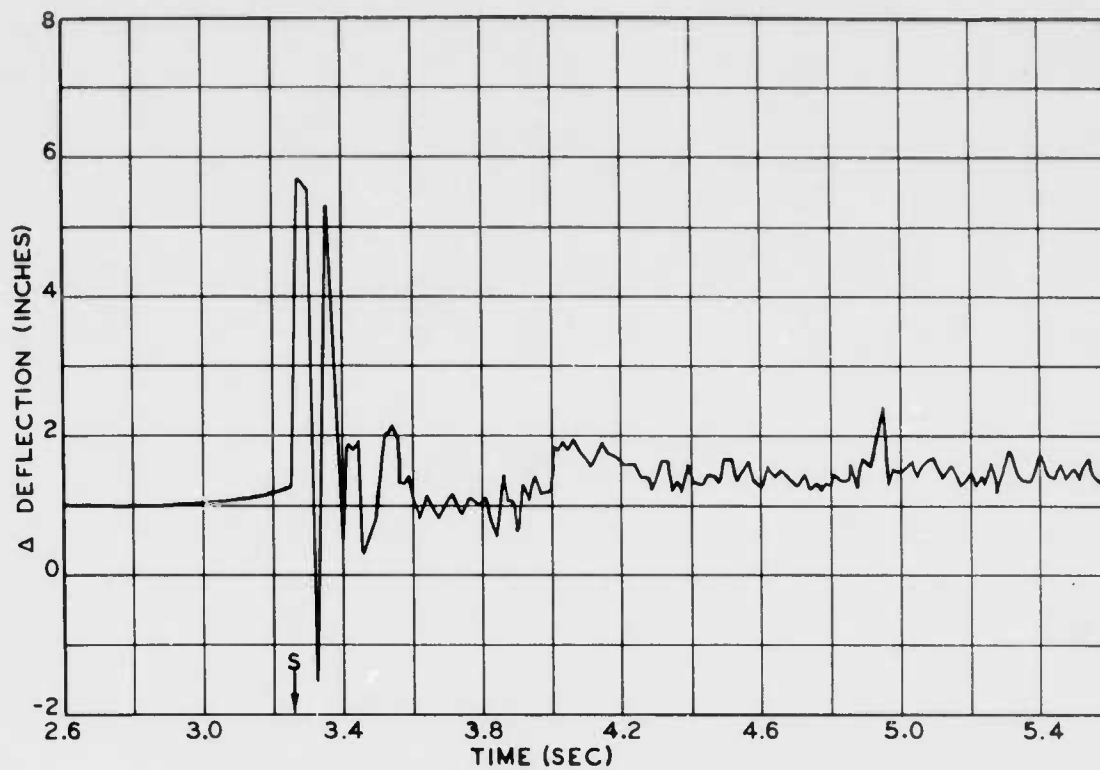


Figure 5.5 Horizontal Stabilizer Deflection, Station 94 Right, Drone 1

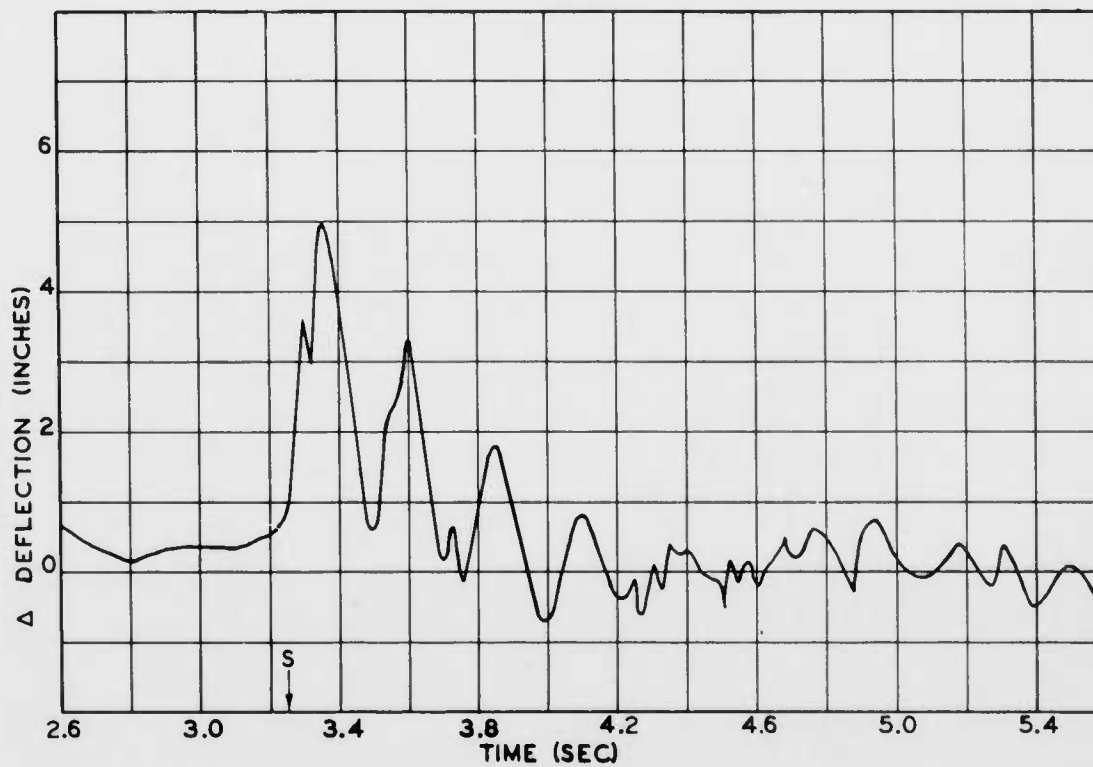


Figure 5.6 Wing Deflection, Station 213 Left, Drone 1

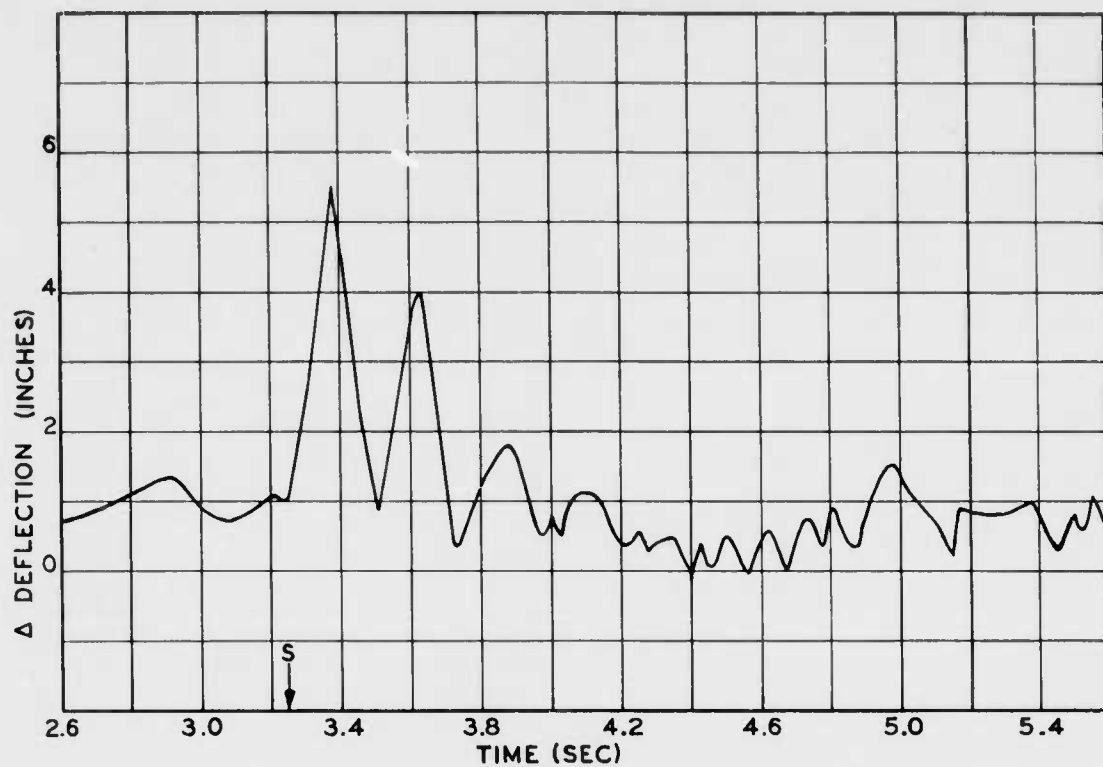


Figure 5.7 Wing Deflection, Station 213 Right, Drone 1

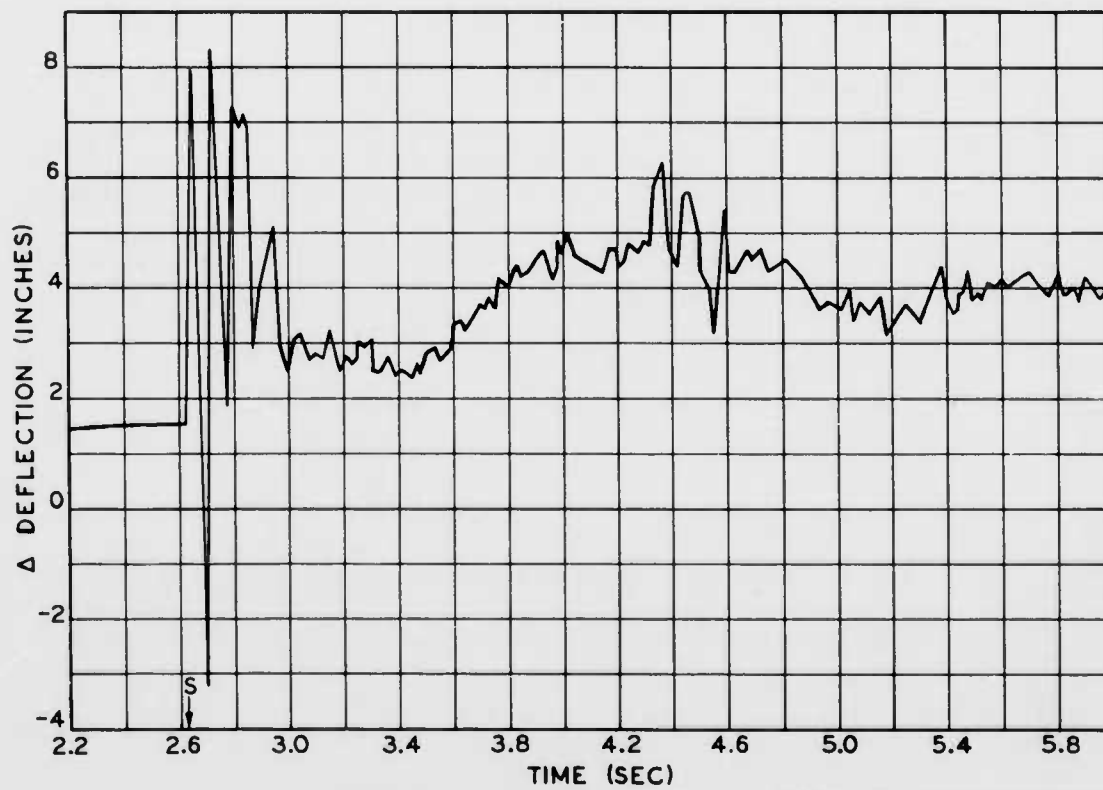


Figure 5.8 Horizontal Stabilizer Deflection, Station 94 Left, Drone 2

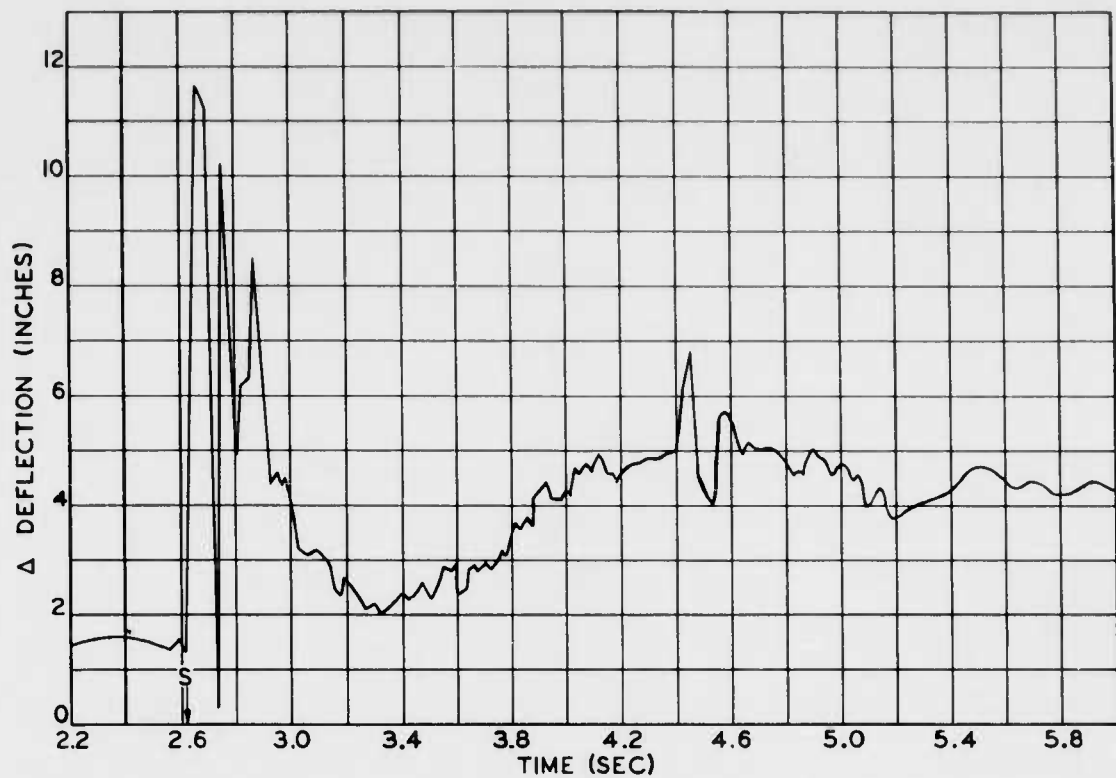


Figure 5.9 Horizontal Stabilizer Deflection, Station 94 Right, Drone 2

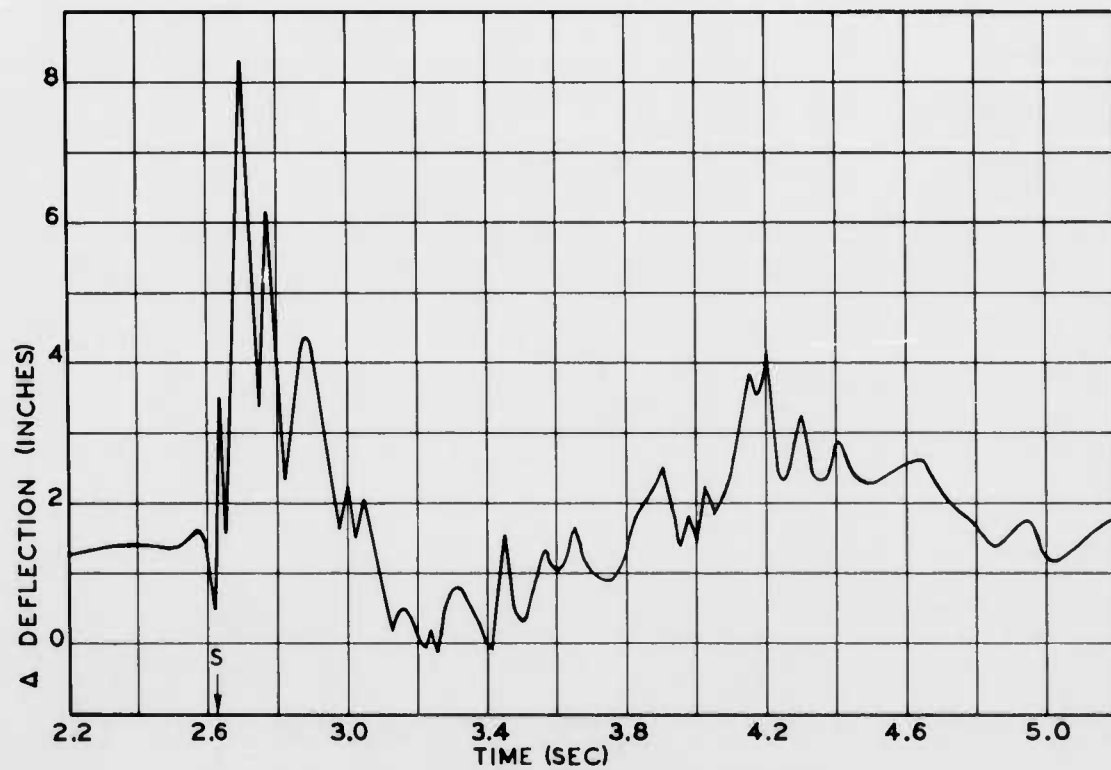


Figure 5.10 Wing Deflection, Station 213 Left, Drone 2

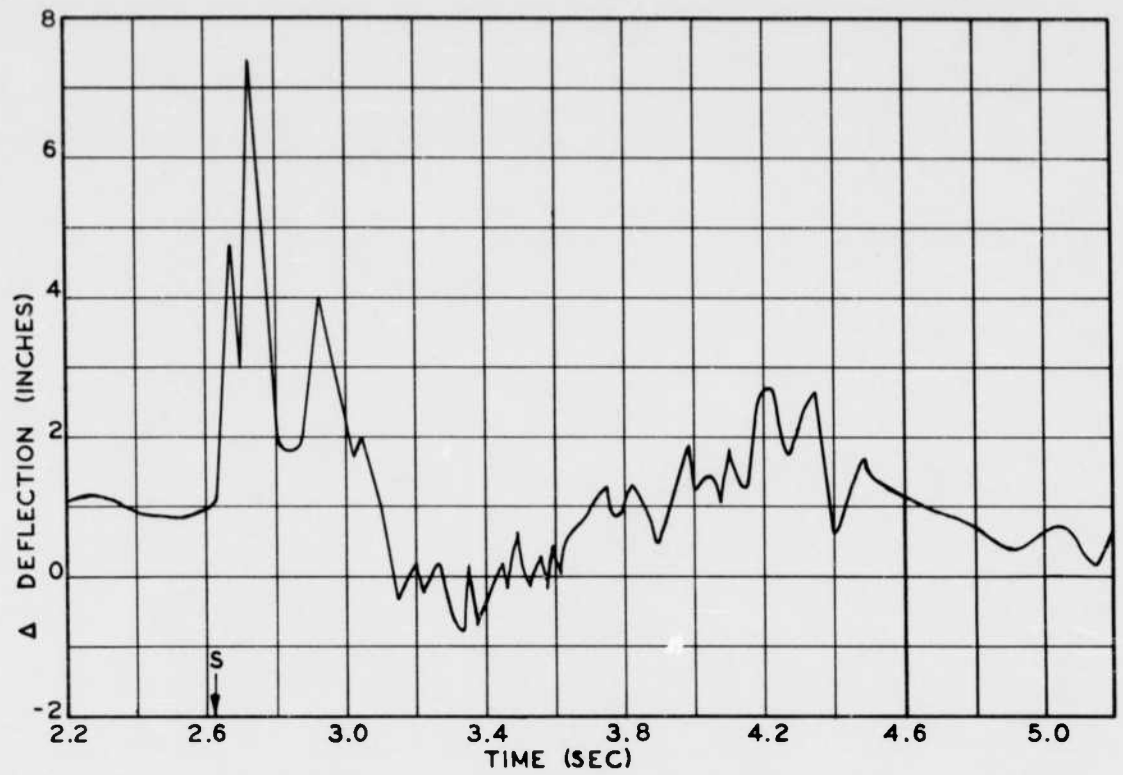


Figure 5.11 Wing Deflection, Station 213 Right, Drone 2

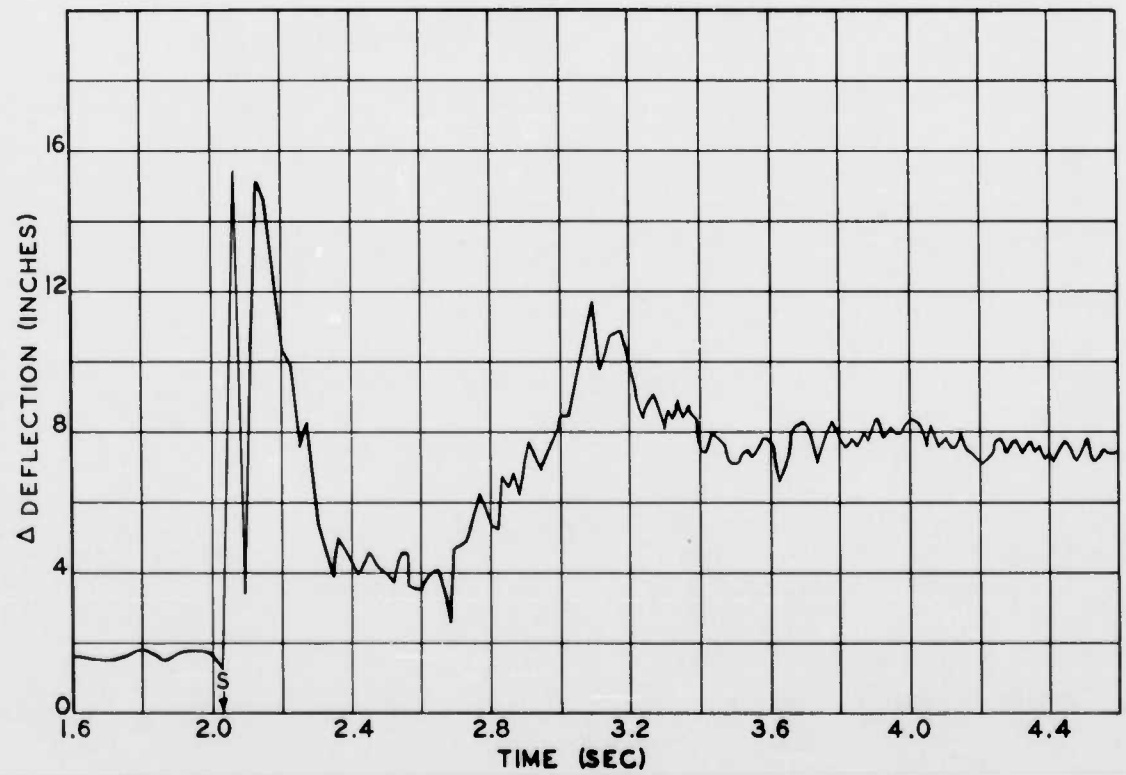


Figure 5.12 Horizontal Stabilizer Deflection, Station 94 Left, Drone 3

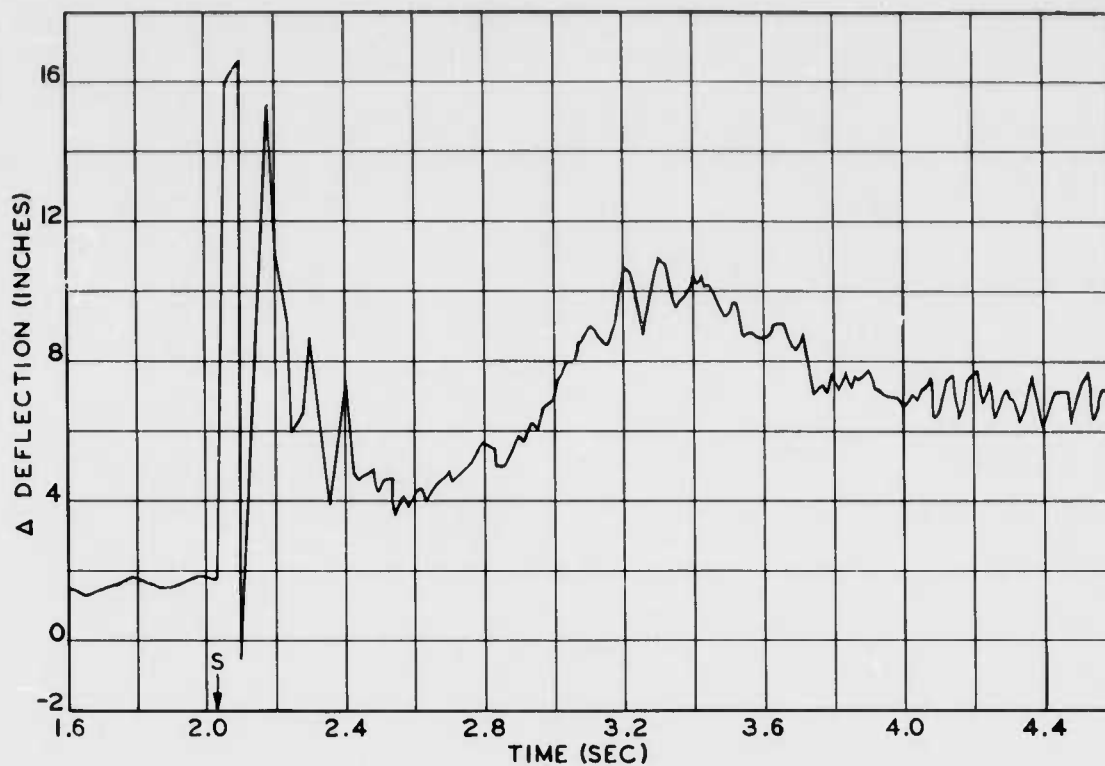


Figure 5.13 Horizontal Stabilizer Deflection, Station 94 Right, Drone 3

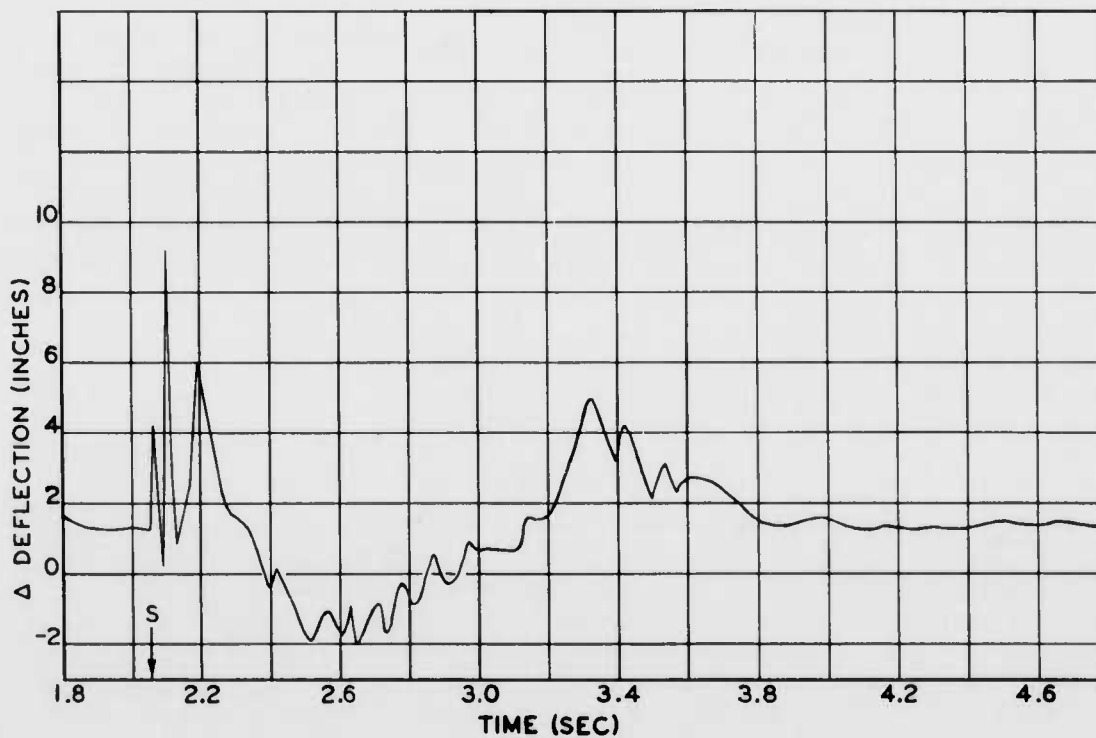


Figure 5.14 Wing Deflection, Station 213 Left, Drone 3

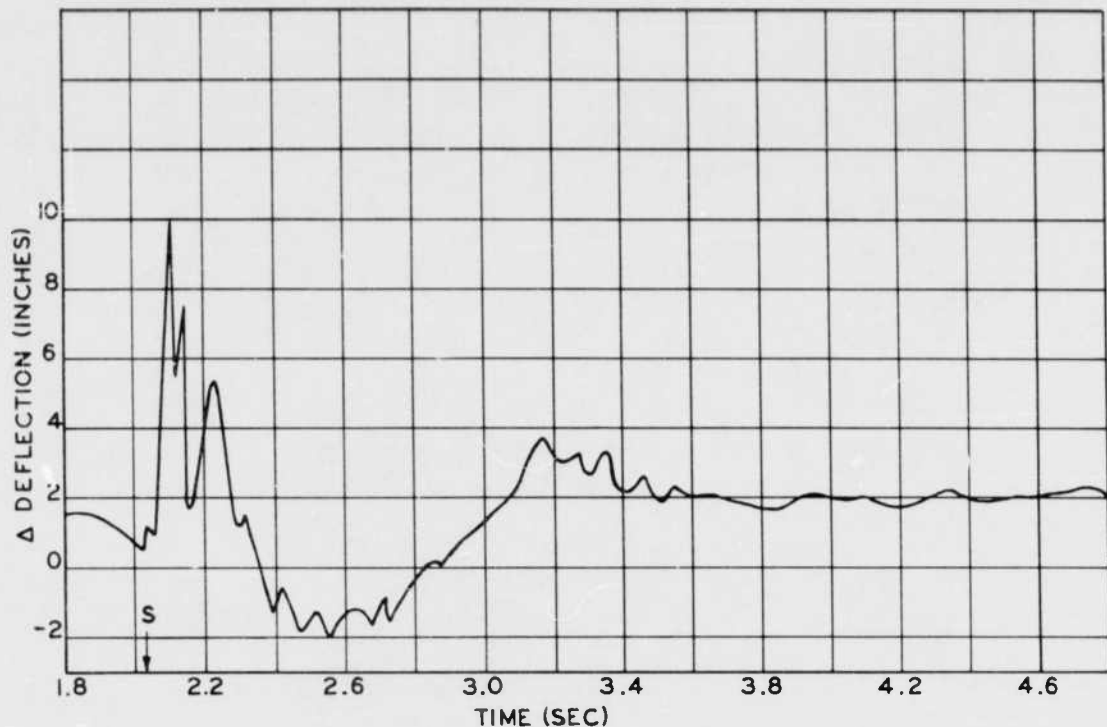


Figure 5.15 Wing Deflection, Station 213 Right, Drone 3

and touch-down was made satisfactorily. After initial touch-down, the drone did not seem to be losing speed rapidly enough, and took several short hops into the air. The nose wheel then collapsed, the right tire blew out, and the drone veered sharply to the right and came to a complete stop just off the runway with the engine still running.

There was no apparent damage to the horizontal stabilizer due to crash landing. The horizontal stabilizer, the Temp-Tapes, and all salvageable equipment were removed from the drone and returned to the interested agencies for further evaluation.

Visual Damage. Close inspection of the recovered drone components in the field and in the laboratory revealed that the blast had very little permanent effect on Drone 1. The horizontal stabilizer was only slightly damaged by blast effects and to an even less degree by thermal effects. There were small permanent buckles, on the upper skin between Stations 40 and 50 on each side, which extended completely across the scab fix. There were also small permanent wrinkles in the elevator, particularly at the trailing edge. The ailerons and flaps had small wrinkles at the trailing edge, but the wing itself showed no indication of damage due to blast. Figure 5.16 shows the blast damage to the horizontal stabilizer and to the aileron. None of these effects would be likely to seriously affect the flight performance of the drone.

The thermal damage consisted only of slight scorching and blistering of dark or blackened areas. These areas consisted of the black deflection-

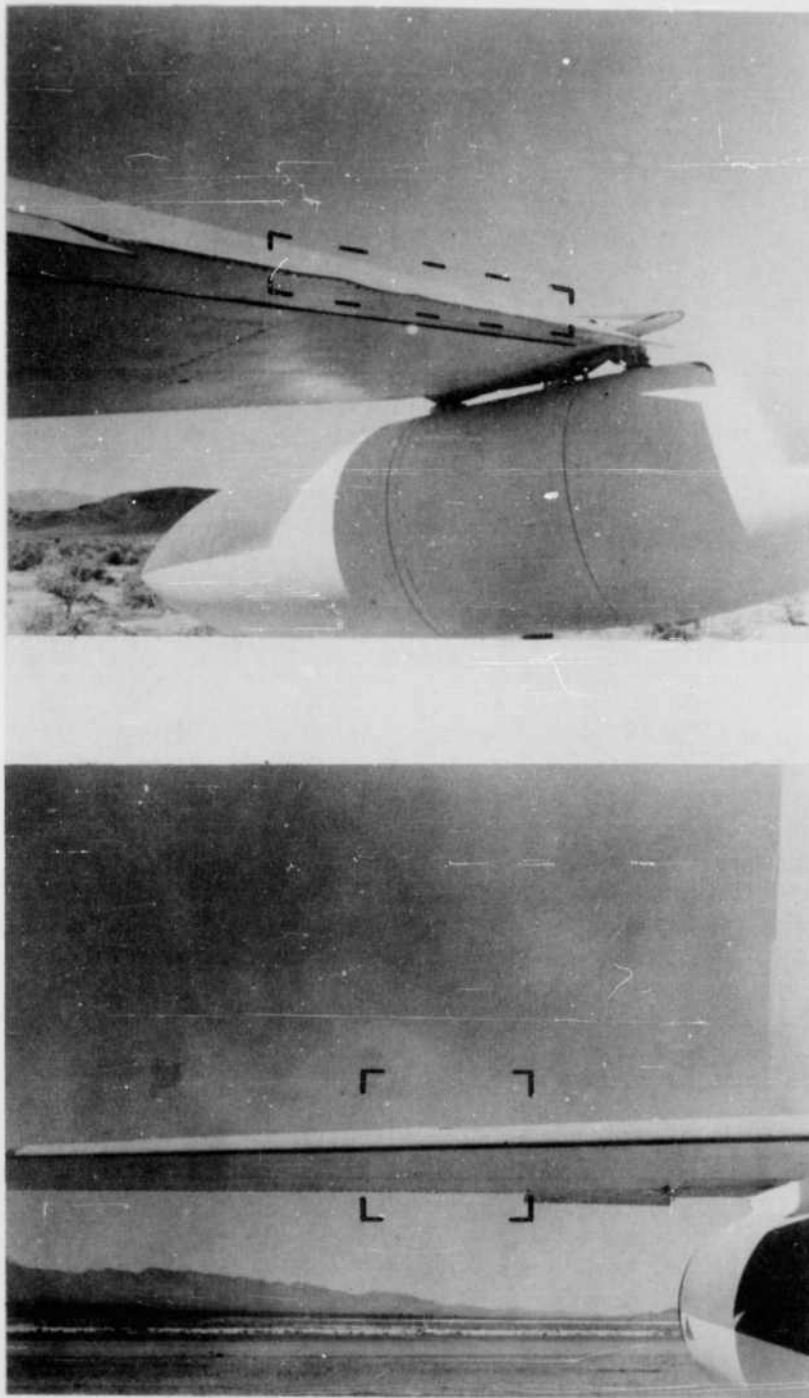


Figure 5.16 Visual Damage, Drone 1

calibration markers and some areas around the elevator leading edge, where a dark protective coating had been applied to the elevator-position pots.

5.2.2 Drone 2

Performance. Drone 2 remained under control, but when intercepted by the director aircraft had lost approximately 150 feet of altitude. At this time it was noted that both wing-tip fuel tanks had been lost, the right aileron was slightly damaged, and the horizontal stabilizer outboard section was bent up.

All control functions were operating, but an unusual amount of "down" elevator signal was required to descend. The drone was taken to the emergency landing field at a nearby dry lake and a landing was attempted. After initial touch-down the drone bounced badly, made a gradual turn to the right, and crash landed. There was considerable crash damage to the drone and the pods were destroyed. Crash damage to the horizontal stabilizer consisted of a large tear at the inboard leading edge of the left semispan. This was caused by the landing gear, which was torn loose during landing, and was obviously not a part of the blast damage.

Although camera and recorder magazines were strewn on the ground, all the magazines were recovered intact. The horizontal stabilizer, the Temp-Tapes, and other salvable equipment were recovered and returned to the interested agencies for further evaluation.

Visual Damage. Close inspection of the recovered drone components in the field and in the laboratory revealed that the damage observed to Drone 2 was similar to that for Drone 1, only more severe (see Figure 5.17). The horizontal stabilizer was buckled between Stations 40 and 50 on both sides, and outboard of that point the stabilizer had a permanent set of about 3 degrees. The stabilizer buckled at about Station 48 at the leading edge, extended back to the vicinity of the main spar, and then moved diagonally inboard to about Station 42 at the trailing edge. There were several rivets popped on the upper skin. The elevators were movable but were binding slightly and showed evidence of rather severe rubbing at the outboard end.

Both the ailerons and flaps were wrinkled near the trailing edge, with the most severe damage at about the midspan of the aileron. Elevator control might possibly have been affected by the damaged elevator, but otherwise the flying capabilities should not have been seriously affected.

As on Drone 1, the thermal damage was confined primarily to the black or darkened patches on the drone lower surface. The blistering was more apparent than on Drone 1, however, and there was some blistering on the white painted surfaces where it was just a little dirty.

5.2.3 Drone 3

Performance. Drone 3 also survived the blast but lost some altitude. When intercepted by the director, both tip tanks were gone, the elevators, stabilizers, and ailerons were damaged, and there was some heat damage

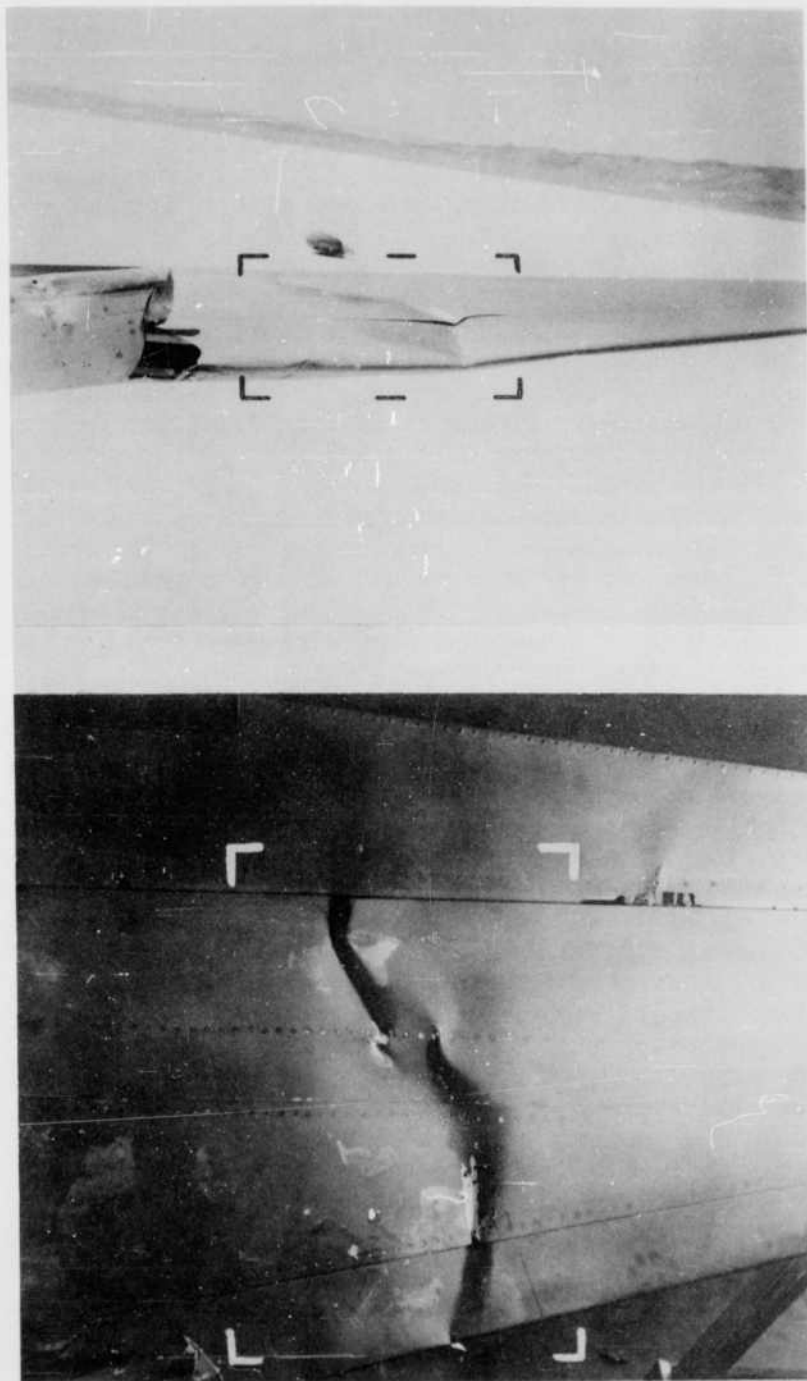


Figure 5.17 Visual Damage, Drone 2

evident on the drone lower surface. The horizontal stabilizer was seriously damaged.

An attempt was made to bring the drone to Pork Chop Dry Lake for an emergency landing. Before a landing could be attempted, however, altitude control difficulties were experienced, and the drone lost control and crashed. The pods and canopy were successfully jettisoned before the crash and later recovered intact.

The aft section of the fuselage, with the horizontal stabilizer attached, was intact but had suffered considerable damage from the crash. The horizontal stabilizer was recovered. The left side sustained little crash damage, but the right side was severely damaged. The stabilizer was returned to the laboratory for further evaluation.

Visual Damage. Close inspection of the recovered drone components in the field and in the laboratory revealed that Drone 3 was severely damaged by blast and thermal effects (see Figure 5.18). The horizontal stabilizer break was more severe than on Drone 2 and the permanent set was greater. The stabilizer broke at about Station 50 at the leading edge extending back to the main spar and then moved diagonally inboard to about Station 42 at the trailing edge. There were several rivets popped, and the skin was ruptured in several places. The elevators were also badly bent, with ruptures in the skin at about Station 42. From an inspection of the recovered stabilizer, it appears probable that the elevator could bind seriously and affect altitude control of the drone. Both ailerons were recovered and were considerably wrinkled and showed signs of thermal damage at the trailing edge.

Thermal damage on the horizontal stabilizer was extensive. Two large areas of paint were burned off from the leading edge to the trailing edge of the stabilizer. The burning started at the black deflection-calibration markers painted on the leading edge of the stabilizers. Although there was some scattered scorching and blistering of the lower surface in general, the thermal damage was primarily confined to areas which did not have clean white paint. Since no severe thermal damage occurred near the failure station, it seems unlikely that these burned areas seriously affected the failure due to gust.

5.3 DATA ACQUISITION

The data-recording systems used in this operation are given in Table 5.7, which also shows the amount of coverage obtained by each. In the following paragraphs is a detailed description of the performance of the various systems.

5.3.1 Local Recording

Drone 1. Both local recorders operated satisfactorily. They were energized at T-15 seconds and ran until all paper was expended, which was about 90 seconds. Excessive gamma radiation caused considerable fogging of the oscillographic paper. This required special developing techniques and resulted in light, though generally readable, galvanometer traces. The rapid deflection of the galvanometers due to instrument responses at

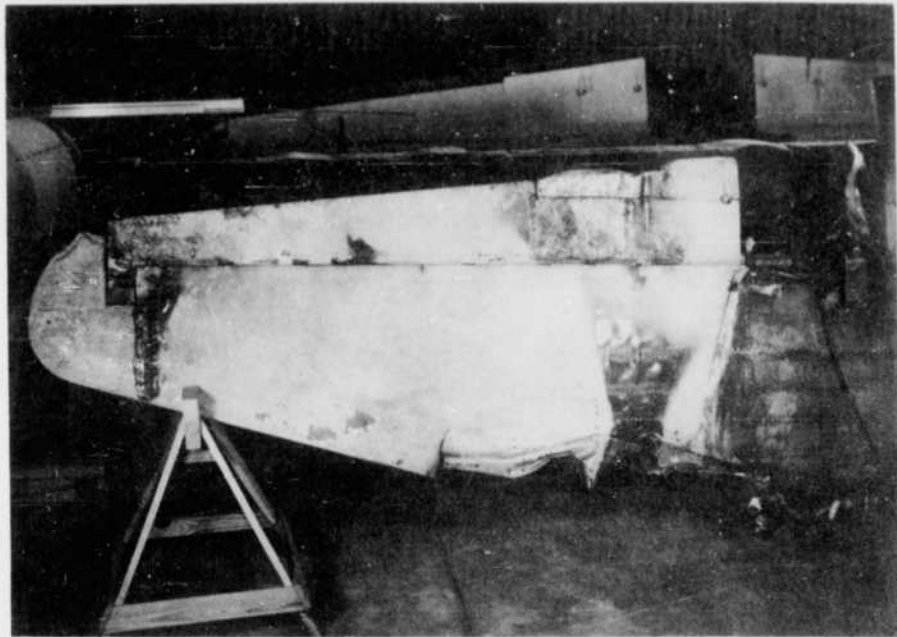


Figure 5.18 Visual Damage, Drone 3

shock arrival caused further weakening of the trace intensity, however, making it extremely difficult to read the record for about 0.2 seconds after shock arrival. On Recorder 2, the transducer drive voltage dropped to zero about 0.10 seconds after shock arrival, after which time no usable information was available on this recorder.

Drone 2. Both recorders operated satisfactorily from T-15 seconds until a power failure occurred at T / 2.9 seconds, or about 0.3 seconds after shock arrival, at which time both recorders stopped. These records were generally readable, although they were fogged even worse than on Drone 1. On Recorder 1, information was available until shock arrival, at which time the traces were so further weakened by rapid galvanometer deflections that the records could not be read. On Recorder 2 the magazine, which was damaged when the drone crash landed, was partially exposed to light. Flight loads were readable for about 4 seconds from T-15 to T-11; but the remainder of the film was exposed during the crash and the record was obliterated.

Drone 3. The recorder paper was all expended, indicating that the recorders operated satisfactorily. However, the paper was so badly fogged by gamma radiation that all information was completely lost.

5.3.2 Telemetering. All telemetered channels for all drones were received successfully soon after drone takeoff and were balanced satisfactorily. All channels were calibrated both at T-40 minutes and at T-20 seconds, and the traces were clear and steady at time zero. At this time there was a momentary disturbance which disrupted the records for 0.1, 0.3, and 0.5 seconds on Drones 1, 2, and 3, respectively. During this time, the records were erratic and partially unintelligible. After this temporary interference, all records were legible until shock arrival.

Drone 1. The telemeter pod was lost immediately after shock arrival, resulting in a complete loss of telemetering information at that time. It is possible that this loss was caused by an attachment linkage weakened by damage, incurred during takeoff.

Drone 2. The carrier signal strength dropped at shock arrival to a level such that the receivers could no longer detect and synchronize on the transmitted signal. There is no evidence of signal level increase throughout the remainder of the record. Although the cause of malfunction cannot be positively determined, it appears that loss of primary power to the telemetering system was responsible for telemeter failure.

Drone 3. Adequate signal strength was received from both top and bottom antennas for 3.5 seconds after shock arrival. However, some peculiarity of transmission prevented receiver video synchronization. The top antenna system failed for unknown cause at shock arrival plus 3.5 seconds. Although adequate signal strength continued from the bottom antenna, synchronization was not regained for several minutes.

It appears, but cannot be proven from available data, that failure of the receivers to synchronize might be due to multipath reception. Support for this hypothesis is given by the Boeing Data Box recordings

of the MSQ-1 pulse returns. On one of these film strips the separation of a single pulse into two, and then three separate pulses can be seen.

5.3.3 Airborne Cameras.

Drone 1. All airborne cameras operated satisfactorily and the film was found to be generally in good condition. The magazine from camera Position 8 photographing the horizontal stabilizer from the telemeter pod was destroyed when the pod was lost from the drone and crashed. Processing of the recovered film under carefully controlled conditions resulted in complete recovery of the required data.

Drone 2. All airborne cameras operated satisfactorily and magazines from the nine camera locations were recovered. Due to a power loss in the recorder pod, cameras at Positions 6 and 7 ceased to run approximately 0.4 seconds after shock arrival. All required data were obtained, however.

Drone 3. Cameras at Positions 6 and 9 were apparently triggered several minutes before blast time, and no information is available from these cameras. All other cameras operated satisfactorily and at the proper time and the recovered film was completely evaluated.

5.3.4 Temp-Tapes. About 50 percent of all Temp-Tapes used on all drones were recovered and sent to their respective developmental agencies for analysis. The temperature measurements from these tapes as read by the developmental agencies were consistent with the thermal results previously presented in this chapter.

5.3.5 Position Data

Phototheodolite. The photographic coverage from three ground-based phototheodolites was complete for all drones. Even though the data were somewhat clouded by dust and sand for the two lower drones, it was entirely satisfactory for determination of all drone positions within the accuracy of the measuring equipment.

Careful study of all position data indicated that the phototheodolite produced the most-dependable data. Comparisons were made of the measured drone positions with other independent input data such as overpressure and shock wave time of arrival, measured input variation, and theoretical calculations. These comparisons indicated that the use of the phototheodolite data resulted in closer correlation between the three drones and input measurements than did the other position data. For these reasons, only the phototheodolite position data are used in Figures 5.1, 5.2, 5.3, and throughout this report.

WLAMC Radar Data Recorder. The data boxes operated satisfactorily during the test for Drones 2 and 3, and all desired data are intact. The data from Drone 1 are complete to T / 2.0 seconds. At this time the radar started hunting in elevation but did not completely lose lock on the drone. Therefore, azimuth and range information are satisfactory throughout the time necessary to establish the drone position at shock arrival. The

WLAMC radar data recorders were generally in quite close agreement with the phototheodolite, and they provided adequate and reliable backup of the measured drone positions.

MSQ-1 Radar Plots. The radar plots were obtained satisfactorily throughout the test for all three drones. However, they are somewhat erratic and do not provide consistent accuracy for all positions. They do provide good backup for the other measurements, however.

Chapter 6

DISCUSSION

6.1 GENERAL

The purpose of this report is to present information regarding the thermal energy and overpressure resulting from a nuclear explosion at specified positions in space and the responses of three drone aircraft exposed to these inputs. The data presented herein are for use by personnel interested in further development of the analytical methods of predicting inputs necessary to destroy aircraft flying in the vicinity of a nuclear explosion. The application of the data to determine the reliability or accuracy of the theoretical methods is beyond the scope of this report. Therefore, the discussion contained herein is limited to a brief analysis of visual damage, an explanation of the recorded data presented, and information defining the reliability of the data.

This type of program has many inherent problems due to the extreme stringency of the operational plan. All three drones operated much closer to the blast than during previous operations. This naturally resulted in more-severe effects due to shock, nuclear radiation, and thermal inputs. Since the drones were unmanned, remote-control operation was necessary with the final checkout coming at least an hour prior to the actual test. In spite of these disadvantages, the greater part of the required data was obtained. In addition to the previously discussed difficulties experienced with the data-recording systems, there was the normal amount of isolated instrument failures. However, sufficient back-up was provided in the instrumentation design to compensate for this.

It is thought that the continuity of the data is improved by comparison of one drone with another in order to see the effect of slant range on the measured inputs and responses. For this reason the drones are considered as a group and are not discussed separately. Instead, each measured characteristic is discussed in the same section for all drones.

6.1.1 Position. Figures 5.1, 5.2, and 5.3 show that at shock arrival Drones 1 and 2 were both outside the specified tolerances in altitude and Drones 2 and 3 were both outside the specified tolerances laterally. Combining all position errors for each drone, it was determined that the slant range to the actual measured position was greater than to the scheduled position for all drones.

Even though Drones 2 and 3 were outside the preassigned lateral limits, there is no evidence in the data of significant asymmetric loading. It is therefore indicated that the lateral position errors reported herein would not appreciably alter the inputs and resulting damage, and the data can be directly compared with predicted results.

6.1.2 Damage. In general, the drone damage was not as severe as was anticipated. Even though the horizontal stabilizer on Drone 3 was

broken, and on Drone 2 was considerably damaged, the damage did not appear sufficient to be classed as destructive as applied to manned aircraft flight. Therefore, none of the drones were destroyed, and it is possible that all could have been flown to a successful mission, if not to a safe landing.

This test did confirm the basic prediction that the blast effects were more severe than the thermal effects and that blast was the critical factor. The horizontal stabilizer was proven to be the critical structure, since that was the only component which received significant damage. However, failure did not occur at the predicted station on the horizontal stabilizer. Failure actually occurred at Station 40-50, which was the secondary break station and was thought to be less critical than Station 10-20, which was undamaged.

The fact that the damage to the drones was less than anticipated can be attributed largely to the decreased gust velocities associated with the lower overpressure, for which there are several contributing factors. The bomb yield was lower than scheduled by about 20 percent, which would normally be expected to result in a decrease of overpressure of about 12 percent. The increase in slant range for Drones 1 and 2 would normally be expected to result in a decrease of overpressure of about 10 percent. The increase in slant range for Drone 3 would be expected to result in a decrease in overpressure of less than 5 percent. It is therefore indicated that the total decrease in overpressure caused by these two factors would be about 20 percent for Drones 1 and 2 and about 15 percent for Drone 3. These figures agree reasonably well with actual measured values.

The fact that the stabilizer did not break in the predicted manner indicates that there is considerable difference between response of the structure to a dynamic gust load of this type and to a static load as applied in the laboratory. This also is possibly a contributing factor to the drones not being damaged as much as predicted.

It is evident that, in order to effect complete, immediate destruction of the aircraft in flight, considerably greater damage must be sustained. Consideration might even be given to an entirely different approach to aircraft destruction. In this test an attempt was made to destroy the aircraft by a bending moment failure of the stabilizer. Though the inputs obtained in Project 5.1 were less than planned, the primary structural members were broken and the stabilizer had considerable permanent set. However, the surfaces were still intact and were sufficient to provide stabilizing loads enabling the aircraft to continue straight-and-level flight. Tests made at MIT with the recovered stabilizers revealed that even the most-severely damaged stabilizer was capable of carrying considerable load. It appears that it might be necessary to actually remove the lifting or control surfaces in order to guarantee immediate destruction of the aircraft.

6.1.3 Post-Operation Tests. Upon recovery, all stabilizers were sent to the Structures and Aeroelastics Lab at MIT for static tests and further analysis. The preliminary results of these tests are given in Table 6.1. The stabilizers were mounted in the static test fixture and the deflections at various stations were measured with no load applied. These deflections are shown as Initial Permanent Set in Table 6.1 and re-

sult from the loading encountered during the test operation. An up load was then applied outboard of the failure station (40 to 50) until the failure station could sustain no further increase in load. The resulting load and moments are shown in the second and third columns of Table 6.1. After the load was released, the deflections were again measured and recorded in the last column of Table 6.1 as Final Permanent Set.

6.2 BLAST EFFECTS

6.2.1 Shock Wave. The shock wave exhibited the characteristics of a single incident shock wave. This is verified by WT 1102, "Shock Photography and Drag Force Measurements." This report showed that the reflected shock wave caught up and merged with the incident shock wave at approximately 2,600 feet above air zero. However, there was a second disturbance noticed in the records, which could probably be attributed to a small second shock wave. This disturbance was clearly visible on the horizontal-stabilizer

TABLE 6.1 Post-Operation Static Tests of Drone Horizontal Stabilizers

Drone	Max. Applied Load-Pounds	Max. Applied Bending Moment at failure Sta. Inch-pounds	Initial Permanent Set at Tip, Inches Zero Load	Final Permanent Set at Tip, Inches
*1 Left	3400	74,800	-	-
1 Right	2700	59,400	0.60	1.33
2 Left	1750	38,500	2.36	4.0
2 Right	1400	30,800	2.75	5.32
3 Left	690	15,200	8.30	15.50
*3 Right	-	-	-	-

* Did not fail

† Right side was destroyed when drone crashed

bending-moment curves on local Recorder 1, Drone 1, which was the only local recorder readable at that time, and also appeared as a second small deflection in the airborne photography. However, it was small and too weak for a normal reflected shock wave. This phenomenon has been observed frequently in the past by Cambridge Research Center and is not believed to have affected the test results in any manner.

Time of Arrival. In Figure 6.1 shock-wave time of arrival is plotted against slant range as measured at the three drones. The data have been reduced to 1 KT at sea level standard conditions for comparison with other tests. This method of treatment is referred to as A-scaling. The actual figures for shock-wave time of arrival are given in Table 5.2. These figures represent the initial deflection of the normal acceleration trace as measured on both local recording and telemetering records for Drones 1 and 2 and from telemetering records alone for Drone 3. A curve of time

of arrival versus slant range as obtained from the data presented in Projects 1.1a and 1.2, Operation Upshot-Knothole WT-710, "Air Blast Measurements," is plotted in Figure 6.1 and is used for comparative purposes. The data for this curve have also been A-scaled and represent a composite of the results obtained during Operations Upshot-Knothole, Tumbler, and Ivy. The composite curve does not overlap the drone measurements in range, so they cannot be compared absolutely. However, extrapolation of the curve as shown by the dashed line indicates close agreement. The composite curve is based on a single incident shock wave and the measured values are for

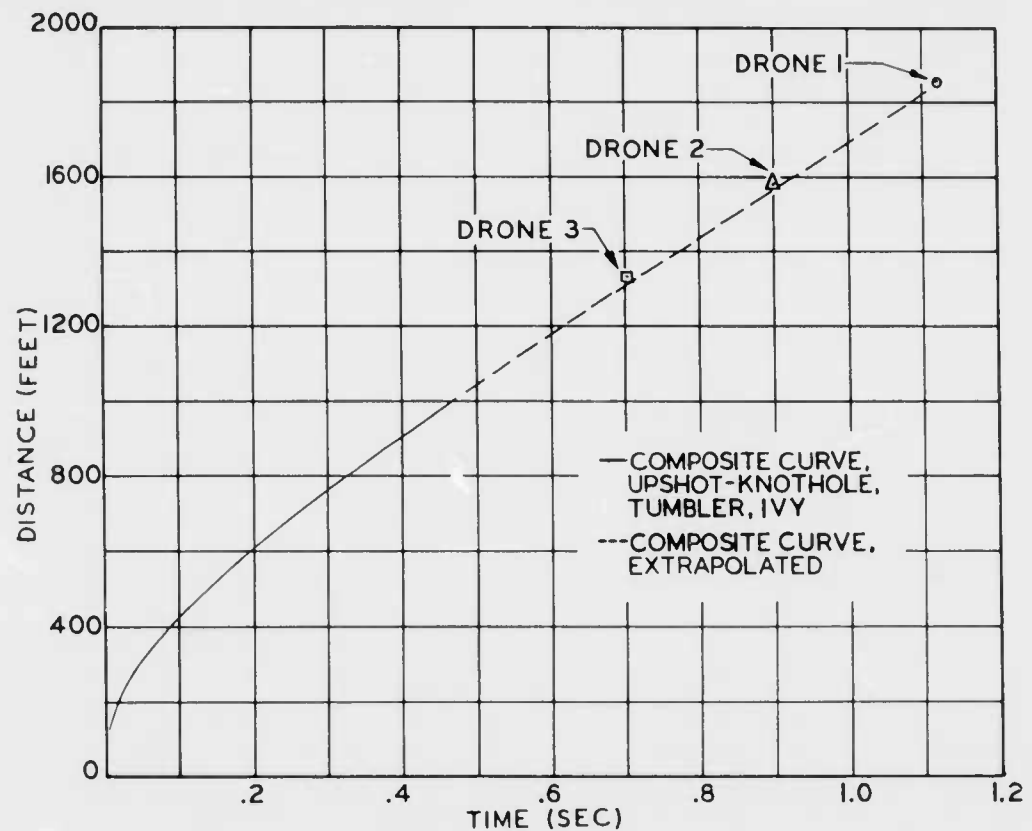


Figure 6.1 Shock Wave Time of Arrival versus Slant Range
(Data Reduced to 1 KT at Sea Level, Shot 12)

the incident wave reinforced with a reflected wave. Therefore, the measured values would normally be expected to be slightly lower than the composite.

The time of arrival for the second disturbance was about 1.63, 1.48, and 1.14 seconds after the incident shock wave for Drones 1, 2, and 3, respectively.

Overpressure. In Figure 6.2 is an A-scaled graph of overpressure versus slant range. This figure shows the comparison of overpressure measurements at the drones with the free air composite curve from Operations Upshot-Knothole, Tumbler, and Ivy as obtained from WT 1102. These overpressure measurements were obtained from the telemeter records, which

lost synchronization just after the peak acceleration was reached. Therefore the peak values were not clearly recorded, and it was necessary to extrapolate the curves obtained and to estimate the peak values reached. The figures used are the best obtainable and are believed to be reasonably

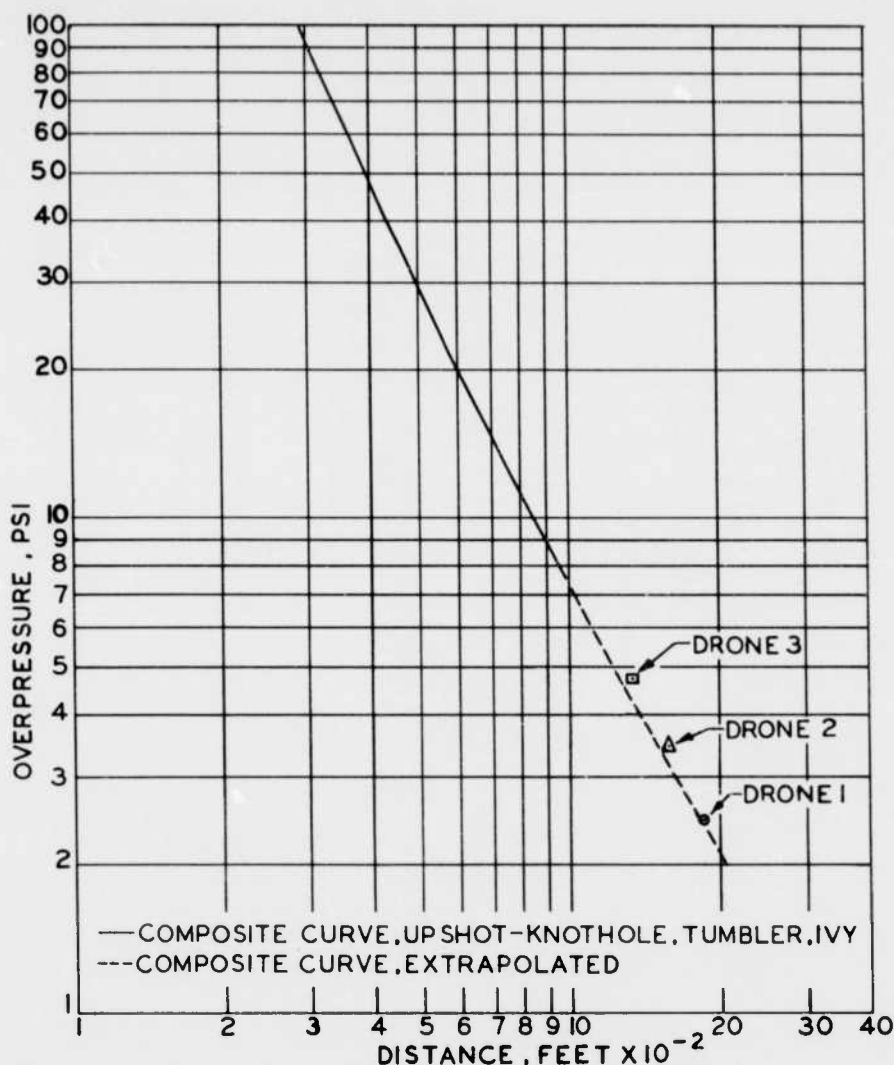


Figure 6.2 Peak Overpressure versus Slant Range
(Data Reduced to 1 KT at Sea Level, Shot 12)

accurate. In view of the method used to arrive at these figures, however, no definite accuracy limits should be assigned.

As with the time of arrival, the composite curve had to be extrapolated to include the distance range covered by the drones. This extrapolation is shown as a dashed line. The overpressure measurements at the drones exhibit close agreement with the composite curve. Since the measurements represented an incident shock wave reinforced by the reflected

shock wave, they would normally be expected to be higher than the composite as shown which represents a single free air shock wave.

6.2.2 Normal Acceleration. The values of drone normal acceleration at the CG are given in Table 5.2 and were obtained primarily from the telemeter records. These peaks were obtained in the same manner as were the overpressure values discussed in the previous section and, therefore, have the same degree of accuracy.

6.2.3 Deflections. All deflection data were obtained from the airborne cameras contained in the drone cockpits. In Table 5.5 are given the figures for maximum deflection due to the shock wave for all stations measured. For all deflection data presented, the zero reference point is taken as the position of the individual measuring station immediately before time zero. The cameras were operating at 64 frames per second, with each data point representing 1/128 second of time, and 1/128 second being missed between frames. Therefore, the cameras did not record the actual peak deflection obtained in all cases. By careful study of the data and correlating it with the actual photographs, however, it was possible to reproduce a curve through the peak deflection with essentially the same accuracy as that of the data points. In the deflection curves, presented in Chapter 5 the individual data points are not used because of the condensed time scale utilized. Instead, a faired line representing the average of the points is used. In these figures the faired curves are well within accuracy limits of the data points.

Horizontal Stabilizer. Horizontal stabilizer deflections were obtained from airborne Cameras 2 and 5. Deflections were measured at Stations 82 and 94 on each side. Painted stripes on the vertical stabilizer were used as reference marks to obtain deflections from measurements read on the film. The measured differences were then multiplied by the previously determined calibration factor to convert the readings to inches of deflection. From an analysis of the reading method and equipment used, the accuracy of the individual data points is found to be ± 0.5 inch.

On the horizontal-stabilizer-deflection curves of Chapter 5, the deflection prior to shock arrival is caused by the thermal input to the lower skin. The deflection curves are similar for all measuring stations on a given stabilizer, except for the magnitude of the deflections obtained. The frequency of the deflection cycles is essentially the same for all stations on all stabilizers, even though the amount of load varied considerably.

In Figure 6.3 is presented a portion of the sequence of photographs for Drone 1 which were used to measure the horizontal-stabilizer deflections presented in this report. These photographs cover the shock arrival and about the first 0.18 second after shock arrival, or past the two major peaks. Comparable illustrations are shown in Figures 6.4 and 6.5 for Drones 2 and 3.

An interesting photograph is shown in Figure 6.5, Sheet 1, at 2.07 seconds on the right side of the page. In this picture the camera caught two images of the left side of the horizontal stabilizer, one just before failure was reached and the other just after. Since the exposure time of

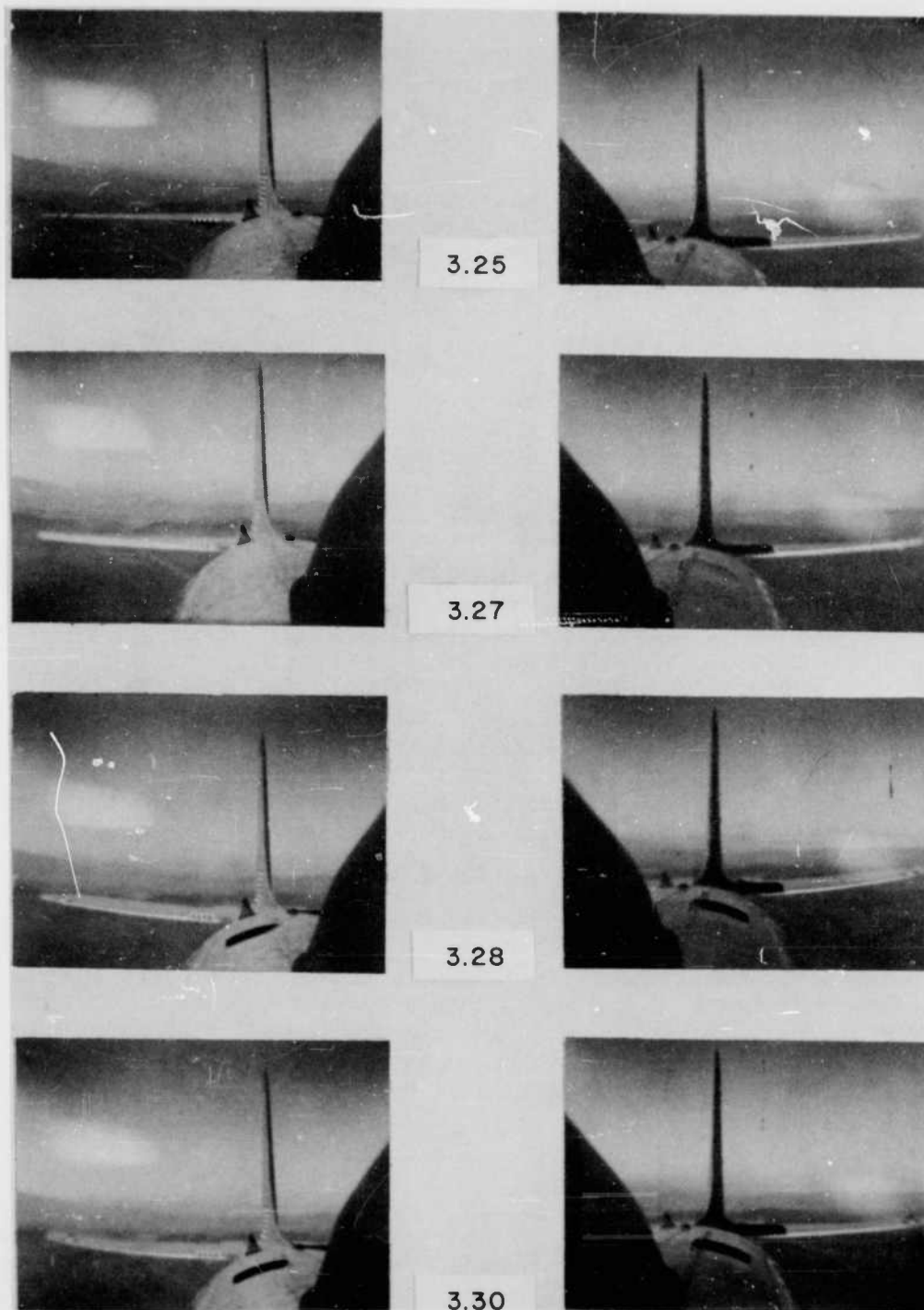


Figure 6.3 Horizontal Stabilizer Deflection at Shock Arrival,
Drone 1. Numbers represent seconds after time zero.



3.32



3.33



3.35



3.36



Figure 6.3 Continued.

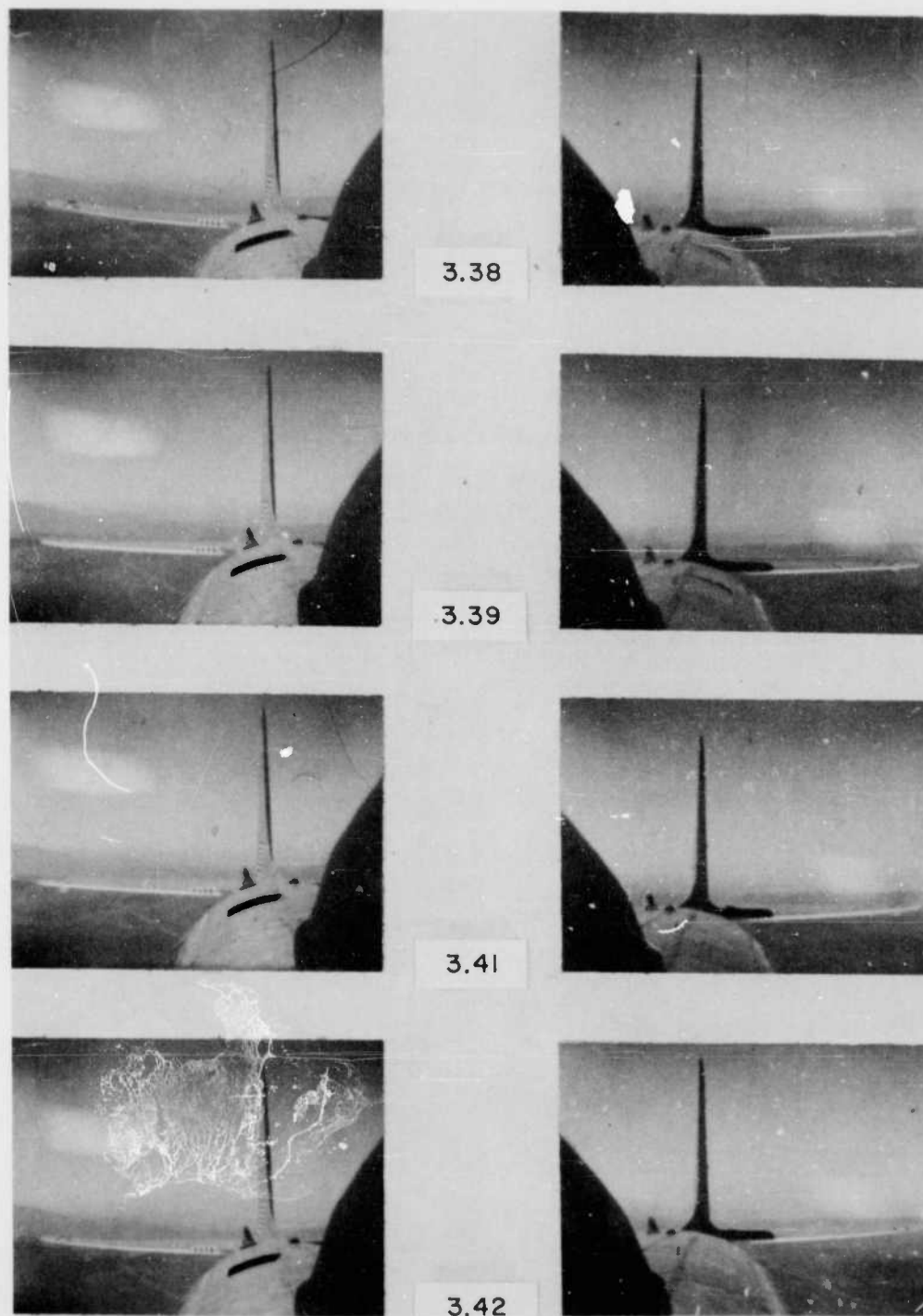


Figure 6.3 Continued.

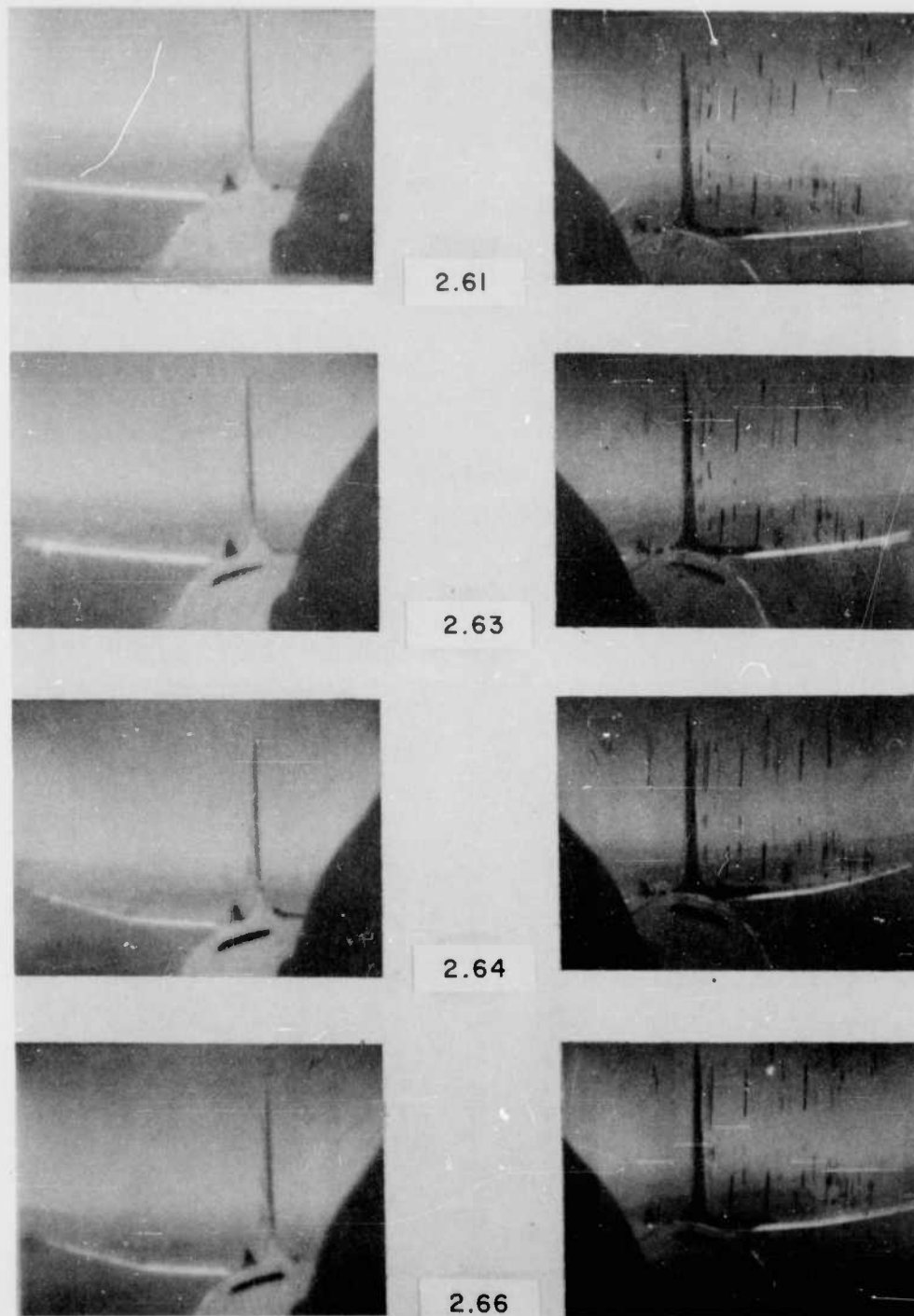


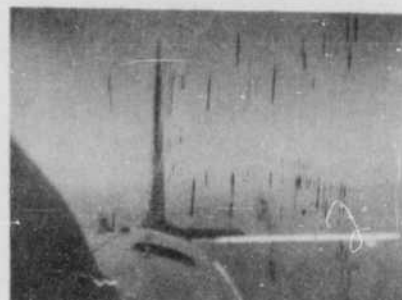
Figure 6.4 Horizontal Stabilizer Deflection at Shock Arrival, Drone 2. Numbers represent seconds after time zero.



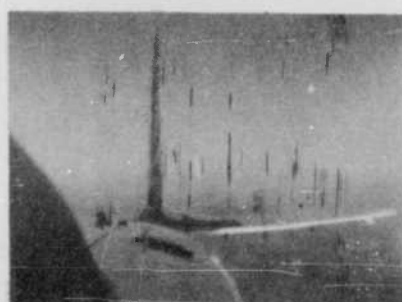
2.68



2.69



2.71



2.72

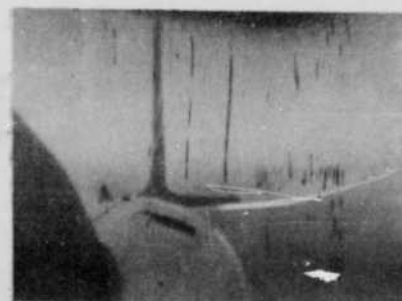
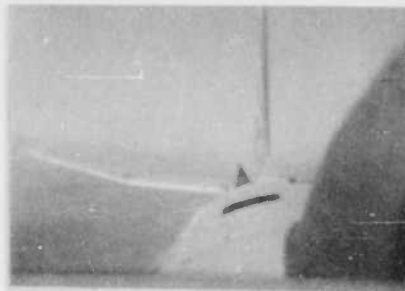
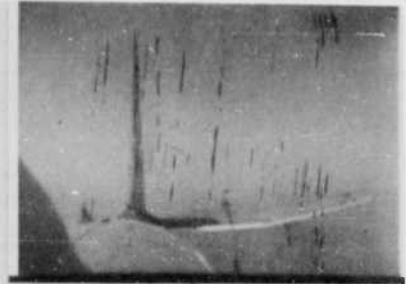


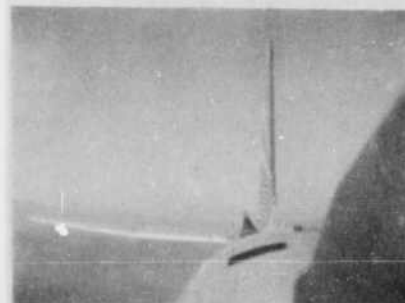
Figure 6.4 Continued.



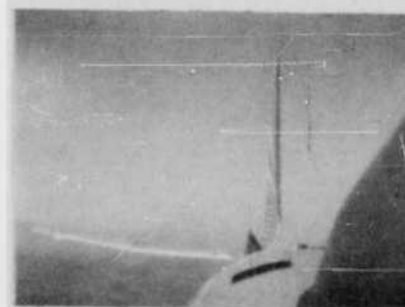
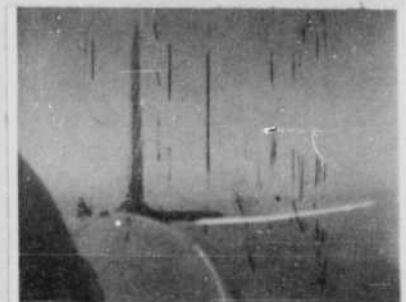
2.74



2.75



2.77



2.78

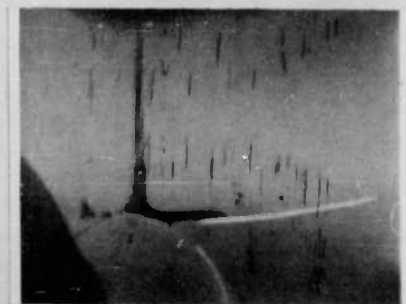


Figure 6.4 Continued.

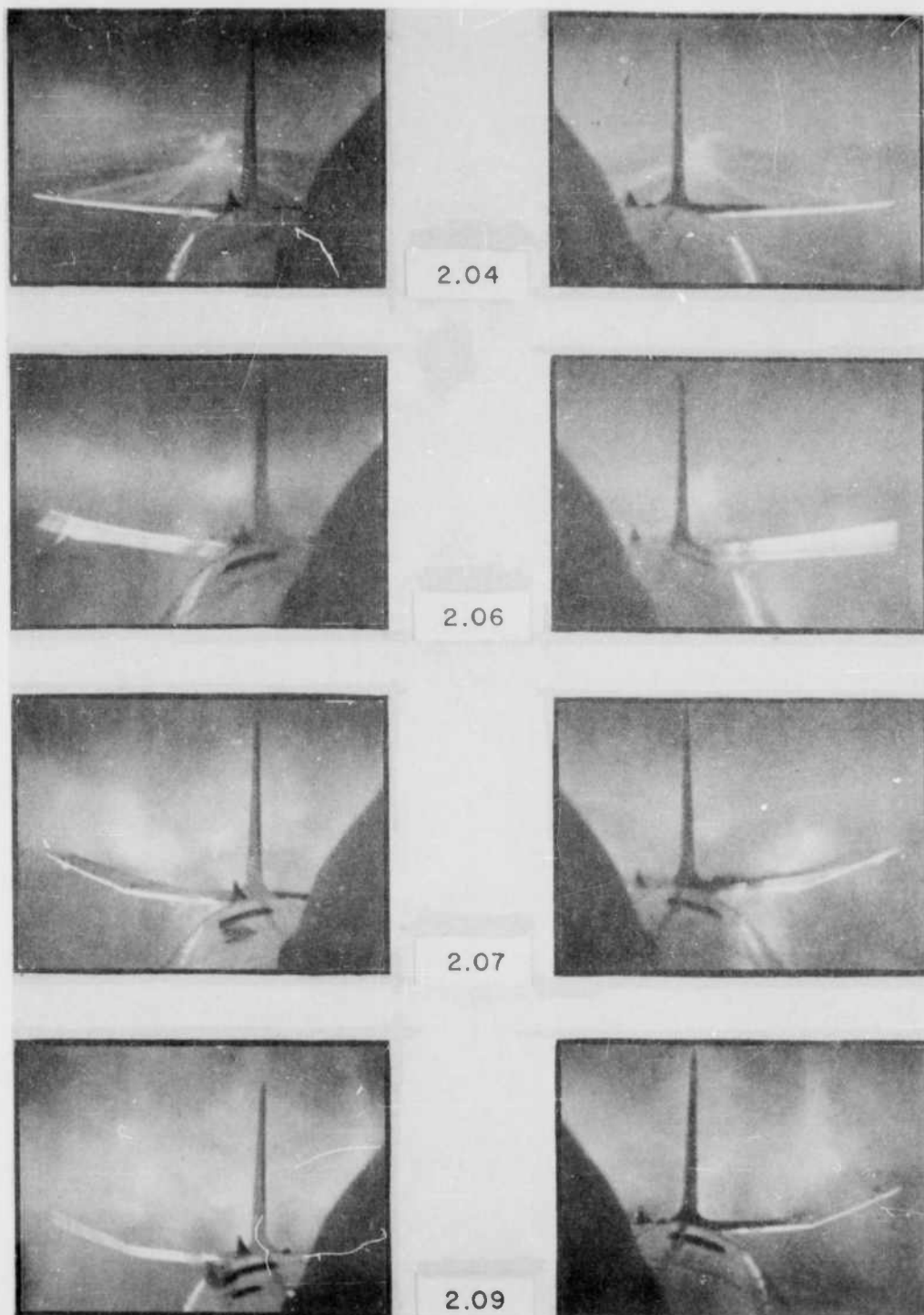


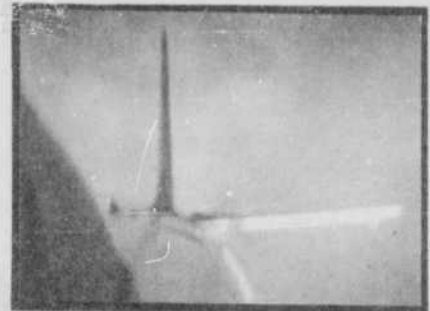
Figure 6.5 Horizontal Stabilizer Deflection at Shock Arrival, Drone 3. Numbers represent seconds after time zero.



2.11



2.12



2.14



2.15

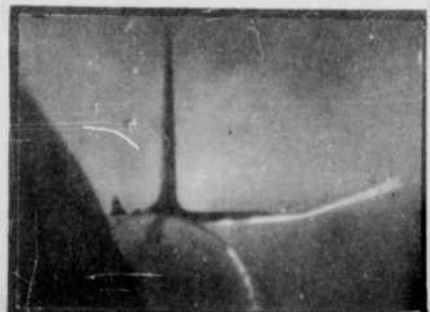
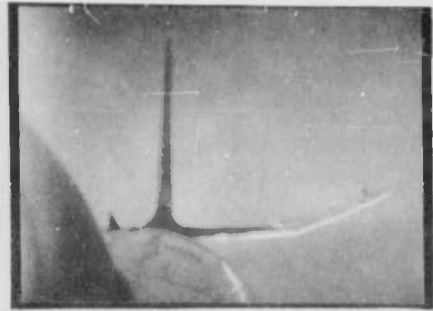


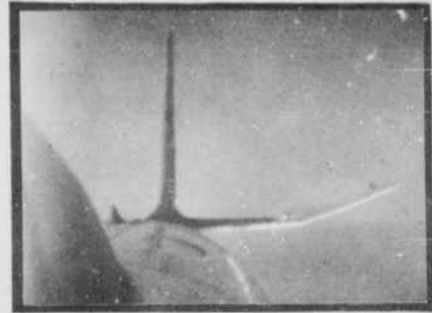
Figure 6.5 Continued.



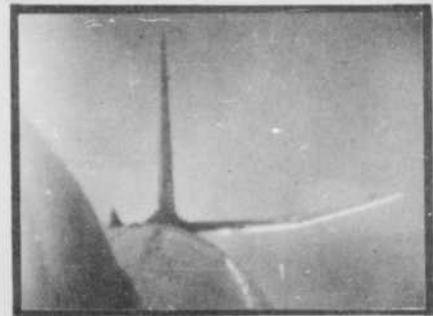
2.17



2.18



2.20



2.21

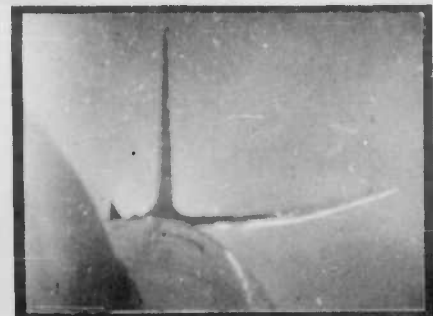


Figure 6.5 Continued.

this frame is less than 0.008 second, the picture clearly shows the rapidity of stabilizer movement and the wide range of position covered by a single frame.

Wing. The wing deflections shown in Table 5.5 were obtained from airborne Cameras 3 and 4. Deflections were measured at Stations 89, 145 (20 percent and 50 percent chord) and 213 on each wing. Medallions painted on the upper wing surface at these locations were used as reference marks. Readings were taken of these marks before time zero and continuing throughout the test. By multiplication of the relative change in position of these medallions by the previously determined calibration factor, the deflection in inches was obtained. From an analysis of reading method and equipment used, the accuracy of the individual data points is found to be ± 0.6 inch at Station 213 and ± 0.3 inch at Station 89. The complete deflection time histories for all wing stations are presented in WADC TN55-545, "Data Results for Destructive Loads on Aircraft in Flight."

As seen from the wing-deflection figures presented in Chapter 5, the wing oscillations generally show the same period for each drone, but the maximum deflection does not always occur at the same cycle. Also, the different stations on the same wing do not always reach maximum deflection at the same cycle. In general, the inboard stations reach their maximum at the first peak, whereas the outboard stations reach their maximum at the second peak. This is possibly caused by the wing dihedral, which results in the initial impact of the shock wave first being felt inboard at the fuselage. The inconsistencies of the deflection peaks are probably due to the interaction of the blast loading, aerodynamic damping, and the natural frequency of the wing structure.

Fuselage. Fuselage deflection was obtained from airborne Cameras 2 and 5 and was measured at Station 373. Reference marks were painted on the vertical stabilizer a little aft of the leading edge. The change in position of these marks was measured and multiplied by the calibration factor to obtain deflection in inches. The accuracy of the individual data points is ± 0.54 inches. A typical fuselage deflection-versus-time history is presented in Figure 6.6.

6.2.4 Bending Moments. In this section only the bending moments due to the shock wave are discussed. Since these were obtained from the local recorder for Drone 1 only, there is no correlation between data sources or between drones, and only Drone 1 is considered. The records from which this data were obtained were very weak for about 0.2 second after shock arrival and were not clearly legible. However, careful study of the records and close correlation with the deflection curves made it possible to construct a reasonable estimate of the trace deflection for this drone. However, these values must be considered as estimates only and must be used with caution.

A typical bending-moment curve is presented in Figure 6.7, with the dashed line representing that portion of the curve which was not clearly legible on the record. In this figure the strain-gage response is termed "apparent" bending moment, because it includes the thermal effects at time zero which are not actually bending moment.

The peak values of bending moment obtained at all measuring stations are presented in Table 5.3. In Figure 6.8 the peak bending moments measured

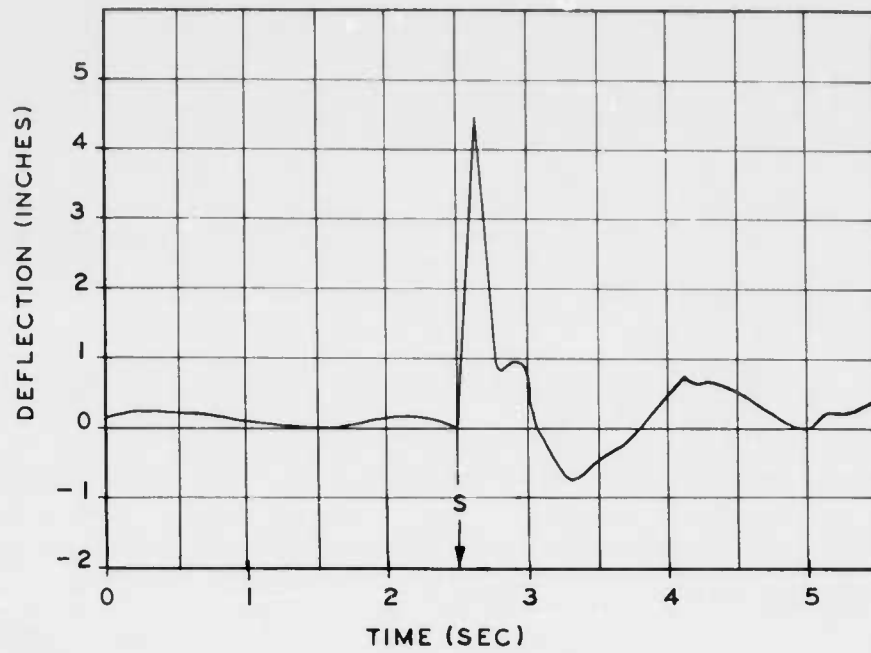


Figure 6.6 Fuselage Deflection versus Time After T_0 ,
Station 373, Drone 2

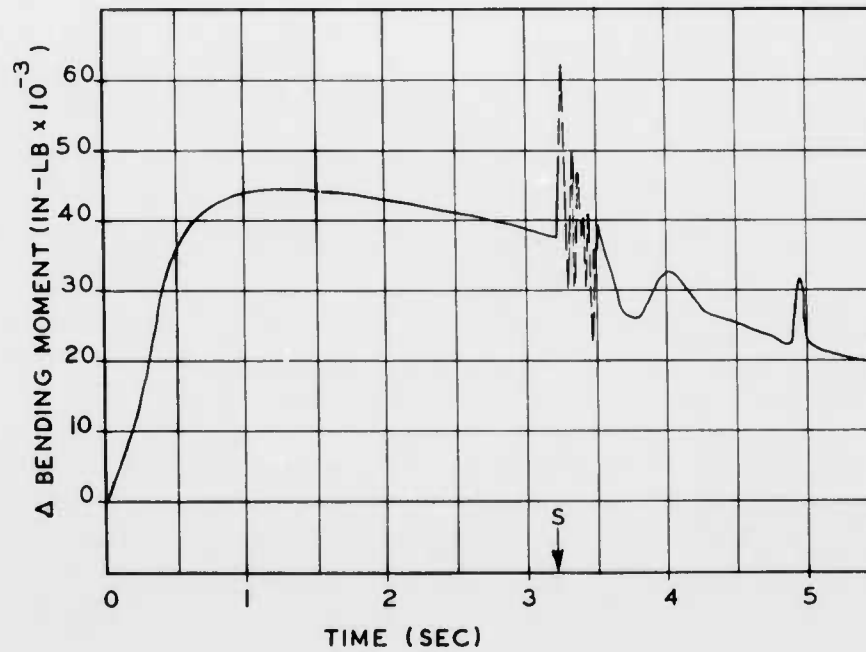


Figure 6.7 Horizontal Stabilizer Apparent Bending Moment,
Station 43 Left, Drone 1

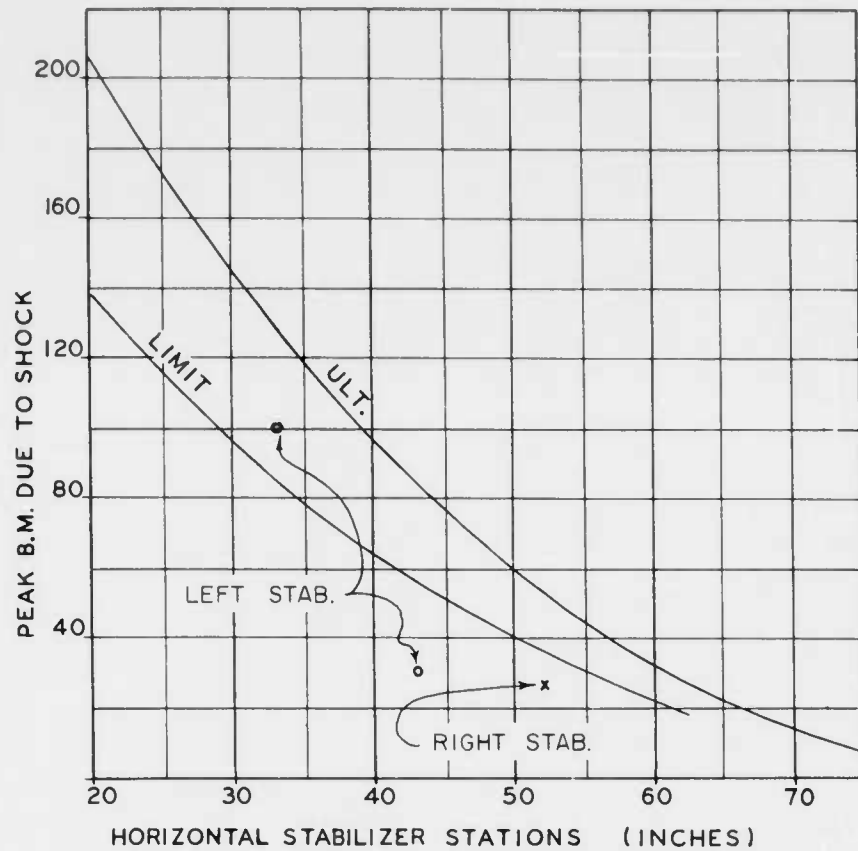


Figure 6.8 Comparison Between Peak Bending Moments and Limit Loads, Drone 1

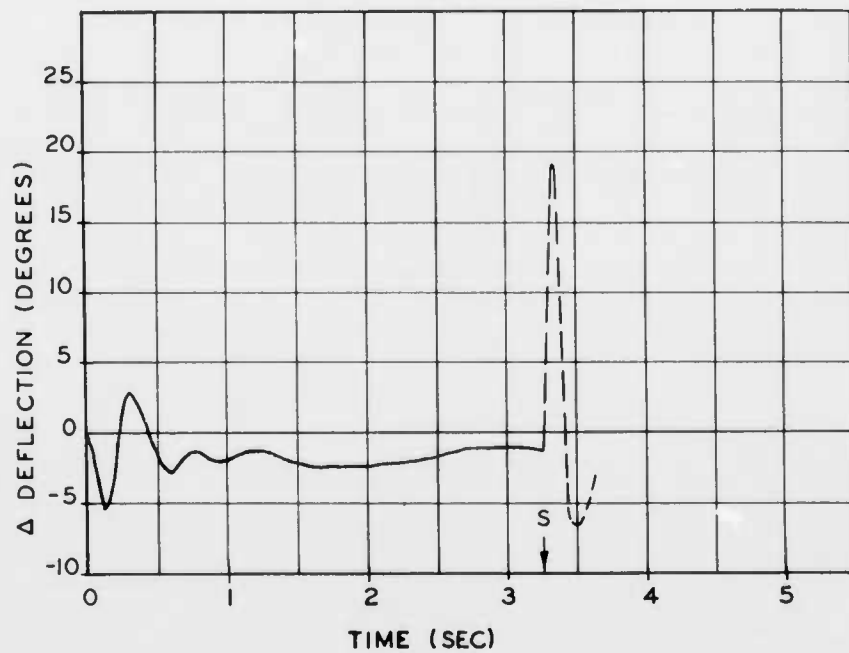


Figure 6.9 Elevator Deflection. Station Zero, Drone 1

are plotted against horizontal-stabilizer station and compared with limit load. This graph shows that the measurement at Station 43 does not form a smooth curve with Stations 33 and 52 and is far below limit load. It is therefore assumed to be in error. This is possibly due in part to the proximity of the bending moment measuring station to the actual break station.

6.2.5 Elevator Deflection. In Figure 6.9 is presented the elevator deflections at Station 0 on Drone 1. The elevator deflection for Drone 1 was obtained from the local recorder records and for Drones 2 and 3 from the telemeter records. The values of elevator deflection at shock arrival are obtained in the same manner as the bending moments discussed in the previous section and should be treated accordingly.

Except for the deflection at shock arrival, the curve of Figure 6.9 is typical of all three drones. For Drones 2 and 3 no deflections were measured after shock arrival. Although the amount of deflection varied from -5° on Drone 1 to -9° on Drone 3, it was generally the same for all stations on a given drone. The oscillation immediately following time zero was observed to have the same approximate period for all drones. The amplitude, however, varied inversely with the distance from the blast. This oscillation was also observed on all drone instrument-panel cameras as control-stick motion. No explanation of this phenomenon can be advanced at this time, however.

6.3 THERMAL EFFECTS

6.3.1 Thermal Inputs. Thermal data were obtained from the local recorder until 10 seconds after shock arrival on Drone 1 and until shock arrival on Drone 2. Thermal data were also obtained from the telemeter records until shock arrival on all three drones. The rate of thermal energy input and the total thermal energy were measured by radiometers and calorimeters developed by the Naval Radiological Defense Laboratory. The data have been corrected for the effect of the quartz filter used during the test and for aircraft misalignment at time zero. All thermal information presented here are considered reliable and within the accuracy normally attributed to flight-test measurements using this type of instrument.

Time-history curves of thermal-energy rate, total thermal energy and horizontal-stabilizer skin temperature are given in Figure 6.10. These curves are typical of all drones, except for peak values obtained. As expected, the decline of thermal energy rate between 0.2 and 0.7 second was slower for Drone 3 and faster for Drone 1 than that shown for Drone 2. The total thermal energy leveled off at 5 to 6 seconds, and skin temperature reached a maximum at 2 to 3 seconds. The maximum values measured for all drones are given in Table 5.3.

6.3.2 Protective Paint. From inspection of the recovered stabilizers, it was apparent that the white paint used on the lower surfaces was effective in minimizing thermal damage. Even on the lower drone there probably would not have been severe burning had there not been the black painted markers. Calculations based on data from this test show the absorptivity to have

been about 14 percent which is good as compared with conventional paints. On the lower drone, however, there was indication that the paint was beginning to break down and would not be able to withstand appreciably increased thermal input. On the lower surface of the horizontal stabilizer, there were a few areas which were initially free of blemishes or markers,

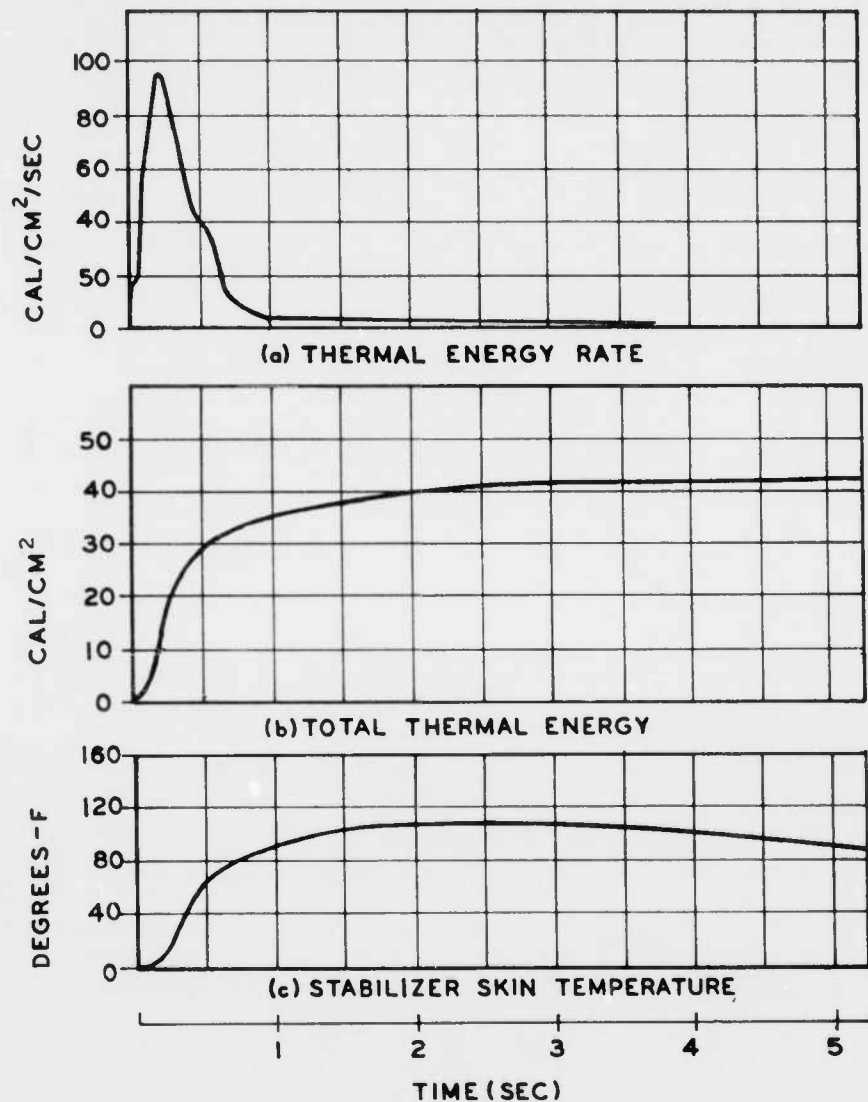


Figure 6.10 Thermal Curves, Drone 1

but which were scorched and blistered after the tests. Therefore, for future applications where higher temperatures are expected, it will probably be necessary to use a more-effective thermal protection.

6.3.3 Thermal Stress. The outputs referred to in this section were obtained from strain-gage bridges designed to measure bending moment and

calibrated only in terms of bending moment. Due to the special requirements of this installation, it was impractical to make these bridges insensitive to certain other forces, particularly end forces. Regardless of the disturbing force, however, all bridge outputs were necessarily read as bending moment, because of the manner in which they were cali-

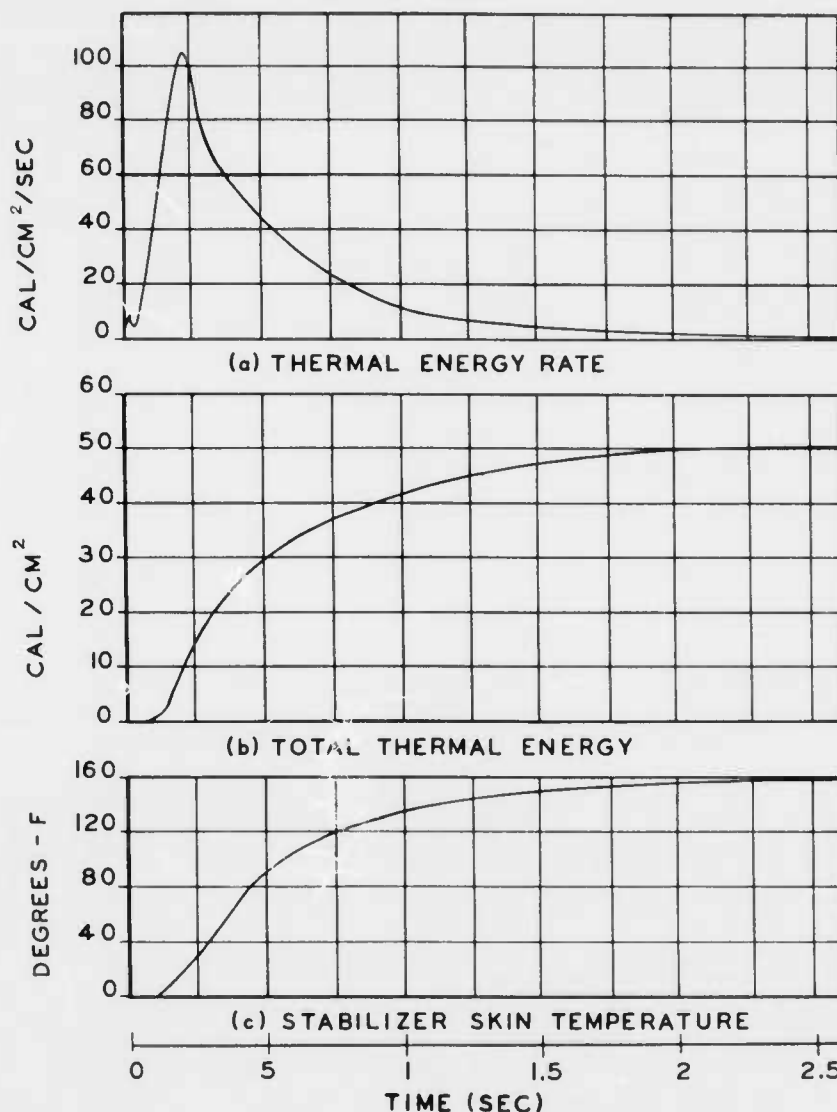


Figure 6.11 Thermal Curves, Drone 2

brated. Since these measurements can (and in this case obviously do) contain stresses other than bending moments, they are termed "apparent bending moments."

There was an appreciable amount of thermal strain present in the horizontal stabilizer on all drones at shock arrival. This was indicated by the deflection of the horizontal stabilizer measured by the

cameras between time zero and shock arrival and shown in the deflection figures of Chapter 5. This was also shown by the large deflections of the bending moment curves between time zero and shock arrival (see Figure 6.7).

The effect of the thermal input to the stabilizer was to heat the lower skin, which expanded and exerted a tensile stress (end force) on

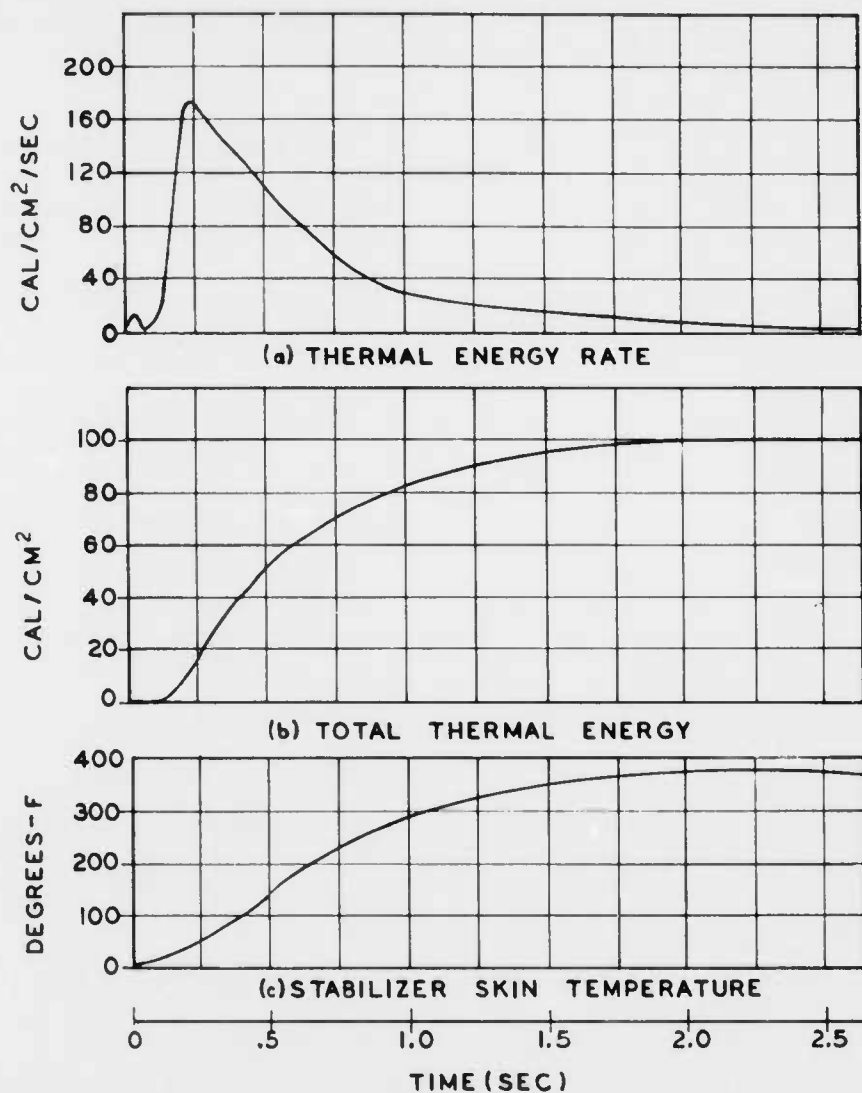


Figure 6.12 Thermal Curves, Drone 3

the adjacent spars and stringers. Since the skin expansion was resisted almost entirely by these members (to which the strain gages were attached) the output from the bridges was considerable. Thus the strain gages were affected in the same manner as though a large external bending moment were applied to the structure in the same direction as the gust load. These measurements are given in Table 5.6 and show that on the bottom drone the

apparent bending moment due to thermal-induced stress was greater than the bending moment required to produce failure of the stabilizer at Station 43. Since this is not an actual bending moment, it should not necessarily be expected to result in stabilizer failure. However, it is possible that as a result of this stress, the structure is materially weakened with respect to external load-carrying ability.

The expansion of the heated skin and the restraining effect of the remaining members acted as a couple which produced the deflection referred to above. This couple, and the resulting deflection, were much less than would have accompanied an equivalent amount of strain in the bridge circuits due to pure bending moment.

The temperature rise at certain strain-gage locations was measured by resistance-thermometer elements placed adjacent to the strain gages. These elements indicated that there was no appreciable strain-gage temperature rise at the time of maximum skin temperature. It is therefore unlikely that there were any appreciable errors in strain-gage output due to temperature effects on the gages at the time of maximum output.

It is difficult to convert the apparent bending moment reading to accurate strain measurements at a given point in the structure, because of the involved bridge circuitry necessitated by the multiple-gage installations. The readings were further affected by the various weighing factors applied to the individual strain gages. An attempt was made, however, to obtain an estimate of thermal effects by analysing the bending-moment measurement immediately following time zero.

During a typical bending moment calibration, the individual strains were measured and a relationship was established between composite strain-gage-bridge output (in percent of calibrate signal) and actual strain of the individual structural members. This calibration showed that for a composite strain of 88 percent calibration at bending moment Station 43, the highest stressed member had a strain of 1607μ in./in. with an average strain of 925μ in./in. for all members.

This relationship is valid, however, only for the particular loading condition for which it was established and cannot be rigorously applied to thermally induced stress. For application to thermally induced stress, an estimate was obtained by taking the average stress per member measured during bending moment calibration (i.e. 925μ in./in. for 88 percent calibration). During the subject test a strain of 143 percent calibration was measured at Station 43 on the bottom drone. Using the relationship established above, this indicates a strain of $1,500 \mu$ in./in. in the spars and stringers, which is about 40 percent of the tensile yield strength.

An attempt was made to verify these figures by calculations. It was assumed that the skin was uniformly heated to the measured temperature, and the thermal expansion of the skin was then calculated. An estimate was made of the amount of area of the internal structure effective in restraining the skin. On this basis it was found that the elongation of the "cold" stringers was approximately equal to that required to produce the measured trace deflection. It is felt that the recorded outputs represent actual thermal strain in the structure.

Under the conditions outlined above, by the time the upper-surface compressive-yield strength would be reached due to gust loading, the ultimate tensile strength would have been reached in the lower spar and

stringer. Therefore the horizontal stabilizer of Drone 3 had reached the point where the thermal input was probably sufficient to produce some structural weakening. Any further increase in thermal input could conceivably have an appreciable effect on the ability of the stabilizer to withstand external load.

Chapter 7

CONCLUSIONS

The following conclusions are based on the information presented and discussed in the previous chapters of this report.

1. Much valuable test data were obtained which should permit further evaluation of existing theoretical methods of calculating blast-imposed loads on aircraft and modification of these methods to include the post-buckling range.

2. The test drones were not damaged as severely as anticipated. None of the drones were destroyed by the blast, even though controllability was sufficiently affected on Drone 3 to prevent its return to base by remote control.

3. The lethal-volume contour was not bracketed and an actual check point on the lethal-volume contour was not obtained. It is probable, however, that the contour for an F-80 aircraft can be estimated with reasonable accuracy by extrapolation from the data obtained in this test.

4. As developed for this program, the concept of the amount of damage necessary to insure complete destruction of the aircraft in flight was conservative.

5. The drones were critical to gust loading at the horizontal stabilizer, as predicted. The primary break station (10 to 20) was undamaged, however, and the actual break occurred at the secondary break station (40 to 50).

6. Although the drones were not positioned within absolute tolerances, they were close enough to the assigned positions to obtain data sufficient to accomplish the objectives of this program.

7. The local recording and telemetering systems used in this test were not adequate in their present form for this type of application.

8. Thermal strains were sufficiently large to become a contributing factor to gust failure as aircraft come closer to air zero.

9. The white protective paint used on the bottom surface considerably reduced heat input to the structure and damage resulting therefrom. For future nuclear tests where the anticipated thermal inputs will be higher than those reported herein, a more-effective method of thermal insulation than the paint used in this test will be necessary.

10. The 20 percent reduction in yield below that anticipated had an undesirable effect on the project results, but satisfactory results were attained nevertheless.

Chapter 8

RECOMMENDATIONS

On the basis of the information presented and discussed in this report and the conclusions drawn therefrom, the following recommendations are made:

1. The data contained herein should be made available to interested personnel for use in the evaluation and modification of theoretical methods for calculating destructive loads on aircraft flying in the vicinity of a nuclear explosion.

2. The concept of the level of inputs necessary for destruction of aircraft in flight as contrasted to "safe delivery" should be reviewed and, if necessary, modified to conform more closely with the results of this test.

3. Further development, and, modification of the data recording equipment used in this test should be accomplished in order to perfect a system or systems which can accurately and reliably record and transmit data under conditions resulting from the close proximity to a nuclear explosion such as were encountered in this test.

DISTRIBUTION

Military Distribution Category 5-10

ARMY ACTIVITIES

- 1 Asst. Dep. Chief of Staff for Military Operations, D/A, Washington 25, D.C. ATTN: Asst. Executive (R&SW)
- 2 Chief of Research and Development, D/A, Washington 25, D.C. ATTN: Atomic Division
- 3 Chief of Ordnance, D/A, Washington 25, D.C. ATTN: ORDTX-AR
- 4 Chief Signal Officer, D/A, P&O Division, Washington 25, D.C. ATTN: SIGRD-8
- 5 The Surgeon General, D/A, Washington 25, D.C. ATTN: MEDNE
- 6-7 Chief Chemical Officer, D/A, Washington 25, D.C.
- 8 The Quartermaster General, D/A, Washington 25, D.C. ATTN: Research and Development
- 9-11 Chief of Engineers, D/A, Washington 25, D.C. ATTN: ENGINE
- 12 Chief of Transportation, Military Planning and Intelligence Div., Washington 25, D.C.
- 13-15 Commanding General, Headquarters, U. S. Continental Army Command, Ft. Monroe, Va.
- 16 President, Board #1, Headquarters, Continental Army Command, Ft. Sill, Okla.
- 17 President, Board #2, Headquarters, Continental Army Command, Ft. Knox, Ky.
- 18 President, Board #3, Headquarters, Continental Army Command, Ft. Benning, Ga.
- 19 President, Board #4, Headquarters, Continental Army Command, Ft. Bliss, Tex.
- 20 Commanding General, Headquarters, First U. S. Army, Governor's Island, New York 4, N.Y.
- 21 Commanding General, Headquarters, Second U. S. Army, Ft. George G. Meade, Md.
- 22 Commanding General, Headquarters, Third U. S. Army, Ft. McPherson, Ga. ATTN: ACOFS, G-3
- 23 Commanding General, Headquarters, Fourth U. S. Army, Ft. Sam Houston, Tex. ATTN: G-3 Section
- 24 Commanding General, Headquarters, Fifth U. S. Army, 1660 E. Hyde Park Blvd., Chicago 15, Ill.
- 25 Commanding General, Headquarters, Sixth U. S. Army, Presidio of San Francisco, San Francisco, Calif. ATTN: AMGCT-4
- 26 Commanding General, U.S. Army Caribbean, Ft. Amador, C.Z. ATTN: Cml. Off.
- 27 Commanding General, USARFANT & MDPF, Ft. Brooke, Puerto Rico
- 28 Commanding General, Southern European Task Force, APO 168, New York, N.Y. ATTN: ACOFS, G-3
- 29 Commanding General, U.S. Army Forces Far East (Main), APO 343, San Francisco, Calif. ATTN: ACOFS, G-3
- 30 Commanding General, U.S. Army Alaska, APO 942, Seattle, Wash.
- 31-32 Commanding General, U.S. Army Europe, APO 403, New York, N.Y. ATTN: OPOT Div., Combat Dev. Br.
- 33-34 Commanding General, U.S. Army Pacific, APO 958, San Francisco, Calif. ATTN: Cml. Off.
- 35-36 Commandant, Command and General Staff College, Ft. Leavenworth, Kan. ATTN: ALLIS(AS)
- 37-39 Commandant, Army War College, Carlisle Barracks, Pa. ATTN: Library
- 40 Commandant, The Infantry School, Ft. Benning, Ga. ATTN: C.D.S.
- 41 Commandant, The Artillery and Missile School, Ft. Sill, Okla.
- 42 Secretary, The U. S. Army Air Defense School, Ft. Bliss, Texas. ATTN: Maj. Gregg D. Breitigan, Dept. of Tactics and Combined Arms
- 43 Commandant, The Armored School, Ft. Knox, Ky.
- 44 Commanding General, Army Medical Service School, Brooke Army Medical Center, Ft. Sam Houston, Tex.

- 45 Director, Special Weapons Development Office, Headquarters, CONARC, Ft. Bliss, Tex. ATTN: Capt. T. E. Skinner
- 46 Commandant, Walter Reed Army Institute of Research, Walter Reed Army Medical Center, Washington 25, D. C.
- 47 Superintendent, U.S. Military Academy, West Point, N. Y. ATTN: Prof. of Ordnance
- 48 Commandant, Chemical Corps School, Chemical Corps Training Command, Ft. McClellan, Ala.
- 49-50 Commanding General, U. S. Army Chemical Corps., Research and Development Command, Washington, D.C.
- 51-52 Commanding General, Aberdeen Proving Grounds, Md. ATTN: Director, Ballistice Research Laboratory
- 53 Commanding General, The Engineer Center, Ft. Belvoir, Va. ATTN: Asst. Commandant, Engineer School
- 54 Commanding Officer, Engineer Research and Development Laboratory, Ft. Belvoir, Va. ATTN: Chief, Technical Intelligence Branch
- 55 Commanding Officer, Picatinny Arsenal, Dover, N.J. ATTN: ORDBE-TK
- 56 Commanding Officer, Frankford Arsenal, Philadelphia 37, Pa. ATTN: Col. Teevee Kundel
- 57 Commanding Officer, Army Medical Research Laboratory, Ft. Knox, Ky.
- 58-59 Commanding Officer, Chemical Warfare Laboratories, Army Chemical Center, Md. ATTN: Tech. Library
- 60 Commanding Officer, Transportation R&D Station, Ft. Eustis, Va.
- 61 Commandant, The Transportation School, Ft. Eustis, Va. ATTN: Security and Information Officer
- 62 Director, Technical Documents Center, Evans Signal Laboratory, Belmar, N.J.
- 63 Director, Waterways Experiment Station, PO Box 631, Vicksburg, Miss. ATTN: Library
- 64 Director, Operations Research Office, Johns Hopkins University, 7100 Connecticut Ave., Chevy Chase, Md. Washington 15, D.C.
- 65 Commanding General, Quartermaster Research and Development, Command, Quartermaster Research and Development Center, Natick, Mass. ATTN: CBR Liaison Officer
- 66 Commanding Officer, Diamond Ordnance Fuze Laboratories, Washington 25, D. C. ATTN: Coordinator, Atomic Weapons Effects Tests
- 67-71 Technical Information Service Extension, Oak Ridge, Tenn.

NAVY ACTIVITIES

- 72 Director, USMC Educational Center, Marine Corps Schools, Quantico, Va.
- 73-74 Chief of Naval Operations, D/N, Washington 25, D. C. ATTN: OP-36
- 75 Chief of Naval Operations, D/N, Washington 25, D.C. ATTN: OP-37
- 76 Chief of Naval Operations, D/N, Washington 25, D.C. ATTN: OP-03EG
- 77 Director of Naval Intelligence, D/N, Washington 25, D.C. ATTN: OP-922V
- 78 Chief, Bureau of Medicine and Surgery, D/N, Washington 25, D.C. ATTN: Special Weapons Defense Div.
- 79 Chief, Bureau of Ordnance, D/N, Washington 25, D.C.
- 80 Chief of Naval Personnel, D/N, Washington 25, D.C.
- 81 Chief, Bureau of Ships, D/N, Washington 25, D.C. ATTN: Codo 348
- 82 Chief, Bureau of Yards and Docks, D/N, Washington 25, D.C. ATTN: D-440
- 83 Chief, Bureau of Supplies and Accounts, D/N, Washington 25, D.C.
- 84-85 Chief, Bureau of Aeronautics, D/N, Washington 25, D.C.
- 86 Chief of Naval Research, Department of the Navy Washington 25, D.C. ATTN: Code 811

- 87- 88 Commander-in-Chief, U.S. Atlantic Fleet, U.S. Naval Base, Norfolk 11, Va.
- 89 Commandant, U.S. Marine Corps, Washington 25, D.C. ATTN: Code AO3H
- 90 President, U.S. Naval War College, Newport, R.I.
- 91 Superintendent, U.S. Naval Postgraduate School, Monterey, Calif.
- 92 Commanding Officer, U.S. Naval Schools Command, U.S. Naval Station, Treasure Island, San Francisco, Calif.
- 93 Director, USMC Development Center, USMC Schools, Quantico, Va.
- 94 Commanding Officer, U.S. Fleet Training Center, Naval Base, Norfolk 11, Va. ATTN: Special Weapons School
- 95- 96 Commanding Officer, U.S. Fleet Training Center, Naval Station, San Diego 36, Calif. ATTN: (SPWP School)
- 97 Commanding Officer, Air Development Squadron 5, VX-5, China Lake, Calif.
- 98 Commanding Officer, U.S. Naval Damage Control Training Center, Naval Base, Philadelphia, Pa. ATTN: ABC Defense Course
- 99 Commander, U.S. Naval Ordnance Laboratory, Silver Spring 19, Md. ATTN: EE
- 100 Commander, U.S. Naval Ordnance Laboratory, Silver Spring 19, Md. ATTN: EH
- 101 Commander, U.S. Naval Ordnance Laboratory, Silver Spring 19, Md. ATTN: R
- 102 Commander, U.S. Naval Ordnance Test Station, Inyokern, China Lake, Calif.
- 103 Officer-in-Charge, U.S. Naval Civil Engineering Res. and Evaluation Lab., U.S. Naval Construction Battalion Center, Port Hueneme, Calif. ATTN: Code 753
- 104 Commanding Officer, U.S. Naval Medical Research Inst., National Naval Medical Center, Bethesda 14, Md.
- 105 Director, Naval Air Experimental Station, Air Material Center, U.S. Naval Base, Philadelphia, Penn.
- 106 Director, U.S. Naval Research Laboratory, Washington 25, D.C. ATTN: Mrs. Katherine H. Cass
- 107 Director, The Material Laboratory, New York Naval Shipyard, Brooklyn, N. Y.
- 108 Commanding General, Fleet Marine Force, Atlantic, Norfolk, Va.
- 109 Commanding Officer and Director, U.S. Navy Electronics Laboratory, San Diego 52, Calif.
- 110-113 Commanding Officer, U.S. Naval Radiological Defense Laboratory, San Francisco, Calif. ATTN: Technical Information Division
- 114 Officer-in-Charge, Special Weapons Supply Depot, U.S. Naval Supply Center, Norfolk 11, Va.
- 115 Commanding Officer and Director, David W. Taylor Model Basin, Washington 7, D.C. ATTN: Library
- 116 Commander, U.S. Naval Air Development Center, Johnsville, Pa.
- 117 Commanding Officer, Clothing Supply Office, Code 1D-0, 3rd Avenue and 29th St., Brooklyn, N.Y.
- 118 Commandant, U.S. Coast Guard, 1300 E. St. N.W., Washington 25, D.C. ATTN: (OIN)
- 119 Commanding General, Fleet Marine Force, Pacific, Fleet Post Office, San Francisco, Calif.
- 120 Commander-in-Chief Pacific, Pearl Harbor, Th
- 121 Commander, Norfolk Naval Shipyard, Portsmouth 8, Va. ATTN: Code 270
- 122-126 Technical Information Service Extension, Oak Ridge, Tenn. (Surplus)
- AIR FORCE ACTIVITIES
- 127 Asst. for Atomic Energy Headquarters, USAF, Washington 25, D.C. ATTN: DCS/O
- 128 Asst. for Development Planning, Headquarters, USAF, Washington 25, D.C.
- 129 Deputy for Materiel Atomic Energy Control, Asst. for Materiel Program Control, DCS/M, Headquarters, USAF, Washington 25, D. C. ATTN: AFMPC-AE
- 130 Director of Operations, Headquarters, USAF, Washington 25, D.C. ATTN: Operations Analysis
- 131 Director of Operations, Headquarters, USAF, Washington 25, D.C.
- 132 Director of Plans, Headquarters, USAF, Washington 25, D.C. ATTN: War Plans Div.
- 133 Director of Requirements, Headquarters, USAF, Washington 25, D.C. ATTN: AFDRQ-SA/M
- 134 Director of Research and Development, DCS/D, Headquarters, USAF, Washington 25, D.C. ATTN: Combat Components Div.
- 135-136 Director of Intelligence, Headquarters, USAF, Washington 25, D.C. ATTN: AFOIN-IB2
- 137 The Surgeon General, Headquarters, USAF, Washington 25, D.C. ATTN: Bio. Def. Br., Pre. Med. Div.
- 138 Asst. Chief of Staff, Intelligence, Headquarters, U.S. Air Forces-Europe, APO 633, New York, N.Y. ATTN: Directorate of Air Targets
- 139 Commander, 497th Reconnaissance Technical Squadron (Augmented), APO 633, New York, N.Y.
- 140 Commander, Far East Air Forces, APO 925, San Francisco, Calif. ATTN: Special Asst. for Damage Control
- 141-142 Commander, Alaskan Air Command, APO 942, Seattle, Wash. ATTN: AAOIN
- 143 Commander, Northeast Air Command, APO 862, New York, N.Y.
- 144 Commander-in-Chief, Strategic Air Command, Offutt Air Force Base, Omaha, Nebraska. ATTN: OAWS
- 145 Commander, Tactical Air Command, Langley AFB, Va. ATTN: Documents Security Branch
- 146 Commander, Air Defense Command, Ent AFB, Colo.
- 147-148 Research Directorate, Headquarters, Air Force Special Weapons Center, Kirtland Air Force Base, New Mexico, ATTN: Blast Effects Ros.
- 149 Commander, Air Materiel Command, Wright-Patterson AFB, Dayton, O. ATTN: MCSW
- 150 Commander, Air Research and Development Command, PO Box 1395, Baltimore, Md. ATTN: RBDN
- 151 Commander, Air Proving Ground Command, Eglin AFB, Fla. ATTN: Adj./Tech. Report Branch
- 152-153 Director, Air University Library, Maxwell AFB, Ala.
- 154-161 Commander, Flying Training Air Force, Waco, Tex. ATTN: Director of Observer Training
- 162 Commander, Crew Training Air Force, Randolph Field, Tex. ATTN: 2GTS, DCS/O
- 163-164 Commandant, Air Force School of Aviation Medicine, Randolph AFB, Tex.
- 165 Commander, Wright Air Development Center, Wright-Patterson AFB, Dayton, O. ATTN: WCOSI
- 166-167 Commander, Air Force Cambridge Research Center, LG Hanscom Field, Bedford, Mass. ATTN: CRQST-2
- 168-170 Commander, Air Force Special Weapons Center, Kirtland AFB, N. Mex. ATTN: Library
- 171 Commander, Lowry AFB, Denver, Colo. ATTN: Department of Special Weapons Training
- 172 Commander, 1009th Special Weapons Squadron, Headquarters, USAF, Washington 25, D.C.
- 173-174 The RAND Corporation, 1700 Main Street, Santa Monica, Calif. ATTN: Nuclear Energy Division
- 175 Commander, Second Air Force, Barksdale AFB, Louisiana. ATTN: Operations Analysis Office
- 176 Commander, Eighth Air Force, Westover AFB, Mass. ATTN: Operations Analysis Office
- 177 Commander, Fifteenth Air Force, March AFB, Calif. ATTN: Operations Analysis Office
- 178 Commander, Western Development Div. (ARDC), PO Box 262, Inglewood, Calif. ATTN: WDSIT, Mr. R. G. Weitz
- 179-183 Technical Information Service Extension, Oak Ridge, Tenn. (Surplus)
- OTHER DEPARTMENT OF DEFENSE ACTIVITIES
- 184 Executive Secretary, Joint Chiefs of Staff, Washington 25, D.C.
- 185-186 Asst. Secretary of Defense, Research and Engineering D/D, Washington 25, D.C. ATTN: Tech. Library
- 187 U.S. Documents Officer, Office of the U.S. National Military Representative, SHAPE, APO 55, New York, N.Y.
- 188 Director, Weapons Systems Evaluation Group, OSD, Rm 2E1006, Pentagon, Washington 25, D.C.
- 189 Asst. for Civil Defense, OSD, Washington 25, D.C.
- 190 Armed Services Explosives Safety Board, D/D, Building T-7, Gravelly Point, Washington 25, D.C.
- 191 Executive Secretary, Military Liaison Committee, PO Box 1814, Washington 25, D.C.
- 192 Commandant, National War College, Washington 25, D.C. ATTN: Classified Records Library
- 193 Commandant, Armed Forces Staff College, Norfolk 11, Va. ATTN: Secretary
- 194 Commandant, Industrial College of the Armed Forces, Ft. Lesley J. McNair, Washington 25, D.C.
- 195 Commander, Field Command, Armed Forces Special Weapons Project, PO Box 5100, Albuquerque, N. Mex.
- 196 Commander, Field Command, Armed Forces Special Weapons Project, PO Box 5100, Albuquerque, N. Mex. ATTN: Technical Training Group
- 197-201 Commander, Field Command, Armed Forces Special Weapons Project, P.O. Box 5100, Albuquerque, N. Mex. ATTN: Deputy Chief of Staff, Weapons Effects Test

~~CONFIDENTIAL~~

202-212	Chief, Armed Forces Special Weapons Project, Washington 25, D.C. ATTN: Documents Library Branch	222-223	Los Alamos Scientific Laboratory, Report Library, PO Box 1663, Los Alamos, N. Mex. ATTN: Helen Reizen
213	Commanding General, Military District of Washington, Room 1543, Building T-7, Gravelly Point, Va.	224-228	Sandia Corporation, Classified Document Division, Sandia Base, Albuquerque, N. Mex. ATTN: W. J. Smyth, Jr.
214-218	Technical Information Service Extension, Oak Ridge, Tenn. (Surplus)	229-231	University of California Radiation Laboratory, PO Box 806, Livermore, Calif. ATTN: Gloria G. Smith
ATOMIC ENERGY COMMISSION ACTIVITIES		232	Weapon Data Section, Technical Information Service Extension, Oak Ridge, Tenn.
219-221	U.S. Atomic Energy Commission, Classified Technical Library, 1901 Constitution Ave., Washington 25, D.C. ATTN: Mrs. J. M. O'Leary (For DMA)	233-245	Technical Information Service Extension, Oak Ridge, Tenn. (Surplus)